



저작자표시-비영리-변경금지 2.0 대한민국

이용자는 아래의 조건을 따르는 경우에 한하여 자유롭게

- 이 저작물을 복제, 배포, 전송, 전시, 공연 및 방송할 수 있습니다.

다음과 같은 조건을 따라야 합니다:



저작자표시. 귀하는 원 저작자를 표시하여야 합니다.



비영리. 귀하는 이 저작물을 영리 목적으로 이용할 수 없습니다.



변경금지. 귀하는 이 저작물을 개작, 변형 또는 가공할 수 없습니다.

- 귀하는, 이 저작물의 재이용이나 배포의 경우, 이 저작물에 적용된 이용허락조건을 명확하게 나타내어야 합니다.
- 저작권자로부터 별도의 허가를 받으면 이러한 조건들은 적용되지 않습니다.

저작권법에 따른 이용자의 권리와 책임은 위의 내용에 의하여 영향을 받지 않습니다.

이것은 [이용허락규약\(Legal Code\)](#)을 이해하기 쉽게 요약한 것입니다.

[Disclaimer](#)



공학박사학위논문

Growth Mechanism of Compound
Semiconductor Nanostructures on 2-D
Materials Studied by Improved Direct
Growth and Observation Techniques

개선된 투과전자현미경 분석법을 이용한 이차원 물질
위에서의 화합물 반도체 나노구조물의 결정성장
메커니즘 연구

by

Janghyun Jo

August, 2017

Department of Materials Science and Engineering
COLLEGE OF ENGINEERING
SEOUL NATIONAL UNIVERSITY

Growth Mechanism of Compound Semiconductor Nanostructures on 2-D Materials Studied by Improved Direct Growth and Observation Techniques

개선된 투과전자현미경 분석법을 이용한 이차원
물질 위에서의 화합물 반도체 나노구조물의
결정성장 메커니즘 연구

지도 교수 김 미 영

이 논문을 공학박사 학위논문으로 제출함
2017년 8월

서울대학교 대학원
재료공학부
조 장 현

조장현의 박사 학위논문을 인준함
2017년 8월

위 원 장	박 찬	(인)
부위원장	김 미 영	(인)
위 원	장 호 원	(인)
위 원	박 경 수	(인)
위 원	이 종 훈	(인)

Abstract

Growth Mechanism of Compound Semiconductor Nanostructures on 2-D Materials Studied by Improved Direct Growth and Observation Techniques

Janghyun Jo

Department of Materials Science and Engineering

The Graduate School

Seoul National University

Atomically thin layered crystals isolated by mechanical exfoliation method have exhibited new physical properties and provided novel applications. Moreover, hybrid structures of these 2-dimensional (2-D) layered materials with semiconductor thin films and nanostructures offer additional functionalities, such as flexibility and transferability, thereby greatly extending the applicability to the electronic and optoelectronic devices. Accordingly, many efforts have focused on the growth of nanomaterials using 2-D materials as substrates. In order to fabricate such nanomaterials with desired shapes and physical properties, the study on the initial growth mechanisms, such as nucleation, nuclei growth, and orientational relationship with substrate, should

be accompanied in detail.

This work mainly focuses on exploring the growth mechanisms of compound semiconductor nanomaterials on graphene, as a representative material among various 2-D layered materials, using transmission electron microscopy (TEM). In order to avoid unintentional damages arising from conventional TEM sample preparation processes, “direct growth and observation” method was developed to observe nanomaterials at the early growth stages. In this method, electron-beam transparent graphene was exploited as a supporting layer for TEM measurements as well as a substrate for nanomaterials growth. Compound semiconductor nanomaterials including ZnO, InAs, and GaAs were grown on graphene which had been transferred onto a TEM grid, followed by TEM measurements conducted without TEM sample preparation processes. “Reflection high-energy electron diffraction (RHEED) transmission mode” was also employed to analyze the structural information of nanostructures in real time during the growth. Contrary to its conventional usage in reflection mode, RHEED was used in transmission mode. This new technique allows us to obtain diffraction patterns containing the structural information of nanomaterials, which is analogous to the principle of electron diffraction in TEM.

Using these newly developed methods, the growth mechanisms of compound semiconductor nanomaterials were thoroughly investigated. First, the growth behavior of ZnO nanomaterials was clearly observed with atomic-resolution and high-sensitivity using a graphene template for the “direct growth

and observation” method. This method successfully disclosed the growth behavior of ZnO nanomaterials on graphene, such as nucleation of ZnO cubic phase and formation of $\Sigma 7$ coincidence site lattice boundary, which are previously unknown. Second, the growth mechanisms of GaAs/single-layer graphene (SLG)/InAs double heterostructures were unraveled with an aid of a further improved “direct growth and observation” method. This study showed that InAs nanorods grown on SLG can influence on the nucleation and growth behavior of GaAs nanomaterials on the other side of SLG. Lastly, the growth behavior of InAs nanorods were investigated in real time using the RHEED transmission mode. Time-resolved observation using RHEED transmission mode revealed the transition in local growth condition from In-rich to As-rich at the very early stage of InAs nanorods growth and the strain relaxation process of GaAs/InAs coaxial nanorods during the shell layer coating.

Keywords: transmission electron microscopy, nucleation and growth, graphene, compound semiconductor, nanomaterials, direct growth and observation technique

Student Number: 2014-30226

Table of contents

Abstract.....	i
Table of contents.....	iv
List of Tables	vii
List of Figures.....	viii
CHAPTER 1.....	1
CHAPTER 2.....	9
2.1 Theory.....	10
2.1.1 Crystal growth: nucleation and growth	10
2.1.2 Heteroepitaxy	20
2.1.3. Van der Waals epitaxy	22
2.1.4. III-V nanorod growth mechanism: VLS growth	24
2.1.5. III-V nanorod growth mechanism: VS growth.....	26
2.2 Transmission electron microscopy	27
2.2.1 High-resolution TEM	27
CHAPTER 3.....	34
3.1 Fabrication of graphene templates	35
3.1.1 Growth of CVD graphene	35
3.1.2 Fabrication of SiNx membrane TEM grid	36
3.1.3 Graphene transfer.....	42
3.2 Materials growth.....	43
3.2.1 ZnO nanomaterials on a graphene template.....	43
3.2.2 GaAs/SLG/InAs double heterostructures.....	45
3.2.3 InAs coaxial nanorods on Si(111) and graphene.....	48
3.3 Materials characterization.....	50
3.3.1 Scanning electron microscopy	50

3.3.2 Transmission electron microscopy.....	50
3.3.3 Reflection high-energy electron diffraction	51
CHAPTER 4.....	53
4.1 Introduction	54
4.2 Direct growth and observation of nanomaterials using a graphene template	56
4.3 Feasibility of the new method for crystal growth and TEM measurements	59
4.4 Growth mechanism of ZnO nanomaterials on graphene	62
4.4.1 Nucleation	62
4.4.2 Grain boundary formation.....	67
4.5 Summary and outlook.....	71
CHAPTER 5.....	73
5.1 Introduction	74
5.2 Direct growth and observation of nanomaterials using a graphene and prefabricated SiNx membrane TEM grid	79
5.2.1 Prefabricated SiNx membrane TEM grid.....	79
5.2.2 Direct growth and observation of GaAs and InAs nanomaterials..	84
5.3 Feasibility of the improved method for crystal growth and TEM measurements	86
5.4 Growth mechanism of GaAs/SLG/InAs double heterostructures.....	90
5.4.1 Control group: growth behavior of GaAs on SLG	90
5.4.2 Experimental group: growth behavior of GaAs on SLG/InAs.....	94
5.4.3 General growth mechanism of double heterostructures	103
5.5 Summary and outlook.....	106
CHAPTER 6.....	107

6.1 Introduction	108
6.2 RHEED transmission mode.....	110
6.3 Feasibility of RHEED transmission mode for the real-time structural analysis of nanomaterials.....	113
6.4 Growth mechanism of InAs nanorods and GaAs($In_xGa_{1-x}As$)/InAs coaxial nanorods.....	121
6.4.1 Initial growth behavior of InAs nanorods	121
6.4.2 Strain relaxation of shell layers during the epitaxial growth	128
6.4.3 InAs nanorods growth on graphene layers.....	134
6.5 Summary and outlook.....	136
CHAPTER 7.....	138
7.1 Summary.....	138
7.2 Outlook	141
REFERENCES	142
ABSTRACT (IN KOREAN).....	150

List of Tables

Table 1.1. Types of compound semiconductor nanostructures studied in each chapter and corresponding new techniques employed for the crystal growth and TEM measurements.	8
Table 3.2. Processing conditions for the fabrication of SiNx membrane TEM grid at each step.....	40
Table 3.3. Growth conditions for ZnO nanomaterials on graphene	44
Table 3.4. Growth conditions for GaAs/SLG/InAs double heterostructures..	47
Table 3.5. Growth conditions for InAs nanorods and $In_xGa_{1-x}As(GaAs)/InAs$ coaxial nanorods.....	49

List of Figures

Figure 1.1. Paradigm shift in the semiconductor industry from bulk to nanostructured transistor with low-dimensional materials.....	5
Figure 1.2. Multi-dimensional hybrid heterostructures. (a) ZnO nanotubes grown on graphene layers. (b) GaAs nanowires grown on graphite. (c) GaN-based coaxial LED nanostructures grown on graphene layers. (d) ZnO quantum dots covered by graphene. (e) ZnO nanowires horizontally grown on graphene layers.	6
Figure 1.3. Prefabricated thin membrane TEM grids for both crystal growth and TEM measurements. (a) Pt growth on SiO ₂ window. (b) Pt growth on Si ₃ N ₄ film. (c) Pt nanocrystals synthesized in a liquid cell encapsulated with SiNx windows.	7
Figure 1.4. Research plans of this work. For each materials system, newly developed or modified “direct growth and observation” technique is proposed and feasibility/reliability of this method is thoroughly confirmed. Using this method, growth mechanism of each materials system is investigated in detail	8
Figure 2.1. Schematic diagrams showing nucleation of new phase. (a) Homogeneous nucleation, (b) Heterogeneous nucleation. The new phase (red particles) is created from surrounding vapor phase (white background).	11
Figure 2.2. Schematic diagrams showing homogeneous nucleation. (a) Nucleation of spherical solid particle with a radius of r in a vapor phase. (b) Volume Gibbs free energy change (blue curve, represented with ΔG_v) and surface free energy of the particle (red curve, represented with γ_{sv}) as a function of particle’s radius. Their contributions to the total Gibbs free energy change (ΔG) are summed and depicted as green curve. The critical size of nucleus (r^*) and the nucleation barrier (ΔG^*) for spontaneous nucleation are marked in the graph.....	15

Figure 2.3. Schematic diagrams showing heterogeneous nucleation. (a) Solid phase nucleated at the interface with a foreign body. The interfacial energies of solid-vapor (γ_{sv}), solid-foreign body (γ_{sc}), and foreign body-vapor (γ_{cv}) are depicted by vectors in the figure. The wetting angle of solid is denoted as θ . (b) The total Gibbs free energy change for heterogeneous nucleation having lower nucleation barrier is illustrated in comparison with that for homogeneous nucleation having higher nucleation barrier. The critical size of nucleus (r^*) and the nucleation barrier (ΔG^*) for spontaneous nucleation are marked in the graph.

..... 19

Figure 2.4. Schematic illustrations showing growth behavior of thin film and nanostructure step by step. Each step depicts top view image representing crystal growth on a substrate. Red color and white background denote the growing material and substrate, respectively. 20

Figure 2.5. Schematic diagrams showing heteroepitaxial growth. (a) Growing material and substrate with a lattice mismatch of $(a_s - a_g)/a_g$. a_s and a_g correspond to the lattice parameters of substrate and growing material, respectively. (b) Coherently strained growth on a substrate. (c) Strain relaxation of a growing material by forming defects at the interface. 22

Figure 2.6. Schematic diagrams showing van der Waals epitaxy. (a) Two-dimensional layered growing material and substrate with a lattice mismatch of $(a_s - a_g)/a_g$. a_s and a_g correspond to the lattice parameters of substrate and growing material, respectively. (b) Incommensurate growth on a substrate. (c) Growing material without strain and defect formation at the interface. (d) Van der Waals epitaxy in the system of 3-D growing material and 2-D substrate.

..... 24

Figure 2.7. Schematic illustrations showing VLS growth mechanism of nanorod. 25

Figure 2.8. Schematic illustrations showing catalyst-free growth mechanism of nanorod. 26

Figure 2.9. Schematic illustration showing the formation of direct and diffracted beams by the interaction with a crystal and their contribution to the image formation.....	28
Figure 2.10. Lattice fringes created under two-beam condition. (a) Direct and diffracted beam, as represented 0 and G , selected by an objective aperture for the two-beam condition. (b) Lattice fringes of HR-TEM image formed under two-beam condition in (a).....	32
Figure 2.11. Lattice fringes created under multi-beam condition. (a) Direct and diffracted beams, as represented 0, G_1 , G_2 , and G_3 , selected by an objective aperture for the two-beam condition. (b) Lattice fringes of HR-TEM image formed under multi-beam condition in (a).....	33
Figure 3.1. Schematic illustration of homemade CVD furnace chamber.....	35
Figure 3.2. Overall fabrication processes of SiNx membrane TEM grid.....	39
Figure 3.3. Schematic illustration of homemade vertical-type 2-inch MOCVD chamber.....	44
Figure 3.4. Schematic illustration of MBE system (RIBER 32P).....	46
Figure 4.1. Schematic diagram of the “direct growth and observation” technique for growing ZnO nanomaterials on graphene and performing TEM measurements. Graphene was grown by CVD method and transferred onto a Cu mesh TEM grid with a perforated amorphous carbon supporting layer. The graphene surface was exposed to O ₂ plasma to enhance nucleation of nanomaterials. ZnO nanomaterials were then grown on the plasma-treated graphene layers by MOCVD method and observed using TEM. No additional TEM sample preparation processes, such as manual grinding or ion milling, was carried.	58
Figure 4.2. Feasibility of a graphene/TEM grid template for nanomaterials	

growth and TEM measurements. (a) Photograph of the template after the growth of ZnO nanomaterials. This shows that the TEM grid maintained its structure after the growth at 580 °C for 15 min. (b) OM image of the template. The inset is a magnified OM image of a TEM mesh, showing micrometer-sized holes with an amorphous carbon layer underneath the graphene..... 61

Figure 4.3. Atomic-resolution images of ZnO nanomaterials grown on a graphene layers..... 61

Figure 4.4. Crystal structure transition of ZnO nucleus from cubic to hexagonal in the early growth stage. (a,b) HR-TEM images of ZnO nucleus obtained for growth times of (a) 10 s and (b) 1 min. (c) HR-TEM image of ZnO grown for 10 s, the same as (a), and left in a reactor for another 6 min afterward with only O₂ gas introduced. The corresponding FFTs and zone axes are provided in each figure. In the insets, the diffraction peaks of ZnO and graphene are marked with green and yellow circles, respectively. (d) Epitaxial relationships between rocksalt/wurtzite ZnO and graphene illustrated using a ball-and-stick model. The C, O, and Zn atoms are represented by blue, green, and yellow balls, respectively. Both rocksalt and wurtzite structures are placed on a basal plane of graphene, and their projected unit cells, along with their zone axes, are identified in the figure with red and blue dashed lines..... 66

Figure 4.5. Grain boundary formation during ZnO nanomaterials growth. (a) BF image obtained in the region where ZnO grains had substantially coalesced. The dashed lines denote low-angle grain boundaries. HR-TEM images were taken at each marked region, clearly showing the atomic configurations of grain boundaries. (b) Low-angle grain boundary containing an array of edge-type dislocation cores. The boundary has a rotation angle of 7.1°. (c) High-angle grain boundary with a rotation angle of 22.6° and the {12̄30} boundary plane. Dislocation-like structural units periodically shown along the boundary are denoted by arrows. 69

Figure 4.6. Distortion of atomic arrangements nearby various defects. (a)

Enlarged HR-TEM image of Figure 4.5b, focusing on the dislocation core at the low-angle grain boundary. The Burgers circuit is drawn around the dislocation core at the grain boundary, which reveals a Burgers vector of $b = 1/3\langle 11\bar{2}0 \rangle$. (b) Enlarged HR-TEM image of Figure 4.5c, focusing on the grain boundary. The quadrilaterals representing structural units are marked along the high-angle grain boundary plane of $\{12\bar{3}0\}$. The Burgers circuit is also drawn around the dislocation core, which reveals a Burgers vector of $b = 1/3\langle 11\bar{2}0 \rangle$. The directions a_1 , a_2 , and a_3 in the figures are hexagonal lattice vectors, and the yellow arrows denote the Burgers vectors of the defects..... 70

Figure 5.1. InAs/SLG/InAs double heterostructures. (a) Schematic illustration of InAs/SLG/InAs double heterostructures with polarity directions of InAs denoted in the figure. (b) Calculated van der Waals binding energy depending on the van der Waals gap between InAs and SLG for InAs/SLG and InAs/SLG/InAs double heterostructures, respectively..... 77

Figure 5.2. GaAs thin films grown on graphene-coated GaAs(001) substrate. (a,b) Density functional theory calculations of averaged electron density along directions identified by arrows between separated slabs of GaAs for (a) As–Ga interaction and (b) As–As interaction, respectively. (c–e) Electron backscattered diffraction orientational maps of GaAs thin films grown on (c) SLG, (d) bilayer graphene, and (e) tetralayer graphene-coated GaAs(001) substrate..... 78

Figure 5.3. Schematic illustrations of a prefabricated SiNx membrane TEM grid. (a) Top view image of 5×5 array of SiNx membrane chips fabricated on a Si(100) wafer. (b) Cross-sectional image of SiNx membrane chips. Perforated SiNx membrane is clearly visible on the Si(100) wafer which will be used for atomic-resolution imaging in TEM. Red boxes in (a) and (b) indicate a region of single SiNx membrane TEM grid..... 82

Figure 5.4. Homemade SiNx membrane TEM grid. (a) OM image of 5×5 array

of prefabricated SiNx membrane chips. (b) Single SiNx membrane TEM grids. (c) SiNx membrane suspended over the square-shaped hole of a Si(100) wafer. (d) TEM image of an array of circular holes with a diameter of 0.5–2 μm in the SiNx membrane..... 83

Figure 5.5. Direct growth and observation method using a graphene and SiNx membrane TEM grid. Graphene was transferred onto a prefabricated SiNx membrane TEM grid. InAs was grown first on the backside of graphene by catalyst-free MBE method. Afterward, GaAs was deposited on the front side of graphene. After the growth, TEM measurements were performed without conventional TEM sample preparation processes. 85

Figure 5.6. Feasibility of a graphene/SiNx membrane TEM grid template for nanomaterials growth and TEM measurements. (a) Photograph of the templates loaded in a sample loading holder of MBE chamber. The templates are identified by red circles. (b) TEM image of an array of circular holes in the nitride membrane after the growth of GaAs and InAs on/underneath SLG. This shows that the graphene/SiNx membrane maintained its structure after the growth at high temperatures. (c) SEM image of GaAs and InAs nanomaterials grown on/underneath SLG suspended over the perforated nitride membrane.

..... 88

Figure 5.7. Atomic-resolution imaging performed over the suspended SLG. (a) HR-TEM image of GaAs and InAs nanomaterials grown on/underneath SLG. (b) HR-TEM image of SLG. 89

Figure 5.8. Various growth directions of GaAs clusters grown on SLG. (a–c) HR-TEM images showing GaAs clusters grown on SLG with a [111]_{ZB} direction (a) pointing laterally, (b) pointing vertically, and (c) tilted with respect to the surface of SLG, respectively. Schematics in the insets represent the directions of GaAs [111]_{ZB}. Each grain in the cluster is identified by dashed lines. The [111]_{ZB} direction of each grain is identified by an arrow. (d–f) Corresponding FFT patterns obtained from GaAs grains marked with asterisks

in (a–c), respectively. The FFT peaks from SLG and GaAs were identified with yellow and cyan circles, respectively. The growth directions of GaAs grains, termed as crystallographic zone axis (Z.A.), are indicated in the figures. 91

Figure 5.9. Statistics for the growth direction of GaAs clusters on SLG. (a) The number of GaAs grains classified by their $[111]_{\text{ZB}}$ directions with respect to the surface of graphene. Horizontal, vertical, and tilted directions correspond to $[111]_{\text{ZB}}$ directions of GaAs grains formed as shown in Figure 5.8a–c, respectively. (b) The number of GaAs grains having a horizontal $[111]_{\text{ZB}}$ direction, which is further classified by their growth directions as shown in the legend. The green portion named ‘others’ in the legend indicates GaAs grains with a horizontal $[111]_{\text{ZB}}$ direction, but the growth direction was not fully identified. 93

Figure 5.10. Various growth directions of GaAs clusters grown on SLG/InAs nanorods. (a–c) HR-TEM images showing GaAs clusters grown on SLG/InAs nanorods with both GaAs $[111]_{\text{ZB}}$ and InAs $[0001]_{\text{WZ}}$ directions pointing (a–b) vertically and (c) laterally with respect to the surface of SLG, respectively. Schematics in the insets represent the directions of GaAs $[111]_{\text{ZB}}$ and InAs $[0001]_{\text{WZ}}$. The grains of GaAs and InAs in the clusters are identified by cyan and green dashed lines, respectively. The $[111]_{\text{ZB}}$ direction of each grain is identified by an arrow. The dashed regions in (a) depict overlap areas of GaAs on SLG and InAs underneath SLG. (d–e) Corresponding FFT patterns obtained from GaAs grains marked with asterisks in (a–b), respectively. The FFT peaks from SLG, GaAs and InAs were identified with yellow, cyan, and green circles, respectively. The growth directions of GaAs grains, termed as crystallographic zone axis (Z.A.), are indicated in the figures. 95

Figure 5.11. Statistics for the growth direction of GaAs clusters on SLG/InAs_{vertical} nanorods. (a) The number of GaAs grains classified by their $[111]_{\text{ZB}}$ directions with respect to the surface of graphene depending on the overlap area of GaAs and InAs (A_{overlap}). Horizontal, vertical, and tilted directions correspond to $[111]_{\text{ZB}}$ directions of GaAs grains formed as shown in

Figure 5.8a–c. (b) The number of GaAs grains classified by their growth directions as represented in the legend, depending on the overlap area. GaAs grains having a horizontal [111]_{ZB} direction were only considered. The green portion named ‘others’ in the legend indicates GaAs grains with a horizontal [111]_{ZB} direction, but the growth direction was not fully identified. The numbers in the parentheses at the top represent the total number of GaAs grains observed..... 98

Figure 5.12. Statistics for the growth direction of GaAs clusters on SLG/InAs_{horizontal}. (a) The number of GaAs grains classified by their [111]_{ZB} directions with respect to the surface of graphene depending on the overlap area of GaAs and InAs with horizontal [0001]_{wz} direction. Horizontal, vertical, and tilted directions correspond to [111]_{ZB} directions of GaAs grains formed as shown in Figure 5.8a–c. (b) The number of GaAs grains classified by their growth directions as represented in the legend, depending on the overlap area. GaAs grains having a horizontal [111]_{ZB} direction were only considered. The green portion named ‘others’ in the legend indicates GaAs grains with a horizontal [111]_{ZB} direction, but the growth direction was not fully identified. The numbers in the parentheses at the top represent the total number of GaAs grains observed..... 101

Figure 5.13. Statistics for the growth direction of GaAs clusters on SLG/InAs_{tilted}. (a) The number of GaAs grains classified by their [111]_{ZB} directions with respect to the surface of graphene depending on the overlap area of GaAs and InAs with tilted [0001]_{wz} direction. Horizontal, vertical, and tilted directions correspond to [111]_{ZB} directions of GaAs grains formed as shown in Figure 5.8a–c. (b) The number of GaAs grains classified by their growth directions as represented in the legend, depending on the overlap area. GaAs grains having a horizontal [111]_{ZB} direction were only considered. The green portion named ‘others’ in the legend indicates GaAs grains with a horizontal [111]_{ZB} direction, but the growth direction was not fully identified. The numbers in the parentheses at the top represent the total number of GaAs grains

observed..... 102

Figure 5.14. Growth direction flip of GaAs clusters. (a) GaAs clusters grown on SLG. (b) GaAs clusters grown on SLG/InAs with vertical [0001]_{WZ} direction. (c) GaAs clusters grown on SLG/InAs with horizontal [0001]_{WZ} direction. 104

Figure 5.15. Schematic diagrams showing growth mechanism of GaAs/SLG/InAs double heterostructures. GaAs and InAs nanostructures are represented by blue and green polygons, respectively, with their atomic configurations observed along [11 $\bar{2}$ 0]_{WZ}/[1 $\bar{1}$ 0]_{ZB} directions. The directions of GaAs [111]_{ZB} and InAs [0001]_{WZ} are identified by blue and green arrows, respectively..... 105

Figure 6.1. Schematic illustration of electron diffraction in TEM and RHEED. The electron diffraction in RHEED is compared with that in TEM. The RHEED electron beam has a larger spot size of 200 μm compared with a beam size in TEM. It glances off the surface of the substrate with an angle of *ca.* 0.8°. The size of the area irradiated by the electron beam is *ca.* 200 $\mu\text{m} \times 1.5$ cm. The large spot size indicates that the RHEED diffraction pattern provides information concerning the nanostructures over a wide area of the specimen.

..... 112

Figure 6.2. SEM images showing the surface morphology of nanorods grown on Si(111) substrate. (a) InAs nanorods. (b) InAs nanorods grown only for 30 s. (c) In_xGa_{1-x}As/InAs coaxial nanorods. (d) GaAs/InAs coaxial nanorods.. 114

Figure 6.3. Correlation between RHEED and TEM diffraction patterns. (a–c) Overlap of (top) RHEED patterns and (bottom) corresponding FFT patterns obtained from the HR-TEM images in (d)–(f) taken along the directions of (a) [10 $\bar{1}$ 0] _{WZ}/[2 $\bar{1}$ 1]_{ZB}, (b) [41 $\bar{5}$ 0] _{WZ}/[3 $\bar{2}$ 1]_{ZB}, and (c) [11 $\bar{2}$ 0] _{WZ}/[1 $\bar{1}$ 0]_{ZB}, respectively. (d–f) HR-TEM images of InAs nanorods taken along the same three orientations. Inset of (e) displays the relationship between these orientations. (g–i) Simulated electron diffraction patterns along the same three

directions of (a)–(c), respectively. Red and blue dots represent diffraction spots for WZ and ZB, respectively. (h) and (i) also consist of symmetric twinned ZB structures, as illustrated in detail in Figure 6.4.....117

Figure 6.4. Simulated electron diffraction patterns of InAs WZ and ZB phases obtained along the three different orientations. Diffraction patterns of InAs ZB phase were acquired from ZB phase with L chirality depicted in Figure 6.3h and i.....118

Figure 6.5. RHEED patterns of poorly-aligned InAs nanorods. (a) (top) RHEED patterns of InAs nanorods grown on Si(111), Si(100) and Si(110) substrates. (bottom) Corresponding SEM images of InAs nanorods. A schematic diagram of InAs nanorods representing their crystal growth direction is displayed in each RHEED pattern. (b) (top) RHEED patterns depending on the vertical alignment of InAs nanorods grown on Si(111) substrates. (bottom) Corresponding SEM images of InAs nanorods. All of the RHEED patterns were acquired along the $[11\bar{2}0]_{\text{WZ}}/[1\bar{1}0]_{\text{ZB}}$ direction of the nanorod.120

Figure 6.6. Real-time observation of the initial growth behavior of InAs nanorods on the Si(111) substrate. (a–c) RHEED patterns obtained (a) just before the start of growth, and (b) 30 s and (c) 15 min after growth commencement, respectively. Streaks in (a) and diffraction spots in (b) are indexed in the figures. (d) Schematic illustration of the growth behavior of InAs nanorods on the Si(111) substrate. (e) HR-TEM image of InAs nanorod grown for 30 s, taken at the region indicated in the inset. The inset shows a low-magnification image of InAs nanorod. (f,g) FFT patterns obtained for (f) twinned ZB and (g) WZ regions in (e), respectively. Twin-ZB and WZ-sensitive spots are denoted by blue and yellow arrows in (f) and (g), respectively. All of the RHEED and TEM diffraction patterns were taken along the $[11\bar{2}0]_{\text{WZ}}/[1\bar{1}0]_{\text{ZB}}$ direction to distinguish the ZB and WZ spots.126

Figure 6.7. Growth mechanisms of InAs nanorods. The four image sets at the top show the crystal structures of the InAs nanorods at the interface with the

Si(111) substrate at an early stage of growth. The four lower image sets show the crystal structures of fully-grown InAs nanorods and nanoislands at the base. Each image set consists of a low-magnification BF image of InAs nanorods, HR-TEM image obtained from the region indicated by the dashed square in the BF image and FFT micrograph obtained from the HR-TEM image. The last image at the bottom is SEM image showing InAs nanoislands. ZB and WZ layers free of stacking faults are indicated in the figures by dashed arrows along the $[0001]_{\text{wz}}/[111]_{\text{ZB}}$ growth direction. The data shown here are representative of more than 10 nanorods..... 127

Figure 6.8. $\text{In}_x\text{Ga}_{1-x}\text{As}/\text{InAs}$ and GaAs/InAs coaxial nanorods. HAADF-STEM images of (a) $\text{In}_x\text{Ga}_{1-x}\text{As}/\text{InAs}$ and (b) GaAs/InAs coaxial nanorods and corresponding EDS element maps of In, Ga, and As, respectively. EDS line profiles of In, Ga, and As were obtained across the coaxial nanorods, and displayed in each HAADF-STEM image. The interfaces and edges of the coaxial nanorods were marked by white-dashed lines by comparing HAADF-STEM images and EDS element maps and line profiles..... 128

Figure 6.9. Real-time structural analysis of the shell layers during the coaxial coating on InAs core nanorods. (a,b) HR-TEM images of (a) $\text{In}_x\text{Ga}_{1-x}\text{As}/\text{InAs}$ and (b) GaAs/InAs coaxial nanorods. (c,d) Series of RHEED patterns acquired during (c) $\text{In}_x\text{Ga}_{1-x}\text{As}$ and (d) GaAs shell layers coating on InAs nanorods. All of the RHEED patterns are aligned with respect to their transmitted beams as zero points, which are not shown in the images. The growth time for each RHEED pattern is indicated in the image. All of the RHEED patterns were obtained along a direction of $[11\bar{2}0]_{\text{wz}}/[1\bar{1}0]_{\text{ZB}}$. (e) RHEED intensity profiles around $\text{InAs}(0004)_{\text{wz}}/(222)_{\text{ZB}}$ and $\text{GaAs}(0004)_{\text{wz}}/(222)_{\text{ZB}}$ spots at growth times of 0, 1, 2, 4 and 15 min in (d). The RHEED intensities were measured along the central vertical line intersecting the $(000l)_{\text{wz}}$ diffraction spots. The positions of the GaAs peaks at which the GaAs spots appeared are indicated by arrows on the plots. The expected positions of the GaAs and InAs spots corresponding to their lattice constants of $(0002)_{\text{wz}}/(111)_{\text{ZB}}$ and $(0004)_{\text{wz}}/(222)_{\text{ZB}}$ are indicated

by dashed lines in (c)–(e) 132

Figure 6.10. Microstructural defects within the shell layers of coaxial nanorods. (a,c) HR-TEM images of $In_xGa_{1-x}As/InAs$ and GaAs/InAs coaxial nanorods obtained along the $[11\bar{2}0]_{WZ}/[1\bar{1}0]_{ZB}$ direction. (b,d) Corresponding Fourier-filtered images obtained by selecting FFT $(0002)_{WZ}/(111)_{ZB}$ spots of (a) and (c), respectively. The locations of dislocations are indicated by the ‘T’ symbol. The yellow and red colors of the symbol represent extra half-planes inserted toward the InAs core nanorod and toward the edge of the shell layer, respectively. The edge of the nanorods and the interfaces between the core and shell layers were identified by EDS line scans and are indicated by the white-dashed lines in (b) and (d). 133

Figure 6.11. RHEED patterns acquired during the growth of InAs nanorods on graphene layers. (a) Streaky and ring patterns from graphene layers obtained before the growth. (b) Spotty pattern of InAs nanorods obtained after the growth. (c) Intensity changes of RHEED spotty patterns as the growth proceeded. Black and red profiles are obtained in the square and circular boxes in (b), respectively, during the growth. The insets denoted as i and ii represent intensity changes in the positions identified with white-dashed lines of Slice 1 and 2 in (b), respectively. 135

CHAPTER 1

Introduction

Modern society and industry have been greatly developed together with critical breakthroughs in bulk single crystal growth technology, which contributed to the earliest beginning of the solid state physics and electronics in the mid-twenties century. The establishment of crystal growth theory based on thermodynamics and kinetics, such as nucleation, crystallization, and epitaxy, followed by the development of the advanced method to control doping concentration and site and interface properties, has fueled a dramatic paradigm shift in the semiconductor industry. Such a great change in semiconductor science and technology brought to life remarkable inventions such as transistors (Nobel Prize in 1956), tunneling devices (Nobel Prize in 1973), low-dimensional quantum devices (Nobel Prizes in 1985 and 1998), integrated circuits, and light-emitting diodes (LEDs; Nobel Prizes in 2000 and 2014), and thus has greatly advanced the life style of human being over the past few decades. Recently, due to the demand for next-generation devices in a fast-

changing world, we are facing a new paradigm shift that would exceedingly change our life once again (Figure 1). In an upcoming high-technology society, new kinds of novel devices promoting convenience of people's everyday life and eliminating constraints of space and time are essentially needed. These include wearable display, portable and ultra-high performance devices as well as small size, light weight and highly integrated devices. To realize such an achievement, future devices should be flexible, transparent, and even multi-functional. However, current crystal growth technology based on the thin film growth on rigid bulk crystalline substrate cannot meet these requirements. Even though flexible devices have already been fabricated using organic materials and amorphous films,¹⁻⁶ single-crystalline inorganic compound semiconductors could demonstrate higher device performance due to their high carrier mobility and radiative recombination rate, as well as excellent thermal and mechanical stability.^{7,8} Therefore, we need to replace the existing device fabrication techniques with the development of new crystal growth technologies and sciences suitable for the next-generation devices.

Multi-dimensional hybrid heterostructures, composed of inorganic nanostructures or two-dimensional (2-D) layered materials grown directly on another 2-D materials, can be the most promising material systems for the next-generation device applications in solid state physics and electronics. Such hybrid structures with low-dimensional nanomaterials, including nanorods, nanowalls, and nanodiscs, can be used as building blocks for the downsized and integrated devices (Figure 2).⁹⁻¹⁶ In addition, contrary to the bulk substrate, 2-

D layered materials, such as graphene, hexagonal boron nitride (*h*-BN), metal chalcogenides and their hybrids, are atomically thin, thus they can be flexible, stretchable, and transparent.¹⁷⁻¹⁹ They also exhibit excellent mechanical strength, thermal conductivity, and various kinds of electrical properties, which would provide significant opportunities for fabricating various electronic and optoelectronic devices by combining with low-dimensional nanostructures with well-controlled doping and quantum structures.^{20,21} Nevertheless, people have not yet exploited the full potential of hybrid heterostructures despite their persistent efforts. Such failure basically arises from a lack of fundamental knowledge about growth mechanisms of nanomaterials on 2-D materials. Because 2-D materials have physically inert surface without dangling bonds, conventional crystal growth theory based on bulk substrate cannot be directly applied. Therefore, studying the growth mechanisms of compound semiconductor nanostructures on 2-D materials, including how nuclei are formed and how they evolve into nanomaterials, has important implications in fabricating well-defined nanostructures with desired physical properties for device applications.

For a detailed understanding of the growth mechanisms which occurs on the order of a few nanometers, an atomic-level investigation should be performed. This type of high-resolution study has been mainly carried out using transmission electron microscopy (TEM). TEM offers crystallographic as well as atomic-resolution information on the crystal growth, which allows us to study the growth behavior of nanomaterials in diversified ways. However,

mechanical and chemical damage due to the conventional TEM sampling process, such as manual polishing and focused ion beam etching, which can be particularly severe for nano-sized objects, has restricted the analysis of growth behavior of nanomaterials at the atomic scale.²² In order to overcome this problem, several attempts were tried by directly growing nanomaterials on prefabricated thin membranes, such as *a*-carbon, Si₃N₄, and SiO₂, which also functioned as TEM grids for TEM measurements (Figure 3).²³⁻²⁶ However, the membranes with a thickness more than a few tens of nanometers caused poor electron transmittances and thus blurry images. This made it difficult to perform atomic-resolution imaging of nanomaterials, which is essential for the growth mechanisms study using TEM. Additionally, the membranes having amorphous characteristics cannot be used as substrates for crystal growth. Since these issues will not be solved only by conventional TEM analysis techniques, new approach enabling high-resolution study without damages on the sample should be suggested.

This work proposes two different methods to investigate the detailed growth mechanisms of compound semiconductor nanostructures without TEM sample preparation processes. The first technique is “direct growth and observation” method using graphene as an ideal template for a crystalline substrate for crystal growth as well as for an ultra-thin supporting layer for TEM measurements. This newly developed technique solves the problems of prefabricated membranes including blurry images and unsuitability for the crystal growth by using crystalline and atomically thin graphene instead of

amorphous and thick membranes. The second technique is “reflection high-energy electron diffraction (RHEED) transmission mode”. RHEED has been only employed in reflection mode to monitor the growth behavior of thin films during the growth. However, in this study, RHEED was used in transmission mode to acquire the structural information of nanomaterials in real time during the growth. Feasibility and reliability of these two methods for both crystal growth and TEM measurements were thoroughly confirmed. Afterward, these methods were applied to each materials system to investigate the growth mechanism; (1) ZnO nanomaterials grown on graphene layers, (2) GaAs/single-layer graphene (SLG)/InAs double heterostructures, and (3) InAs nanorods grown on Si(111) and graphene (Table 1 and Figure 4).

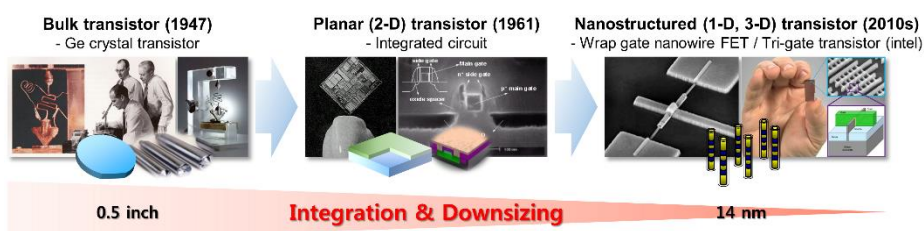


Figure 1.1. Paradigm shift in the semiconductor industry from bulk to nanostructured transistor with low-dimensional materials

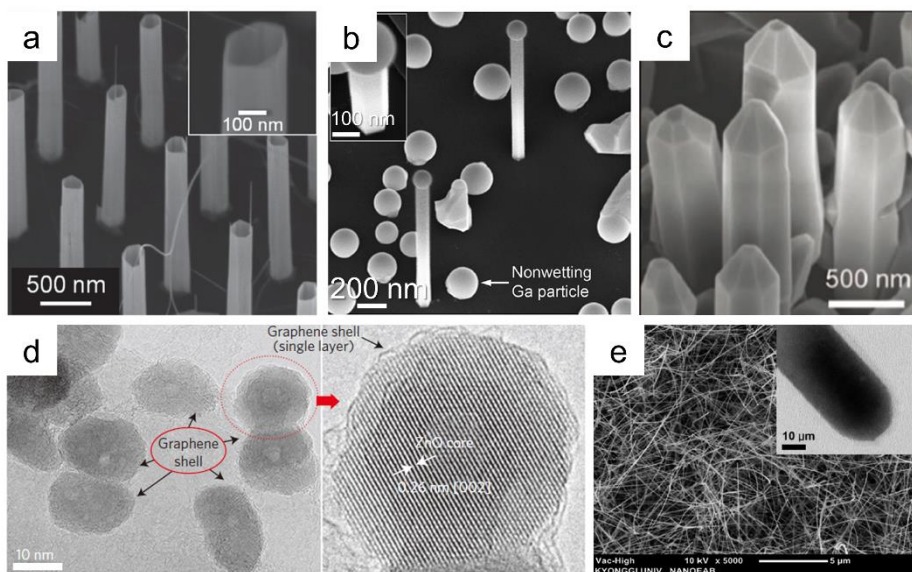


Figure 1.2. Multi-dimensional hybrid heterostructures. (a) ZnO nanotubes grown on graphene layers.¹⁴ (b) GaAs nanowires grown on graphite.¹⁵ (c) GaN-based coaxial LED nanostructures grown on graphene layers.¹² (d) ZnO quantum dots covered by graphene.¹⁶ (e) ZnO nanowires horizontally grown on graphene layers.¹³

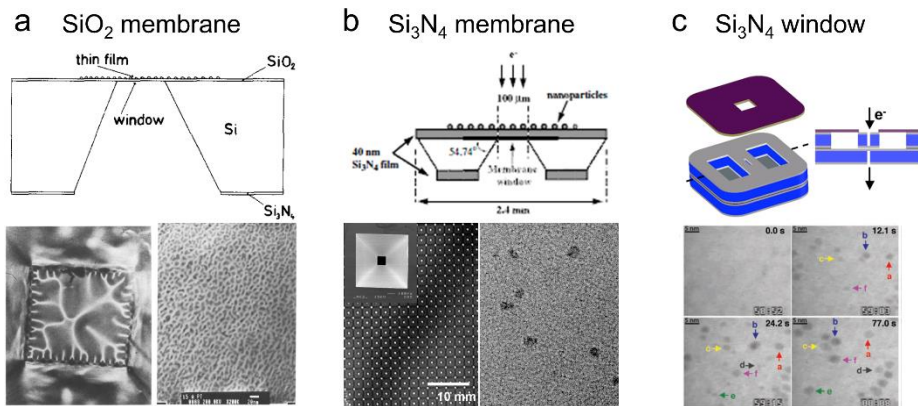


Figure 1.3. Prefabricated thin membrane TEM grids for both crystal growth and TEM measurements. (a) Pt growth on SiO_2 window.²³ (b) Pt growth on Si_3N_4 film.²⁵ (c) Pt nanocrystals synthesized in a liquid cell encapsulated with SiN_x windows.²⁶

Table 1.1. Types of compound semiconductor nanostructures studied in each chapter and corresponding new techniques employed for the crystal growth and TEM measurements.

	Chapter 4	Chapter 5	Chapter 6
Materials System	ZnO nanomaterials grown on graphene	GaAs/SLG/InAs double heterostructures	InAs nanorods grown on Si(111) and graphene
Technique	“Direct growth and observation” using a graphene template	Further improved “Direct growth and observation” using a graphene template	RHEED transmission mode
Schematics			



Figure 1.4. Research plans of this work. For each materials system, newly developed or modified “direct growth and observation” technique is proposed and feasibility/reliability of this method is thoroughly confirmed. Using this method, growth mechanism of each materials system is investigated in detail

CHAPTER 2

Scientific Background

This chapter provides fundamental knowledge underlying the scope of this study. The present work deals with crystal growth mechanisms of nanostructures studied by TEM. Thus, it is necessary to discuss general principles about crystal growth mechanisms and various TEM measurements before taking up the main subject. Firstly, general nucleation and growth theories are explained. Based on these general principles, specific growth behavior including van der Waals epitaxy and catalyst-free growth of nanorods is further described by comparing with conventional epitaxy and catalyst-induced growth of nanorods, respectively. Lastly, scientific background of various analysis methods in TEM is explained. TEM is intensely exploited over the whole part of this work to perform atomic-resolution imaging and reciprocal space analysis. Thus, the general principles of these analysis methods are briefly discussed.

2.1 Theory

2.1.1 Crystal growth: nucleation and growth

In general, crystal growth is a crystallization process in which atoms and molecules are gathered each other to form a closed-packed and periodically ordered structure, so called a crystal. In semiconductor industry, crystal growth means deposition of a single or many kinds of materials on a substrate to yield a crystalline solid by bottom-up approaches including physical vapor deposition and chemical vapor deposition (CVD) methods. Crystal growth is mainly divided into two different stages: nucleation and growth.

Nucleation is a very initial process of phase transformation from parent phase to thermodynamically new phase that has different crystal structure or physical/chemical properties. In crystal growth of compound semiconductor, a new crystalline solid phase is formed on a substrate from a vapor phase source in a growth chamber. Such a nucleation process indicates the formation of very small particles having a new solid phase. These particles normally consist of a few hundred atoms that are capable of growing further in size.

Nucleation, the formation of very small particles of new phase, can occur in two different ways: homogeneous and heterogeneous nucleation. In the case of homogeneous nucleation, small particles of the new phase form themselves uniformly anywhere within the parent phase (Figure 2.1a). On the other hand, in the case of heterogeneous nucleation, small particles of the new

phase form at the interface of foreign body, normally on a substrate (Figure 2.1b). This heterogeneous nucleation is the process we are dealing with for the crystal growth of compound semiconductor.

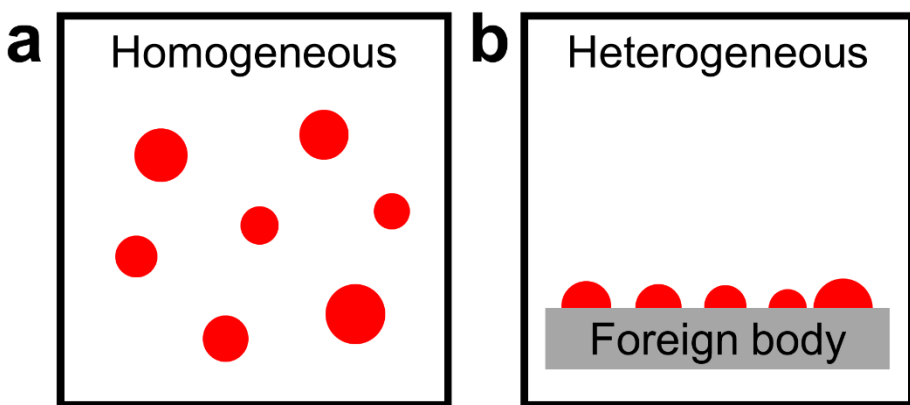


Figure 2.1. Schematic diagrams showing nucleation of new phase. (a) Homogeneous nucleation, (b) Heterogeneous nucleation. The new phase (red particles) is created from surrounding vapor phase (white background).

Let us first consider the homogeneous nucleation in detail. For the sake of convenient explanation, the solidification of a pure material in the vapor phase is assumed. In the nucleation process, a small particle of the new phase is further assumed to have spherical shape with a radius of r , as depicted in Figure 2.2a. The thermodynamic criterion for spontaneous nucleation is that the total Gibbs free energy change during nucleation ΔG should be negative as follows.²⁷

$$\Delta G = (\text{phase transformation from vapor to solid}) < 0 \quad (2.1)$$

There are two factors contributing to the total Gibbs free energy change for nucleation: volume Gibbs free energy change (ΔG_v) and surface free energy (γ_{sv}). The first term (ΔG_v) indicates the volume Gibbs free energy difference between solid and vapor phase caused by the formation of new solid phase and disappearance of parent phase in a unit volume. The contribution of volume Gibbs free energy change to the total Gibbs free energy change for nucleation is given by ΔG_v multiplied by the volume of nucleating particle.

$$(\text{Contribution of volume Gibbs free energy change}) = \frac{4}{3}\pi r^3 \Delta G_v \quad (2.2)$$

ΔG_v is always negative since Gibbs free energy for solid is lower than that for vapor when the conditions for spontaneous nucleation are satisfied. Therefore, the first term is always negative.

$$\Delta G_v = G_s - G_v < 0 \quad (2.3)$$

The second term (γ_{sv}) indicates the surface energy of solid-vapor phase boundary which is newly created during the nucleation. The contribution of surface free energy to the total Gibbs free energy change for nucleation is given by γ_{sv} multiplied by the surface area of nucleating particle.

$$(\text{Contribution of surface free energy}) = 4\pi r^2 \gamma_{sv} \quad (2.4)$$

γ_{sv} is always positive, thus the second term is also always positive.

$$\gamma_{sv} > 0 \quad (2.5)$$

The total Gibbs free energy change for nucleation is then expressed by the summation of aforementioned two terms.

$$\Delta G = \frac{4}{3}\pi r^3 \Delta G_v + 4\pi r^2 \gamma_{sv} \quad (2.6)$$

The nucleation process can be basically anticipated by the equation of the Gibbs free energy change for nucleation in Equation 2.6. This equation is plotted as a function of the radius of the nucleating particle r , as illustrated in Figure 2.2b. At the very beginning of nucleation process, ΔG increases with the size of the nucleating particle since the formation of new interface between solid and vapor phases, which has positive value, is a dominant factor in this regime. This indicates that the small particle of the new phase spontaneously shrinks and dissolves into single atoms or molecules. On the other hand, when the size of small particle exceeds r^* , ΔG decreases with the size of the nucleating particle since the formation of thermodynamically stable solid phase, which has negative value, is a dominant factor in this regime. This suggests that the nucleating particle spontaneously grows with the addition of surrounding

atoms and molecules. The small particle of the new phase which is smaller than r^* in radius is called *embryo*, whereas the particle which is larger than r^* in radius is called *nucleus*. In this context, r^* means a critical radius of the new particle for achieving spontaneous nucleation and growth. Additionally, the value of the total Gibbs free energy change for nucleation at nucleus's radius of r^* indicates nucleation barrier, or activation free energy ΔG^* , which is the energy required for the formation of a stable nucleus. These two terms are expressed as follows.

$$r^* = -\frac{2\gamma_{sv}}{\Delta G_v} \quad (2.7)$$

$$\Delta G^* = \frac{16\pi\gamma_{sv}^3}{3(\Delta G_v)^2} \quad (2.8)$$

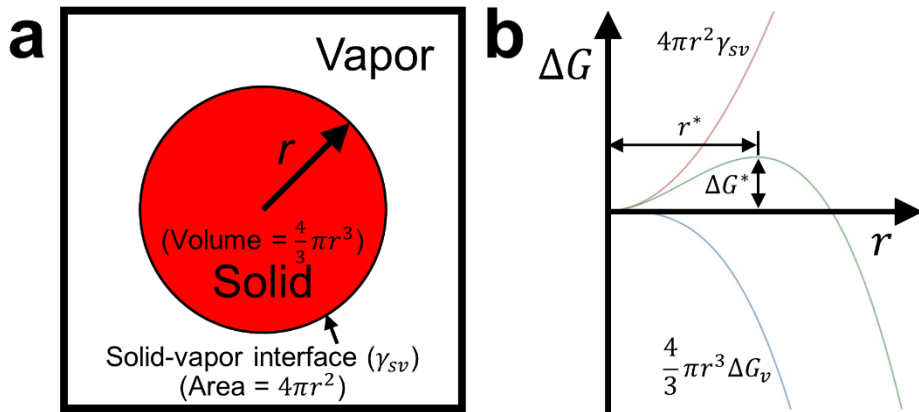


Figure 2.2. Schematic diagrams showing homogeneous nucleation. (a) Nucleation of spherical solid particle with a radius of r in a vapor phase. (b) Volume Gibbs free energy change (blue curve, represented with ΔG_v) and surface free energy of the particle (red curve, represented with γ_{sv}) as a function of particle's radius. Their contributions to the total Gibbs free energy change (ΔG) are summed and depicted as green curve. The critical size of nucleus (r^*) and the nucleation barrier (ΔG^*) for spontaneous nucleation are marked in the graph.

Next, the heterogeneous nucleation will be considered. For the sake of convenient explanation, the solidification of a pure material at the interface of a flat substrate in the surrounding vapor phase is assumed. In the nucleation process, solid and vapor phases wet the flat substrate and cover the whole surface of the substrate, thereby forming interfacial energies of solid-vapor (γ_{sv}), solid-foreign body (γ_{sc}), and foreign body-vapor (γ_{cv}), as shown in Figure 2.3a. The new solid phase at the interface is assumed to have spherical cap shape with a wetting angle θ on a substrate for the simple calculations.

Heterogeneous nucleation occurs much more easily and frequently than homogeneous nucleation does due to lowering of nucleation barrier ΔG^* caused by the reduced interfacial energy γ_{sv} with an aid of heterogeneous interface. Let us deal with these characteristics of heterogeneous nucleation in more detail by deriving equations for r_{het}^* and ΔG_{het}^* using same procedures as presented above for the case of homogeneous nucleation.

Three different surface energies (or tensions) depicted in Figure 2.3a keep a balance in the flat surface of a substrate as follows.

$$\gamma_{cv} = \gamma_{sc} + \gamma_{sv} \cos\theta \quad (2.9)$$

There are also two factors contributing to the total Gibbs free energy change for nucleation: volume Gibbs free energy change (ΔG_v) and interfacial free energy (γ_{sv}). The contribution of volume Gibbs free energy change to the total Gibbs free energy change for nucleation is given by ΔG_v multiplied by the volume of spherical cap in Figure 2.3a.

$$(\text{Contribution of volume Gibbs free energy change}) = \frac{4}{3}\pi r^3 \phi(\theta) \Delta G_v \quad (2.10)$$

$$\phi(\theta) = \frac{1}{4}(2 - 3 \cos\theta + \cos^3\theta) \quad (0 \leq \phi(\theta) \leq 1) \quad (2.11)$$

where $\phi(\theta)$ is a geometrical factor only depending on a wetting angle θ , which is governed by combinations of three different interfacial energies. The

contribution of surface free energy to the total Gibbs free energy change for nucleation is given by γ_{sv} , γ_{sc} , and γ_{cv} multiplied by their phase boundary areas.

$$\begin{aligned} \text{(Contribution of surface free energy)} = & \\ \pi r^2 \sin^2 \theta (\gamma_{sc} - \gamma_{sv}) + 4\pi r^2 \gamma_{cv} \left(\frac{1 - \cos \theta}{2} \right) & \end{aligned} \quad (2.12)$$

The total Gibbs free energy change for nucleation is then expressed by the summation of aforementioned two terms.

$$\Delta G_{het} = \frac{4}{3} \pi r^3 \phi(\theta) \Delta G_v + \pi r^2 \sin^2 \theta (\gamma_{sc} - \gamma_{sv}) + 4\pi r^2 \gamma_{cv} \left(\frac{1 - \cos \theta}{2} \right) \quad (2.13)$$

Using this equation, r_{het}^* and ΔG_{het}^* can be derived using the same scheme as performed for the case of homogeneous nucleation.

$$r_{het}^* = -\frac{2\gamma_{sv}}{\Delta G_v} \quad (2.14)$$

$$\Delta G_{het}^* = \left(\frac{16\pi\gamma_{sv}^3}{3(\Delta G_v)^2} \right) \phi(\theta) \quad (2.15)$$

These two terms are denoted in the plot of Equation 2.13 by comparing those for homogeneous nucleation (Figure 2.3b). The comparison between heterogeneous and homogeneous nucleation indicates that the critical radius size for heterogeneous nucleation r_{het}^* is identical to that for homogeneous nucleation r_{homo}^* provided that γ_{sv} remains same for both homogeneous and

heterogeneous nucleation. Additionally, the nucleation barrier for heterogeneous nucleation ΔG_{het}^* is lower than that for homogeneous nucleation ΔG_{homo}^* by the value of $\phi(\theta)$, thereby promoting the nucleation process.

The term $\phi(\theta)$ in the Equation 2.15 functions as a nucleation barrier lowering factor since the value of $\phi(\theta)$ is between 0 and 1. For the crystal growth of compound semiconductor, the interfacial energy between a substrate and a growing material γ_{sc} is strongly governed by their lattice match at the atomic scale. As the lattice match becomes more coherent, the interfacial energy γ_{sc} becomes lower, thus reducing the wetting angle θ and the term $\phi(\theta)$. This eventually results in reduced nucleation barrier ΔG_{het}^* compared with the crystal growth with poor lattice match.

Growth process is directly followed by the nucleation stage. The growth behavior of thin film and nanostructure is briefly illustrated in Figure 2.4. The nuclei formed during nucleation stage become larger in size and density. Afterward, the nuclei merge each other to create larger clusters under the growth condition of thin film. These clusters eventually cover the whole surface of a substrate to yield a flat thin film. In contrast, the nuclei hardly merge each other and grow themselves at their own sites under the growth condition of nanostructures, such as nanorod, nanowall, and nanodisc. These nanostructures prefer to grow vertically to yield nanostructures with high aspect ratio in case of nanorod and nanowire.

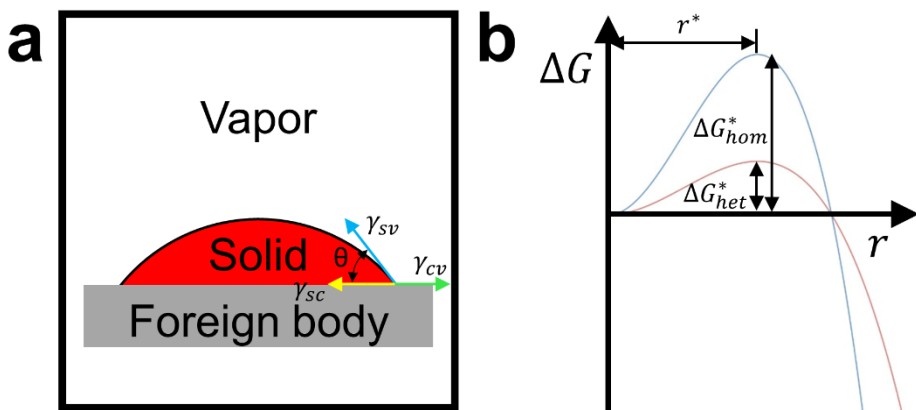


Figure 2.3. Schematic diagrams showing heterogeneous nucleation. (a) Solid phase nucleated at the interface with a foreign body. The interfacial energies of solid-vapor (γ_{sv}), solid-foreign body (γ_{sc}), and foreign body-vapor (γ_{cv}) are depicted by vectors in the figure. The wetting angle of solid is denoted as θ . (b) The total Gibbs free energy change for heterogeneous nucleation having lower nucleation barrier is illustrated in comparison with that for homogeneous nucleation having higher nucleation barrier. The critical size of nucleus (r^*) and the nucleation barrier (ΔG^*) for spontaneous nucleation are marked in the graph.

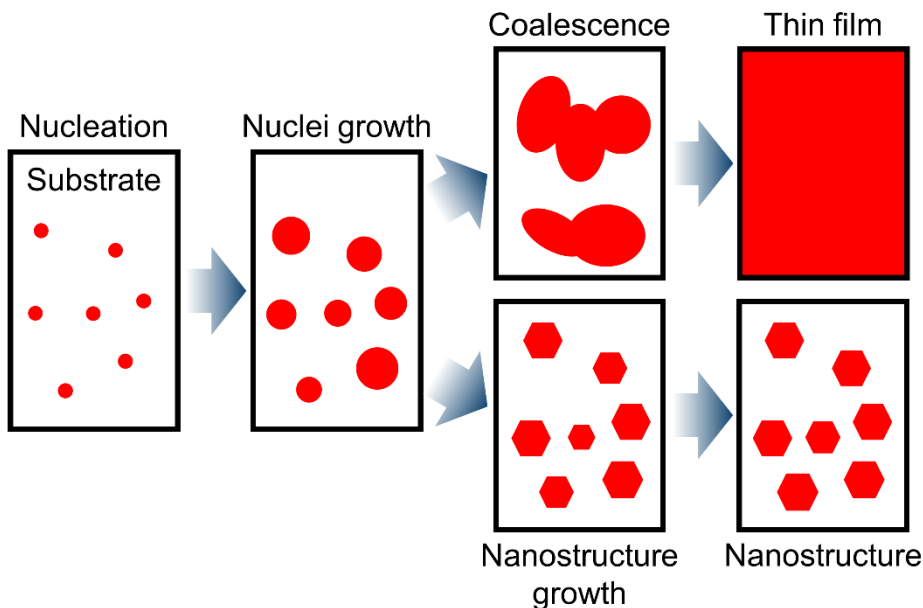


Figure 2.4. Schematic illustrations showing growth behavior of thin film and nanostructure step by step. Each step depicts top view image representing crystal growth on a substrate. Red color and white background denote the growing material and substrate, respectively.

2.1.2 Heteroepitaxy

Epitaxy is a two compound Greek word. The first word is “Epi” meaning above and the second one is “Taxis” meaning order.²⁸ In a crystal growth, epitaxy literally means that the crystal structure of the growing material is arranged in an ordered fashion with respect to atomic arrangements of the substrate at the interface. Heteroepitaxy is a special case of the epitaxy, when the growing material is different from the substrate (Figure 2.5a). Adatoms of the growing material form chemical bonds with distinct atoms of the substrate

with an aid of dangling bonds at the surface during the heteroepitaxial growth. The pairing between dislike atoms allows the growth in a strained structure to imitate atomic arrangements and crystalline symmetry of the substrate (Figure 2.5b). Such a strained structure of the growing material is maintained at the interface since chemical bonds formed between the growing material and the substrate are quite strong. The atomic arrangements of the growing material are elastically strained along both in-plane and out-of-plane directions, thereby deforming in-plane lattice parameters of the growing material to be identical to those of the substrate at the interface,

When the strain, otherwise called lattice mismatch between the growing material and the substrate, is small for the initial growth stage, the strain energy is stored well in the heteroepitaxial system as shown in Figure 2.5b. As the thickness of the growing material increases, the strain energy stored in the system also increases and thus cannot be accommodated anymore. When the thickness of the growing material exceeds a certain critical value, called critical thickness, various kinds of defects including threading dislocations, edge dislocations, and stacking faults are generated to relieve the strain energy (Figure 2.5c). Thus, both the in-plane and out-of-plane lattice parameters revert to their own values of the growing material.

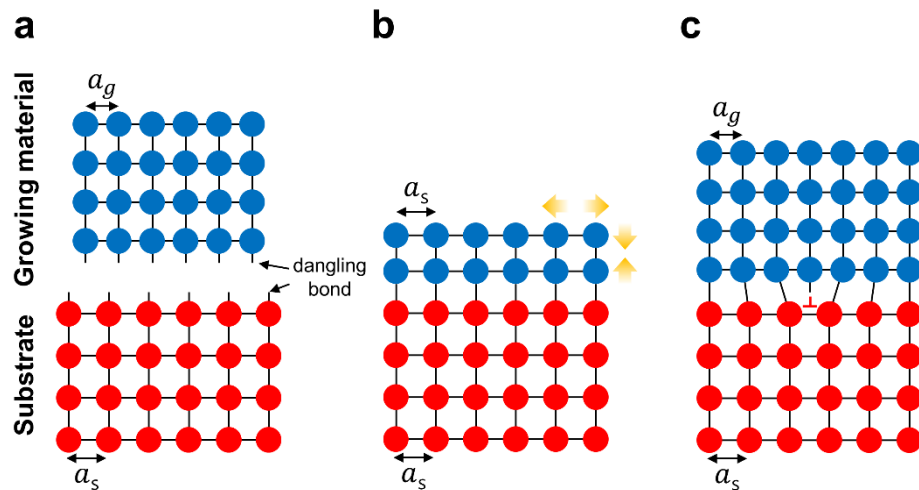


Figure 2.5. Schematic diagrams showing heteroepitaxial growth. (a) Growing material and substrate with a lattice mismatch of $(a_s - a_g)/a_g$. a_s and a_g correspond to the lattice parameters of substrate and growing material, respectively. (b) Coherently strained growth on a substrate. (c) Strain relaxation of a growing material by forming defects at the interface.

2.1.3. Van der Waals epitaxy

Van der Waals epitaxy is an epitaxial growth of 2-D layered material on the other 2-D layered substrate (Figure 2.6a).²⁸ In 1980s, Koma *et al.* suggested that the heterointerface of the growing material is bound to the 2-D layered material only by weak van der Waals interaction.²⁹ A weak van der Waals force at the heterointerface is the same interaction applied within each layer of 2-D material. This is contrast to the conventional epitaxial growth showing comparable strength of interactions between the growing material/substrate and the atoms in the growing material. Such a weak

interaction is much weaker than that from strong covalent bond in the epitaxial growth.

Van der Waals epitaxy features incommensurate growth at the heterointerface, indicating that the growing material is not strained by a weak interaction from the substrate; the in-plane and out-of-plane lattice parameters of the growing material remain unchanged (Figure 2.6b). A weak interaction relaxes the lattice matching conditions between the growing material and the substrate even in a large lattice mismatched system. Despite such a weak interaction, van der Waals epitaxy typically affects on the formation of epitaxial relationship between the growing material and the substrate for the energy minimization in the system. Thus, these characteristics of van der Waals epitaxy result in an epitaxial growth without defect formations at the abrupt heterointerface (Figure 2.6c). Additionally, these advantages of van der Waals epitaxy can be applied to the growth of 3-D material having dangling bonds on inert 2-D layered material, which is also called quasi-van der Waals epitaxy (Figure 2.6d).

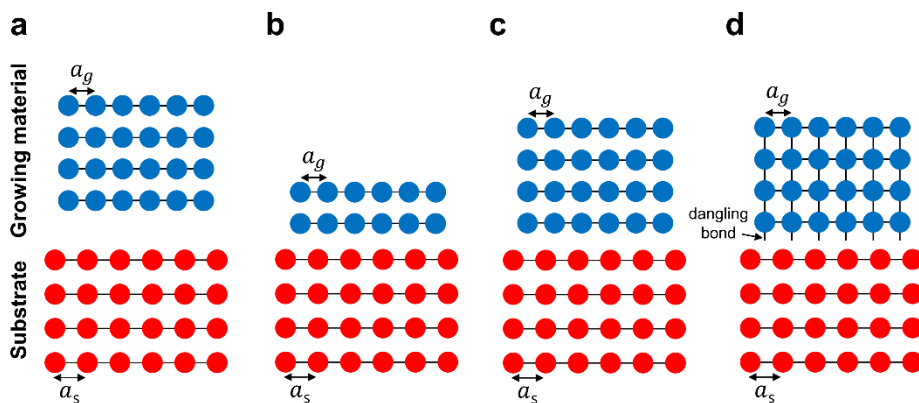


Figure 2.6. Schematic diagrams showing van der Waals epitaxy. (a) Two-dimensional layered growing material and substrate with a lattice mismatch of $(a_s - a_g)/a_g$. a_s and a_g correspond to the lattice parameters of substrate and growing material, respectively. (b) Incommensurate growth on a substrate. (c) Growing material without strain and defect formation at the interface. (d) Van der Waals epitaxy in the system of 3-D growing material and 2-D substrate.

2.1.4. III-V nanorod growth mechanism: VLS growth

In vapor-liquid-solid (VLS) growth of nanorods, a catalyst in liquid and amorphous state serves as a preferential absorption site for gas phase reactants. The catalyst stores up variable compositions during the growth and enhances nucleation process at the solid/liquid interface literally by reducing the nucleation barrier. Droplets of metal nanoparticle such as Au and self-catalyst, group III component in III-V nanorod, can be exploited as the catalyst for the growth.

The VLS growth mechanism of nanorods is schematically illustrated in Figure 2.7. The metal droplet forms to be served as a catalyst on a substrate

before the growth of nanorods. Its size is normally few tens of nanometers in diameter. After the growth begins, the catalyst is supersaturated with reactant gases, and nucleation process preferentially occurs at the interface between the liquid catalyst and the substrate. The nuclei particularly form at the perimeter of the solid/liquid interface since the surface energy term for the nucleation barrier of newly formed nuclei in Equation 2.15 is significantly reduced. The nuclei formed at such a triple phase boundary replace an existing liquid/vapor interface with a new nucleus/vapor interface whereas those in the inside of the catalyst should create new interfaces in all directions. Therefore, the total surface energy for the nuclei formed at the triple phase boundary is lowered compared with those inside the catalyst, resulting in the reduced nucleation barrier. The nanorod grows vertically by these nucleation and growth mechanisms. During the cool-down after the growth of nanorod, the catalyst solidifies and ends up with being located at the tip of the nanorod.

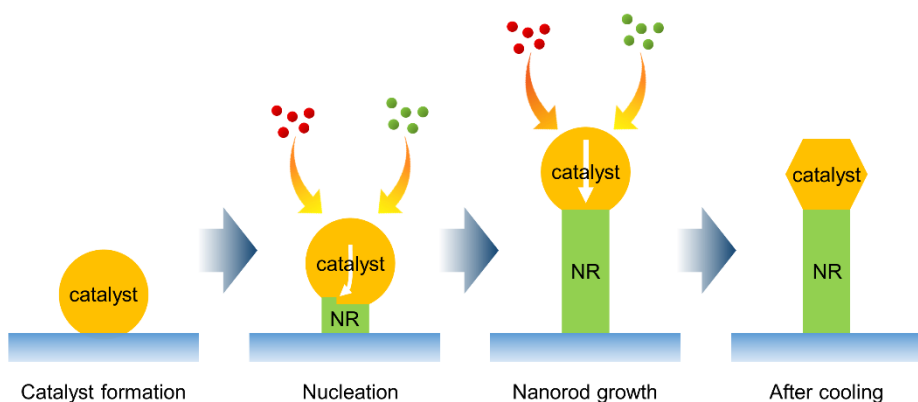


Figure 2.7. Schematic illustrations showing VLS growth mechanism of nanorod.

2.1.5. III-V nanorod growth mechanism: VS growth

In vapor-solid (VS) growth of nanorods, the nanorod grows vertically in the absence of a catalyst. This is also called catalyst-free growth by comparison with catalyst-induced VLS growth explained in Chapter 2.1.4. The catalyst-free growth mechanism of nanorods is schematically illustrated in Figure 2.8. Adatoms diffuse on the surface of a substrate and gathered together at specific sites. They react with gas phase reactants to form nucleus which overcome the nucleation barrier as represented in Equation 2.15. The nucleus then form side facets along the surface normal direction of the substrate. Afterward, the growth of the nucleus occurs in a vertical direction by the supply of adatoms such as direct impingement of gas phase reactants or surface diffusion of adatoms along the side walls of the nanorod. These nucleation and growth mechanisms result in high aspect ratio nanorods grown on the substrate without catalyst on the tip.

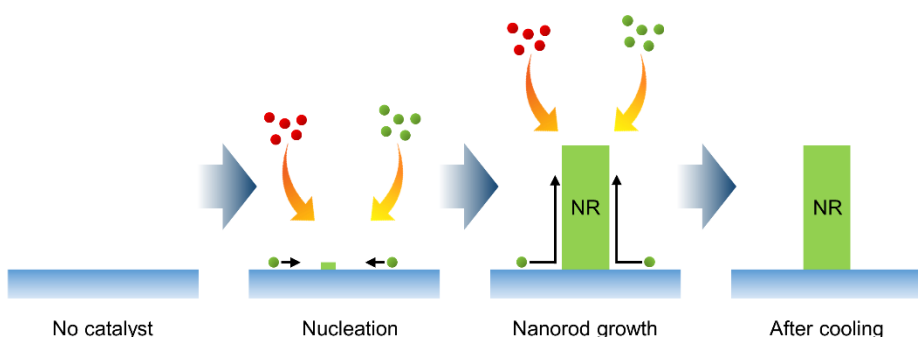


Figure 2.8. Schematic illustrations showing catalyst-free growth mechanism of nanorod.

2.2 Transmission electron microscopy

2.2.1 High-resolution TEM

High-resolution (HR) TEM imaging technique has been widely used to observe nano-sized objects and to identify their crystal structure for the last two decades. Lattice fringes obtained from the HR-TEM image reveal projected lattice structure of nanomaterials along a specific crystallographic zone axis, thereby allowing us to study their structural information. Thus this section describes how lattice fringes are generated at high magnification and how they are related to the crystal structure of nanomaterials.

HR-TEM image is a phase contrast image which is produced by interference between direct and many diffracted beams having different phase factors. Incident electron beam entering into a specimen is scattered inside the crystal. The scattering of the electron beam gives rise to exit waves at the bottom surface of the specimen, which consist of direct beam (ϕ_0) and diffracted beams (ϕ_g) exhibiting diffraction vector 0 and \vec{g} , respectively, as shown in Figure 2.9. Diffracted beams satisfying Bragg condition, denoted as $\pm g, \pm 2g, \pm 3g, \dots$, constructively interfere each other, thus forming diffraction patterns and images. In contrast to these diffracted beams, the other beams destructively interfere and cancel out each other.

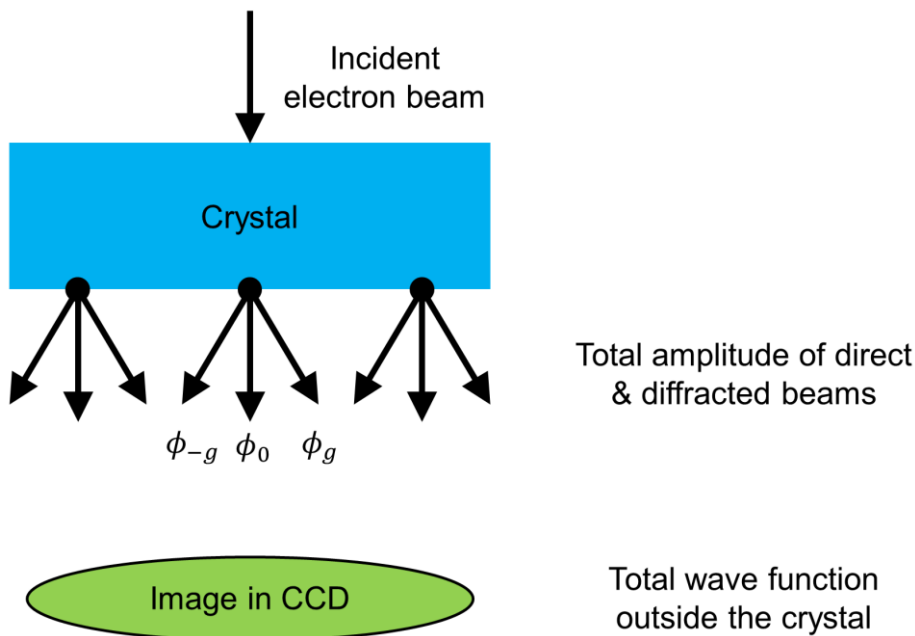


Figure 2.9. Schematic illustration showing the formation of direct and diffracted beams by the interaction with a crystal and their contribution to the image formation.

The total wave function passing through the specimen is represented as superposition of all the direct and diffracted beams.³⁰

$$\Psi = \phi_0 \exp(2\pi i \mathbf{k}_0 \cdot \mathbf{r}) + \phi_{g_1} \exp(2\pi i \mathbf{k}_{g_1} \cdot \mathbf{r}) + \phi_{g_2} \exp(2\pi i \mathbf{k}_{g_2} \cdot \mathbf{r}) + \dots \quad (2.16)$$

To simplify the derivation of equation representing the origin of lattice fringes, let us first consider two beam condition only with direct beam (ϕ_0) and diffracted beam (ϕ_g) as follows,

$$\Psi = \phi_0 \exp(2\pi i \mathbf{k}_0 \cdot \mathbf{r}) + \phi_g \exp(2\pi i \mathbf{k}_D \cdot \mathbf{r}) \quad (2.17)$$

$$\mathbf{k}_D = \mathbf{k}_0 + \mathbf{g} + \mathbf{s}_g = \mathbf{k}_0 + \mathbf{g}' \quad (2.18)$$

where the diffracted and direct beams are written as \mathbf{k}_D and \mathbf{k}_0 , and reciprocal lattice vector of the crystal and excitation error for the diffraction vector \vec{g} are represented as \mathbf{g} and \mathbf{s}_g , respectively.

According to the classical diffraction theory based on two-beam condition, the amplitude of diffracted beam ϕ_g can be written as

$$\phi_g = \frac{i}{\xi_g s_{eff}} \sin(\pi t s_{eff}) \exp(i\pi s_{eff} t) \quad (2.19)$$

$$s_{eff} = \sqrt{s^2 + \frac{1}{\xi_g^2}} \quad (2.20)$$

where ξ_g is characteristic length (or extinction distance) for the diffraction vector \vec{g} . By comparing with the form of Equation 2.19, the amplitude of direct and diffracted beam in Equation 2.17 can be simplified as follows,

$$\phi_0(z) = A \quad (2.21)$$

$$\phi_g(z) = B \exp(i\delta) \quad (2.22)$$

where

$$B = \frac{\pi}{\xi_g} \frac{\sin(\pi t s_{eff})}{\pi s_{eff}} \quad (2.23)$$

$$\delta = \frac{\pi}{2} - \pi t s_{eff} \quad (2.24)$$

The total wave function in Equation 2.17 is then given as

$$\Psi = \exp(2\pi i \mathbf{k}_0 \cdot \mathbf{r}) [A + B \exp\{i(2\pi \mathbf{g}' \cdot \mathbf{r} + \delta)\}] \quad (2.25)$$

The intensity of the total wave function which is recorded is written as

$$\begin{aligned} I &= |\Psi|^2 = A^2 + B^2 + AB[\exp\{i(2\pi \mathbf{g}' \cdot \mathbf{r} + \delta)\} + \exp\{-i(2\pi \mathbf{g}' \cdot \mathbf{r} + \delta)\}] \\ &= A^2 + B^2 + 2AB \cos(2\pi \mathbf{g}' \cdot \mathbf{r} + \delta) \\ &= A^2 + B^2 - 2AB \sin(2\pi \mathbf{g}' \cdot \mathbf{r} - \pi s t) \end{aligned} \quad (2.26)$$

Effective excitation error s_{eff} is simply expressed as s by assuming that the specimen is so thin. Let the direction of diffraction vector \mathbf{g}' is normal to that of incident electron beam path (\hat{z}) and parallel to that of x (\hat{x}) in a Cartesian coordinate. The Equation 2.26 then turns into

$$I = A^2 + B^2 - 2AB\sin(2\pi g'x - \pi st) \quad (2.27)$$

where g' is the amplitude of diffraction vector \mathbf{g}' .

Equation 2.27 is the main equation which explains the relationship between the lattice fringes and structural information of the specimen. The sine function in Equation 2.27 is responsible for the oscillatory intensity of the total wave function, which is the origin of the lattice fringes in HR-TEM image. The period of the sine function is $1/g' = d_g$ which is an interplanar spacing between the adjacent planes. This indicates that the lattice fringe spacing is identical to the interplanar spacing of d_g as illustrated in Figure 2.10. In addition, the direction in which the intensity varies sinusoidally suggests the plane normal direction of diffracted beam.

The derivation of total wavefunction and its intensity under multi-beam condition can be performed in the same way as the case of two-beam condition. Figure 2.11a shows direct and various diffracted beams selected by an objective aperture. Lattice fringes of HR-TEM image are illustrated in Figure 2.11b, which are generated by the interference of direct and many diffracted beams having different phase factors. Such lattice fringes include various structural information of the specimen, such as the direction of planes normal to the diffraction vector \mathbf{g}' , the angle between two planes, the interplanar spacing of the planes, and crystallographic symmetry of the specimen. Using these structural information obtained from lattice fringes in

HR-TEM image, crystal structure and crystallographic zone axis of the specimen can be identified.

The structural analysis performed in the present work employs aforementioned properties of HR-TEM imaging technique. The thing which should be noted is that the lattice fringes in HR-TEM image do not directly reveal atomic structure of the specimen. They are phase contrast image obtained by the interference between direct and diffracted beams, thus providing the information on the interplanar spacing and crystallographic orientations, not the direct location of the specific atoms in the specimen.

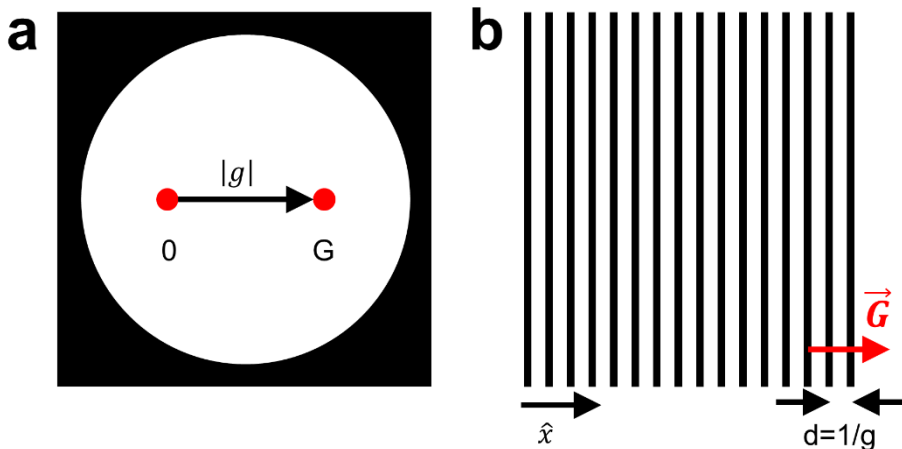


Figure 2.10. Lattice fringes created under two-beam condition. (a) Direct and diffracted beam, as represented 0 and \vec{G} , selected by an objective aperture for the two-beam condition. (b) Lattice fringes of HR-TEM image formed under two-beam condition in (a).

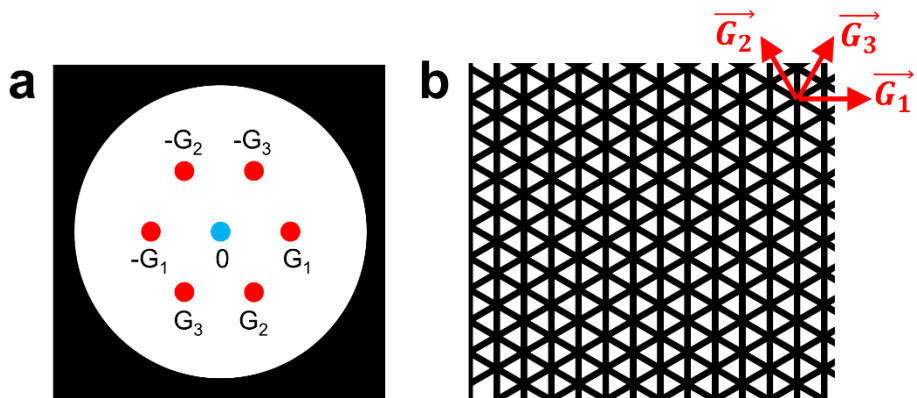


Figure 2.11. Lattice fringes created under multi-beam condition. (a) Direct and diffracted beams, as represented 0 , \vec{G}_1 , \vec{G}_2 , and \vec{G}_3 , selected by an objective aperture for the two-beam condition. (b) Lattice fringes of HR-TEM image formed under multi-beam condition in (a).

CHAPTER 3

Experimental Methods

In this chapter, experimental details including the fabrication of graphene templates, crystal growth, apparatus, and characterization techniques are discussed. First, detailed methods on the fabrication of graphene template are explained as a starting point to perform “direct growth and observation” method. Graphene template is made by graphene layers placed on a conventional TEM grid, such as lacey carbon grid, or a prefabricated SiNx membrane-coated TEM grid. Additionally, various kinds of materials growth on the graphene template are described in detail. Two different types of growth systems such as metal-organic chemical vapor deposition (MOCVD) and molecular beam epitaxy (MBE) are employed to grow compound semiconductor nanostructures on graphene. Lastly, materials characterizations using scanning electron microscopy (SEM), TEM, and RHEED and their operating conditions are considered.

3.1 Fabrication of graphene templates

3.1.1 Growth of CVD graphene

Graphene layers were grown on copper foil (25- μm -thick, Alfa Aesar) in a chemical vapor deposition (CVD) furnace. Schematic illustration of the homemade furnace are shown in Figure 3.1. Copper foil was cut into small pieces which fit the size of a quartz boat and cleaned with acetone and methanol. A quartz boat containing copper foil was loaded at the hot zone of a tube furnace. Before the growth, copper foil was annealed at 1000 °C for 30 min while introducing only hydrogen as an ambient gas. During the growth of CVD graphene, methane gas was injected into the reactor with hydrogen as a carrier gas. The growth was carried out at 1000 °C for 30 min, and the reactor pressure was kept at 150–200 Torr for multi-layered graphene (MLG) and at base pressure for single-layered graphene (SLG). After the growth of 30 min, the furnace was cooled in air down to room temperature. Detailed growth conditions of CVD graphene are summarized in Table 3.1.

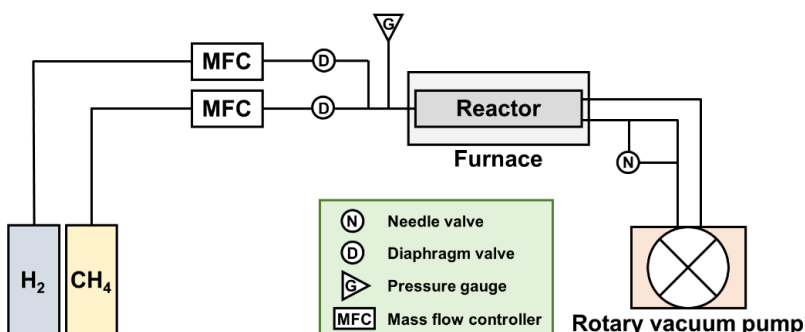


Figure 3.1. Schematic illustration of homemade CVD furnace chamber.

Table 3.1. Growth conditions for CVD graphene

Growth conditions	
Substrate	Copper foil
Reactor pressure [Torr]	150–200 (for MLG) Base pressure (for SLG)
Growth temperature [°C]	1000
Growth time [min]	30
Anneal time [min]	30
CH ₄ flow rate [sccm]	35
H ₂ flow rate [sccm]	100

3.1.2 Fabrication of SiNx membrane TEM grid

New type of TEM grid containing Si wafer with a perforated amorphous SiNx membrane was fabricated as an alternative of conventional Quantifoil TEM grid. Firstly, a SiNx membrane-coated Si wafer was prepared. Si(100) wafer with a thickness of 200 μm was purchased from Crystal bank (Pusan National University). SiNx thin films with a thickness of ~200 nm were then deposited on both sides of Si wafer by plasma enhanced CVD (PECVD) method. The deposition was carried out at 200–300 °C in a vacuum chamber with SiH₄ gas introduced.

For the selective etching of SiNx thin films, lithography and dry

etching processes were employed. Photoresist (AZ5214) was spin-coated on the backside of SiNx membrane-covered Si wafer for 1 min with a spin speed of 3000 rpm. Afterward, the sample was baked at 90 °C for 1 min. Photolithography was then used to define the shape of hole patterns on the photoresist layer. Ultraviolet radiation (UV ramp) was selectively illuminated on the photoresist layer with a mask containing an array of square-shaped hole which is 400 µm on a side. The UV-exposed sample was dipped into an aqueous developer (MIF 500, MicroChem.) for 90 s at room temperature and rinsed with deionized (DI) water for 30 s. After that, reactive ion etching (RIE) was employed for 5 min to remove the SiNx thin films in a shape of a photomask. The photoresist left on the backside of Si wafer was eliminated by etching with acetone for 10 min, followed by rinsing with isopropyl alcohol (IPA).

The hole patterns of SiNx membrane was fabricated by anisotropic wet etching of Si wafer, followed by lithography and dry etching processes. The Si wafer was anisotropically and selectively etched using 30% KOH solution and a SiNx mask on the backside. Si(111) planes etch at a much slower rate than Si(100) planes in a KOH solution (e.g. 1 µm etched in a direction of [100] at 1 min). Such anisotropic etching makes a hole only in a direction of [100] while remaining (111) planes almost intact. The sample was placed in a solution of 30% KOH heated at 85 °C for ~ 3 hr, followed by rinsing with deionized (DI) water more than three times. Afterward, poly(methyl methacrylate) (PMMA 950K, 11%) was spin-coated on the front side of Si wafer for e-beam lithography. The spin coating was performed for 1 min with a spin speed of

4000 rpm. The sample was then baked at 180 °C for 90 s. The e-beam lithography was conducted by field emission (FE)-SEM to define an array of hole patterns on the PMMA coating layer. Hole patterns were in the range of 0.5–2 µm in diameter. The sample was then dipped into a mixed solution of Methyl Isobutyl Ketone (MIBK) and IPA with a ratio of 1:3 for 90 s at room temperature, followed by rinsing with DI water for 30 s. Such an array of hole patterns was perforated by additional RIE process in the same conditions as performed right after photolithography and developing. Lastly, the PMMA layer left on the front side of Si wafer was removed by etching with O₂ plasma treatment for 60 s and with acetone for more than 1 hr.

The whole fabrication processes of SiNx membrane TEM grid mentioned above are schematically illustrated in Figure 3.2. The detailed conditions at each step was also summarized in Table 3.2.

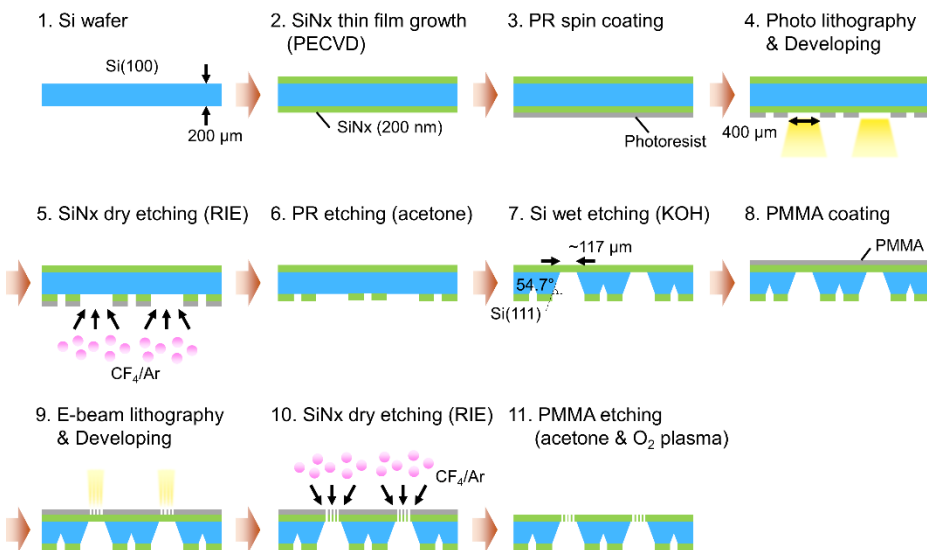


Figure 3.2. Overall fabrication processes of SiNx membrane TEM grid

Table 3.1. Processing conditions for the fabrication of SiNx membrane TEM grid at each step

	Processing conditions
1. Si(100) wafer surface	Crystal bank (Pusan National University)
2. SiNx thin film growth	Deposition: PECVD Temperature: 200–300 °C
3. Photoresist spin coating	Photoresist: AZ5214 Spin speed: 3000 rpm Coating time: 1 min Baking temperature: 90 °C Baking time: 1 min
4. Photolithography /Developing	Exposure time: 10s (UV ramp) Developing time: 90 s (MIF 500) Rinsing time: 30s (IPA)
5. RIE (SiNx etching)	Gas flow rate: CF ₄ :Ar = 45:5 sccm Chamber pressure: 50 mTorr Plasma power: 150 W Etching time: 300 s
6. Photoresist etching	Etching time: 10 min (acetone)
7. Si wafer wet etching	Etching time: 3 hr (30% KOH) Temperature: 85 °C
8. PMMA spin coating	PMMA: PMMA 950K, 11% Spin speed: 4000 rpm

	Coating time: 1 min
	Baking temperature: 180 °C
	Baking time: 90 s
	Dose factor: 600 µC/cm ² (FE-SEM)
9. E-beam lithography	Beam current: 500 pA
/Developing	Developing time: 90 s (MIBK:IPA=1:3)
	Rinsing time: 30s (IPA)
	Gas flow rate: CF ₄ :Ar = 45:5 sccm
10. RIE (SiNx etching)	Chamber pressure: 50 mTorr
	Plasma power: 150 W
	Etching time: 300 s
	O ₂ plasma etching time: 60 s
11. PMMA etching	O ₂ plasma power: 50 W
	Chamber pressure: 100 mTorr
	Etching time: 10 min (acetone)

3.1.3 Graphene transfer

After the growth of CVD graphene, PMMA (PMMA 950K, 11%) was spin-coated onto graphene for 10 s with a spin speed of 1000 rpm and for additional 50 s with a spin speed of 4000 rpm. Afterward, PMMA-coated graphene was baked at 140 °C for 90 s. The graphene layers on the other side of the copper foil was then removed by O₂ plasma treatment. The graphene layers were separated from the copper foil by etching it away using a solution of ammonium persulfate ((NH₄)₂S₂O₈) (0.04 g·mL⁻¹). Afterward, PMMA-supported graphene floating in the solution was rinsed several times using DI water and carefully lifted by TEM grids (Quantifoil holey carbon grid, Ted Pella) or prefabricated SiNx membrane TEM grid. The graphene transferred on TEM grids were then dried using hot plate at ~110 °C for more than 15 min to improve adhesion with supporting layers of TEM grids. PMMA coating layer was removed by heating the graphene/TEM grids templates in acetone at 60–80 °C for more than 30 min. This eventually completed manufacturing the graphene templates which will be used for both crystal growth and TEM measurements within a framework of “direct growth and observation” method. The polymer residues left on the graphene surface were further eliminated by heating the templates at high temperature of more than 600 °C in a growth chamber just before the crystal growth began.

3.2 Materials growth

3.2.1 ZnO nanomaterials on a graphene template

Oxygen plasma was treated on the surface of graphene layers placed on a Quantifoil TEM grid for 3 s to increase the nucleation sites over the whole surface area of graphene. Afterward, the graphene template was loaded into the MOCVD reactor, and ZnO nanomaterials were directly grown on graphene layers using catalyst-free MOCVD system for various growth times (10 and 30 s, and 1, 2, 5, 10, and 15 min). The homemade vertical-type 2-inch MOCVD chamber is schematically illustrated in Figure 3.3. Diethylzinc and O₂ gas were injected into the reactor, with Ar as a carrier gas. The reactor temperature was raised up to 580–600 °C for 12 min and kept at this temperature for additional 10 min before the growth to stabilize high reactor temperature. The reactor pressure was kept at ~2 Torr during the whole growth process. Detailed growth conditions are given in Table 3.3.

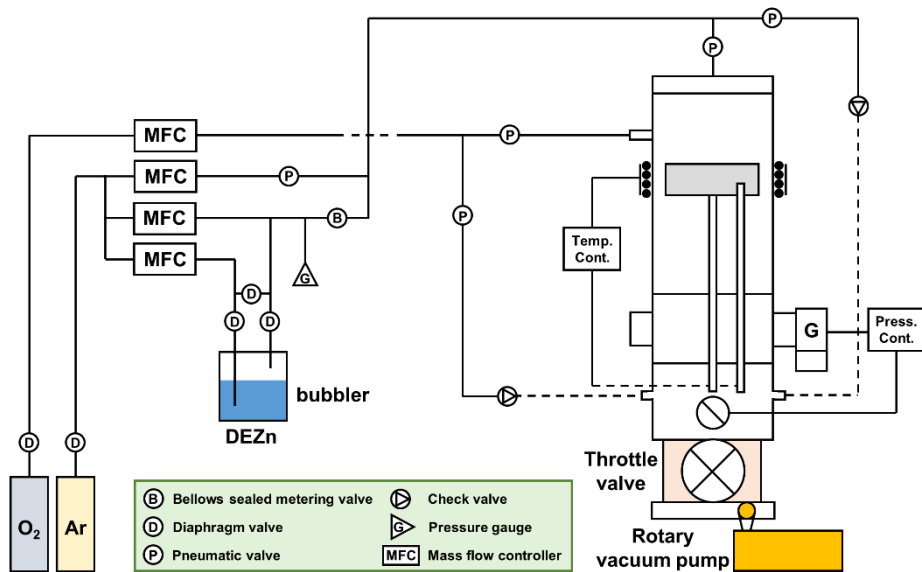


Figure 3.3. Schematic illustration of homemade vertical-type 2-inch MOCVD chamber

Table 3.2. Growth conditions for ZnO nanomaterials on graphene

Growth conditions	
Substrate	Graphene
Reactor pressure [Torr]	~ 2
Growth temperature [°C]	580–600
Growth time [min]	1/6, 1/2, 1, 2, 5, 10, and 15
DEZn flow rate [sccm]	20
DEZn dilute flow rate [sccm]	40
O ₂ flow rate [sccm]	100
Ar flow rate [sccm]	1500
Bubbler temperature of DEZn [°C]	-15

3.2.2 GaAs/SLG/InAs double heterostructures

GaAs and InAs nanomaterials were grown on both sides of SLG and MLG by catalyst-free MBE. Firstly, InAs nanorods were grown on the backside of graphene suspended by holes in the SiNx membrane TEM grid. The InAs nanorods were grown at ~450 °C for a short time of 30 s in a cryogenically cooled ultra-high vacuum MBE growth chamber (RIBER 32P) using high-purity In and uncracked As₄ molecular beams from Knudsen cells. Schematic illustration of the MBE system is presented in Figure 3.4. The As₄ was supplied to the Si(111) substrate 10 min before supplying the In to prevent the formation of In droplet on the surface of graphene.

After the growth of InAs nanorods, the graphene template was loaded in the MBE chamber up-side-down to grow GaAs nanomaterials on the other side of graphene suspended by holes in the SiNx membrane TEM grid. The GaAs nanomaterials were grown at ~450 °C for a short time of 30 s in a cryogenically cooled ultra-high vacuum MBE growth chamber (RIBER 32P) using high-purity Ga and uncracked As₄ molecular beams from Knudsen cells. The As₄ was supplied to the Si(111) substrate 10 min before supplying the Ga to prevent the formation of Ga droplet on the surface of graphene. Detailed growth conditions are described in Table 3.4.

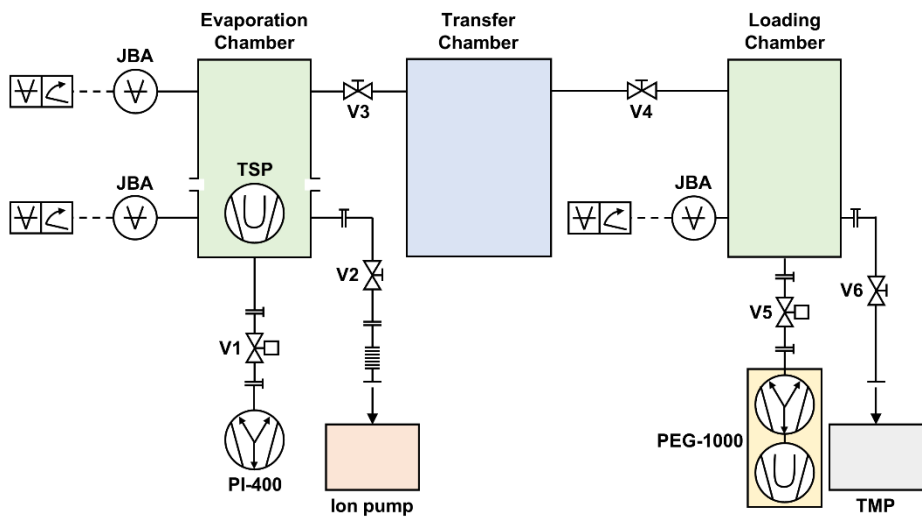


Figure 3.4. Schematic illustration of MBE system (RIBER 32P)

Chapter 3: Experimental Methods

Table 3.3. Growth conditions for GaAs/SLG/InAs double heterostructures

	InAs	GaAs
Substrate	SLG and MLG	
Target morphology	Nanorods	Thin films
Reactor pressure [Torr]	2.4×10^{-7}	2.4×10^{-7}
Growth temperature [°C]	450	450
Growth time [min]	0.5	0.5
Effusion cell temp. [°C]	750 (In) 360 (As)	950 (Ga) 320 (As)
Beam equivalent pressure [Torr]	8.0×10^{-8} (In) 5.0×10^{-5} (As)	1.0×10^{-7} (Ga) 5.0×10^{-6} (As)

3.2.3 InAs coaxial nanorods on Si(111) and graphene

InAs nanorods and $\text{In}_x\text{Ga}_{1-x}\text{As}(\text{GaAs})/\text{InAs}$ coaxial nanorods were grown by catalyst-free MBE on an oxide-etched Si(111) substrate. Oxide-free Si surface was prepared by etching oxidation layers on the surface of Si(111) wafer with buffered oxide etch for 30 s and cleaning in DI water for 30 s. High-temperature annealing was followed inside an ultrahigh-vacuum preparation chamber heated at 650 °C for 10 min with As_4 introduced. The InAs nanorods were grown at ~500 °C in a cryogenically cooled ultrahigh-vacuum MBE growth chamber (RIBER 32P) using high-purity In and uncracked As_4 molecular beams from Knudsen cells. Schematic illustration of the MBE system is presented in Figure 3.4. The As_4 was supplied to the Si(111) substrate 10 min before supplying the In to prevent the formation of In droplet on the substrate.

In order to investigate the initial stage of InAs nanorods growth, the growth was conducted only for a short time of 30–85 s. To obtain high-quality and well-controlled $\text{In}_x\text{Ga}_{1-x}\text{As}(\text{GaAs})/\text{InAs}$ coaxial nanorods, a two-step growth procedure was performed. For the growth of $\text{In}_x\text{Ga}_{1-x}\text{As}/\text{InAs}$ coaxial nanorods, InAs core nanorods were first grown at 500 °C for 36 min and $\text{In}_x\text{Ga}_{1-x}\text{As}$ shell layers were subsequently grown on the InAs core nanorods at 400 °C for 40 min using an additional Ga molecular beam. GaAs/InAs coaxial nanorods were also prepared as a control group by growing InAs nanorods at 480 °C for 150 s and coating GaAs shell layers on the InAs core nanorods at 400 °C for 15 min. Detailed growth conditions are described in Table 3.5.

Table 3.4. Growth conditions for InAs nanorods and $In_xGa_{1-x}As(GaAs)/InAs$ coaxial nanorods

	Initial stage	GaAs/InAs coaxial nanorod		$In_xGa_{1-x}As/InAs$ coaxial nanorod	
	InAs nanorod	InAs nanorod	GaAs coating	InAs nanorod	$In_xGa_{1-x}As$ coating
Substrate					Si(111) wafer and graphene
Reactor pressure [Torr]	1.0×10^{-7}	1.0×10^{-7}	1.0×10^{-7}	1.7×10^{-7}	1.7×10^{-7}
Growth temperature [$^{\circ}\text{C}$]	500	500	400	480	400
Growth time [min]	0.5	2.5	15	36	40
Effusion cell temp. [$^{\circ}\text{C}$]	750 (In) 360 (As)	720 (In) 360 (As)	850 (Ga) 430 (As)	790 (In) 360 (As)	850 (In) 360 (As)
Beam equivalent pressure [Torr]	0.9×10^{-7} (In) 7.7×10^{-5} (As)	1.2×10^{-5} (As)	4.5×10^{-5} (As)	4.5×10^{-5} (As)	4.5×10^{-5} (As)

3.3 Materials characterization

3.3.1 Scanning electron microscopy

The surface morphology of compound semiconductor nanostructures grown on graphene layers was characterized using a FE-SEM instrument (AURIGA and MERLIN Compact, Carl Zeiss). In-lens secondary electron detector is equipped to these SEM for high-resolution and contrast imaging. The acceleration voltage was set to 2 and 3 kV with a working distance of ~3.8 and 5.8 mm for AURIGA and MERLIN Compact, respectively.

3.3.2 Transmission electron microscopy

To investigate the crystal structure and epitaxial relationship of nanomaterials with graphene, TEM measurements were performed. Plan-view samples were prepared without post specimen preparation processes through “direct growth and observation” method, as already mentioned in Chapters 3.1 and 3.2. For the plan-view imaging of nanorods, they were dispersed in anhydrous ethanol by sonication and dropped onto a holey carbon-coated TEM grid. Cross-sectional samples were fabricated by FIB milling in a FEI-Helios 650 FIB instrument. FIB lamella was further milled using Ar ion milling machine (Model 1040 Nanomill, Fischione) to remove damaged layer caused by FIB process and thin the lamella.

Bright-field (BF), HR-TEM images, and selected area electron diffraction (SAED) were obtained with a 200-kV field-emission TEM

instrument (FEI Tecnai F20 and JEOL JEM-2100F). Elemental mapping of nanomaterials were performed with silicon drift detector-based energy dispersive X-ray spectroscopy (EDS) system together with AZTEC software (Oxford instruments, UK). Atomic-resolution images of graphene layers were taken with an aberration-corrected TEM equipped with a CEOS image corrector and XFEG (Titan G2 60-300, FEI) operated at 80 kV. In order to avoid knock-on damage of high-energy electron beam on a vulnerable graphene, low acceleration voltage of 80 kV was chosen for atomic-resolution imaging. HR-TEM images were mostly acquired within a hole over the underlying amorphous carbon layer and SiNx membrane to avoid the electron-beam scattering effect from the underlying layer. Crystal structures of nanomaterials were investigated by analyzing the fast Fourier transform (FFT) patterns of the HR-TEM images.

3.3.3 Reflection high-energy electron diffraction

The entire growth process of nanostructures was monitored in real time in an MBE chamber. The electron beam with an electron beam energy of 22.2 keV and a spot size of 0.2 mm was emitted from the electron gun (KSA 400, KSA, Inc.). The length of the electron-beam irradiated along the beam trajectory was 15 mm, indicating a *ca.* 0.8° incident angle of the electron beam with respect to the substrate surface. Real-time videos of the RHEED patterns were acquired using a commercial digital single-lens reflex camera having a time resolution of 0.04 s. The lattice parameters of the nanostructure such as

Chapter 3: Experimental Methods

InAs nanorods and $\text{In}_x\text{Ga}_{1-x}\text{As}(\text{GaAs})/\text{InAs}$ coaxial nanorods were estimated by comparing the spacings between the RHEED spots with those of the Si(111) substrate as a reference. Snapshot of RHEED patterns were taken while the nanorod growth was temporarily ceased by closing the In and Ga shutters and by stopping rotation of the substrate.

CHAPTER 4

Atomic-resolution observation of nucleation and growth behavior of ZnO nanomaterials on a graphene template

This chapter describes the initial growth mechanisms of ZnO nanomaterials on graphene layers. For the imaging and investigation of the growth behavior of nanomaterials at the atomic scale without conventional TEM sample preparation processes, the “direct growth and observation” technique using a graphene template is newly introduced. Before applying the method in practice, its feasibility and reliability for the crystal growth as well as TEM measurements are confirmed. Then, using this method, the growth behavior of ZnO nanomaterials on graphene layers including the nucleation of ZnO cubic phase and the formation of $\Sigma 7$ coincidence site lattice (CSL) boundary is explained in detail, which were not known before.

4.1 Introduction

Studying nucleation and growth is one of the major goals in materials science. Fundamental understanding of the initial growth behavior, including how nuclei are formed and how they evolve into nanostructures, is essential for fabrication of nanomaterials with desired physical properties. Recently, graphene-based hybrid heterostructures are growing as promising candidate for fabricating next-generation optoelectronic and electronic devices. Particularly, ZnO reveals its potentials for the application into the transparent conducting electrode and optoelectronic devices such as LED due to its direct and large bandgap (3.3 eV) and large exciton binding energy (60 meV). Thus, there have been many efforts to grow ZnO on graphene and to fabricate multi-functional devices.^{13,14,16} However, developing such hybrid heterostructures based on graphene are being delayed due to the lack of knowledge on the growth mechanisms of compound semiconductor nanostructures on graphene.

For understanding the growth behavior of nanomaterials in detail, atomic level investigation on the crystal structure of as-grown nuclei and local atomic arrangements of nearby defects is required. Such high-resolution study along with crystallographic analysis could be performed using TEM. Nevertheless, the destructiveness of the conventional TEM sample preparation processes makes it difficult to image nanomaterials at the atomic scale.²² So far, the method growing nanomaterials directly on prefabricated thin membranes, such as Si₃N₄ and SiO₂, has been developed for imaging as-grown nanomaterials by TEM to avoid damages during typical TEM sample

preparation processes.^{23,25} However, these membranes are not suitable for the atomic-scale investigation of initial growth mechanisms since a few tens of nanometers-thick-membranes contribute to significant electron beam scattering which might prevent clear imaging of nano-sized objects. Additionally, amorphous characteristics of these membranes cannot be used as conventional substrates for the crystal growth. Therefore, the development of new method for imaging and analyzing the growth mechanisms of nanomaterials are essentially required.

4.2 Direct growth and observation of nanomaterials using a graphene template

In order to observe the nano-sized materials without damages during the TEM sample preparation processes, a new method, so called “direct growth and observation” technique, is introduced. This method modifies the previous methods using prefabricated thin membranes, such as Si_3N_4 and SiO_2 , by exploiting a graphene as an alternative. Graphene exhibiting excellent electron beam transparency and high mechanical strength is an ideal supporting layer for TEM measurements by minimizing the background signal from the underlying membrane. In addition to merely sustaining nanomaterials as a support, graphene can be further used as a crystalline substrate for nanomaterials growth. The crystalline nature of graphene along with its electron beam transparency ultimately enables direct imaging of nanomaterials and allows us to systematically investigate the initial growth mechanisms without typical TEM sample preparation processes.

The “direct growth and observation” method using a graphene template is schematically represented in Figure 4.1.³¹ This figure introduces the experimental procedures step by step. Graphene layers were deposited on a Cu foil by CVD method. PMMA was spin-coated on the surface of graphene to support ultra-thin graphene layers during transfer process. The PMMA-supported graphene was transferred onto a Cu mesh TEM grid with a perforated amorphous carbon supporting layer. After etching PMMA layer with acetone, O_2 plasma was treated on the surface of the graphene to enhance the nucleation

sites. This graphene on TEM grid template was loaded into an MOCVD chamber, and ZnO nanostructures were grown on the graphene layers. After the growth, the template was directly loaded in a TEM without TEM sample preparation processes. The free-standing graphene on perforated region of the amorphous carbon supporting layer was observed using TEM to investigate the nucleation and initial growth behavior of ZnO nanomaterials with atomic-resolution.

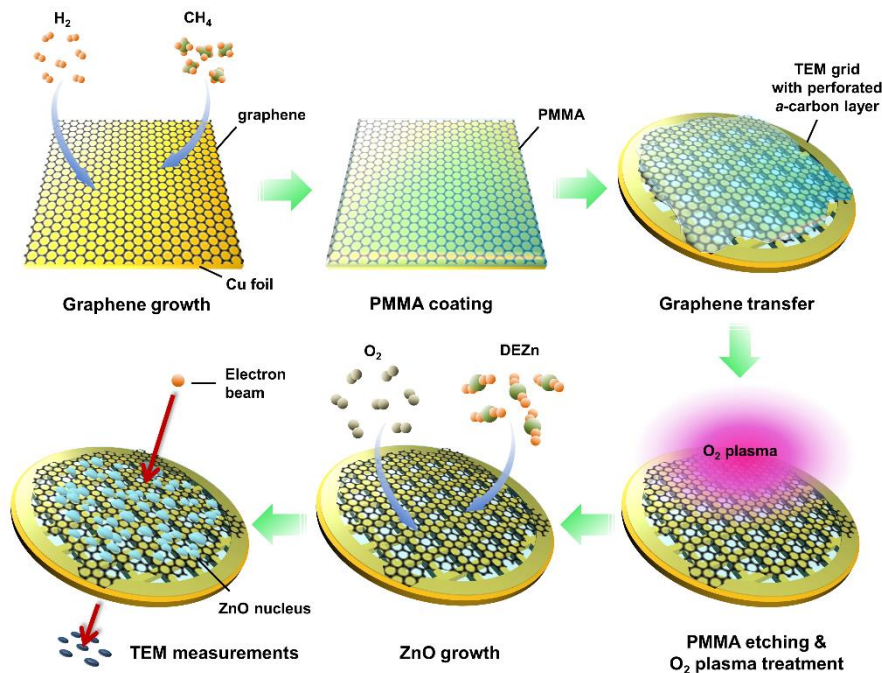


Figure 4.1. Schematic diagram of the “direct growth and observation” technique for growing ZnO nanomaterials on graphene and performing TEM measurements. Graphene was grown by CVD method and transferred onto a Cu mesh TEM grid with a perforated amorphous carbon supporting layer. The graphene surface was exposed to O₂ plasma to enhance nucleation of nanomaterials. ZnO nanomaterials were then grown on the plasma-treated graphene layers by MOCVD method and observed using TEM. No additional TEM sample preparation processes, such as manual grinding or ion milling, was carried.³¹

4.3 Feasibility of the new method for crystal growth and TEM measurements

Feasibility of the graphene/TEM grid system as a template for crystal growth and TEM measurements was verified by various ways, such as optical microscopy (OM), SEM, and TEM measurements. Thermal, mechanical, and chemical stabilities of the graphene/TEM grid template at high growth temperature were thoroughly confirmed. ZnO nanomaterials were grown on the graphene template for 15 min at 580–600 °C using catalyst-free MOCVD method under the growth condition as mentioned in Chapter 3.2.1. Figure 4.2 shows that the TEM grid and graphene withstood high temperature and kept their shapes during the whole growth process.³¹ Although the graphene/amorphous carbon layers have rough surface, OM image in Figure 4.2b clearly shows that graphene and underlying perforated amorphous carbon layer still remained intact. These findings reveal that the graphene/TEM grid template remained in a fairly good condition even after the high temperature growth process. In addition, the robustness of the template indicates that the following characterization steps, such as SEM and TEM, can be performed without any problem.

The graphene/TEM grid template showed capability of acquiring clear atomic-resolution images. Figure 4.3 reveals HR-TEM images of ZnO nanomaterials taken in the region of free-standing graphene. Since the graphene minimizes electron beam scattering because of its thinness and low atomic number, background signals arising from underlying graphene supporting

layers were rarely detected on the image, compared with conventional thick and amorphous supporting layers. High mechanical strength of graphene also allowed us to grow nanomaterials on the regions of free-standing graphene, which is beneficial for eliminating the background signal from underlying amorphous carbon layer of a TEM grid. Furthermore, it was verified that ZnO nanostructures grew on the graphene template in the same manner as they did on graphene lying on arbitrary substrates. This ensures that the system can be exploited to investigate the general growth behavior of the ZnO nanomaterials on graphene.

The graphene, which was used as an ideal substrate as well as a supporting layer, provided benefits for crystal growth and TEM measurements. The OM and TEM images showed that the free-standing region of the graphene was intact after the growth process. In addition, ZnO nanostructures grown on the free-standing graphene stayed stable under various measurements. This indicates that our system is feasible to investigate the nucleation and growth behavior of ZnO nanomaterials on graphene substrate.

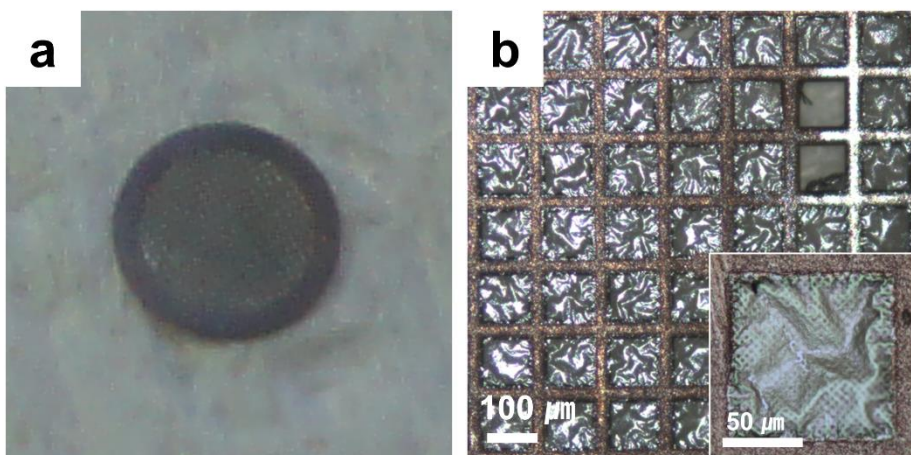


Figure 4.2. Feasibility of a graphene/TEM grid template for nanomaterials growth and TEM measurements. (a) Photograph of the template after the growth of ZnO nanomaterials. This shows that the TEM grid maintained its structure after the growth at 580 °C for 15 min. (b) OM image of the template. The inset is a magnified OM image of a TEM mesh, showing micrometer-sized holes with an amorphous carbon layer underneath the graphene.³¹

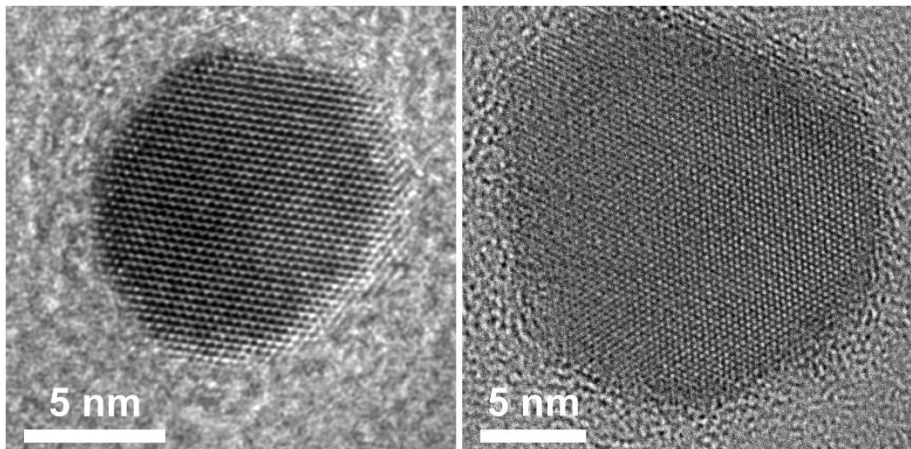


Figure 4.3. Atomic-resolution images of ZnO nanomaterials grown on a graphene layers

4.4 Growth mechanism of ZnO nanomaterials on graphene

4.4.1 Nucleation

First, nucleation of ZnO nanomaterials was dealt with using “direct growth and observation” method. In general, it is difficult to inspect crystallographic information of individual nucleus using BF images and diffraction patterns, since any significant information was not accessible by those methods due to small size of nucleus. However, “direct growth and observation” method using a graphene as an ideal substrate as well as a supporting layer facilitated atomic-resolution imaging, thereby particularly enabling investigation of the initial growth behavior of nanomaterials more precisely.

Figure 4.4a–c shows HR-TEM images of ZnO nucleus grown on graphene.³¹ ZnO nuclei grown for 10 s mostly had rounded shapes and incompletely crystallized atomic arrangement as shown in Figure 4.4a. Interestingly, the most noticeable finding was that ZnO nuclei with a rocksalt cubic structure were frequently observed in this growth stage, whereas ZnO nuclei with a hexagonal structure were not found.³² All of the rocksalt ZnO nuclei were grown along a direction of $\langle 110 \rangle$ as confirmed by FFT (the inset of Figure 4.4a). Such a rocksalt ZnO phase was not observed any more in the growth time of 1 min (Figure 4.4b). All the ZnO nucleus with a size of a few tens of nanometers revealed only hexagonal wurtzite structure grown along a

direction of $\langle 0001 \rangle$ (the inset of Figure 4.4b) as well as hexagonal faceted shape.

It is quite surprising that the rocksalt ZnO structure was found at the initial stage of growth (*e.g.* nucleation) because it has been mostly formed at specific growth conditions such as extremely high pressure and cubic substrate.³²⁻³⁴ This is attributed to the structural stability of the alternating form, the wurtzite ZnO, compared with the metastable cubic ZnO.

Additional experiments were carried out to better understand the behavior that the cubic ZnO structure was transformed into hexagonal ZnO structure as the growth proceeded. After the growth of ZnO on graphene for a short time of 10 s to obtain nuclei with the cubic phase, the sample was kept in an MOCVD reactor for another 6 min at the same growth temperature of 580–600 °C without introducing a precursor gas of DEZn. Figure 4.4c shows that the size of ZnO nucleus remained the same as that of the 10 s-grown nucleus. However, all the cubic ZnO structure observed at the nucleation stage totally disappeared, and only the nuclei with hexagonal phase and well-defined hexagonal facets were observed, as is the case for 1 min-grown ZnO. This result demonstrates that the ZnO nucleus forms thermodynamically stable hexagonal ZnO phase when provided with sufficient time and energy.

These experimental findings provide explanation for the appearance of metastable cubic ZnO structure in the early growth stage in conjunction with kinetics of nucleation.³¹ In heterogeneous nucleation procedure, the embryo that overcomes nucleation barrier only form nuclei on substrates, suggesting

that the height of the nucleation barrier is a critical factor in nucleation process^{27,35}. Nucleation and growth of these nuclei is then determined by competition between two factors; an increase in interfacial energy and decrease in bulk Gibbs free energy for the creation of new phase. Particularly, for an early growth stage, interfacial energy becomes a predominant factor determining the nucleation barrier of the initial growth stage because of a relatively large interfacial area to volume ratio of nanomaterials. Since the interfacial energy strongly depends on how the lattices match each other at the interface, atomic arrangements of ZnO and graphene at the interface were investigated using ball-and-stick model as shown in Figure 4.4d.

When the kinetic energy barrier, proportional to the interface energy in the case of heteroepitaxial growth, for a metastable structure is much lower than that for a stable structure, then the transition to the metastable state can be prevalent at the very initial stage of the growth^{27,35}. As illustrated in Figure 4.4d, the epitaxial relationships of ZnO [001]_c || graphene [1010]_h and ZnO [110]_c || graphene [1210]_h for cubic ZnO, and ZnO [1010]_h || graphene [1010]_h and ZnO [1210]_h || graphene [1210]_h for hexagonal ZnO are verified. In this case, the cubic ZnO matches graphene substrate with ratios of nearly 1:1 and 4:5 in lattice parameters along X and Y directions, respectively. On the other hand, the hexagonal ZnO matches graphene substrate with ratios of 3:4 in lattice parameters along both X and Y directions. This suggests better lattice matches at the interface between cubic ZnO and graphene, compared to that between hexagonal ZnO and graphene, which indicates lower nucleation energy barrier

for cubic ZnO phase on graphene. Therefore, relatively low nucleation energy barrier of cubic ZnO grown on graphene can preferentially lead to the formation of cubic structure of ZnO as an intermediate state. The detailed knowledge on the nucleation barrier for the heterogeneous nucleation is described in Chapter 2.1.1.

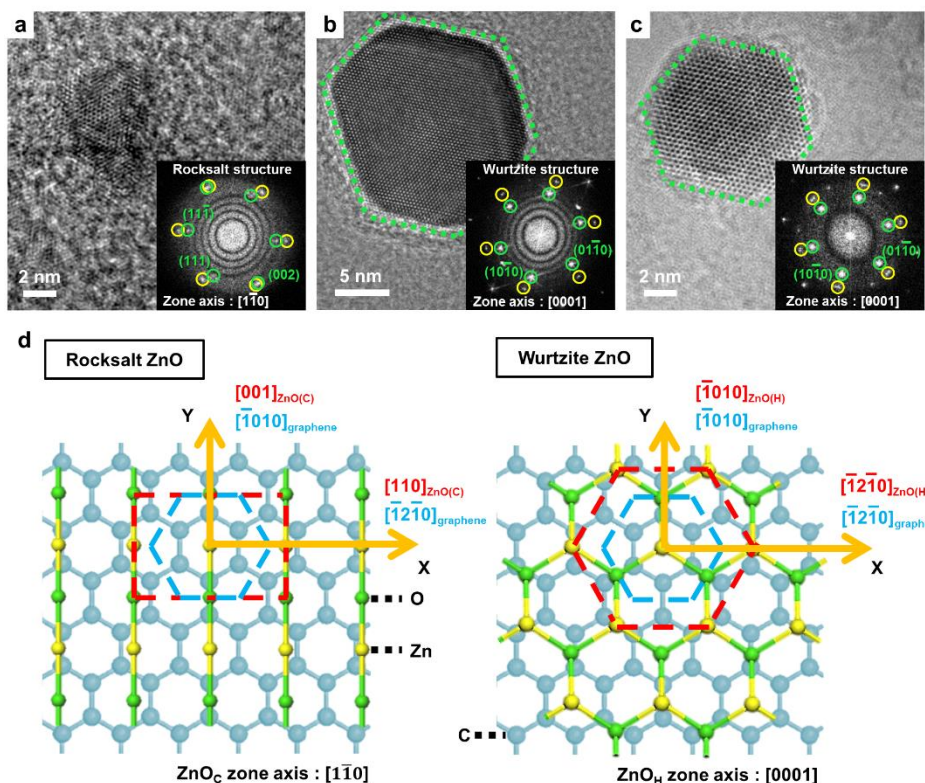


Figure 4.4. Crystal structure transition of ZnO nucleus from cubic to hexagonal in the early growth stage. (a,b) HR-TEM images of ZnO nucleus obtained for growth times of (a) 10 s and (b) 1 min. (c) HR-TEM image of ZnO grown for 10 s, the same as (a), and left in a reactor for another 6 min afterward with only O₂ gas introduced. The corresponding FFTs and zone axes are provided in each figure. In the insets, the diffraction peaks of ZnO and graphene are marked with green and yellow circles, respectively. (d) Epitaxial relationships between rocksalt/wurtzite ZnO and graphene illustrated using a ball-and-stick model. The C, O, and Zn atoms are represented by blue, green, and yellow balls, respectively. Both rocksalt and wurtzite structures are placed on a basal plane of graphene, and their projected unit cells, along with their zone axes, are identified in the figure with red and blue dashed lines.³¹

4.4.2 Grain boundary formation

After nucleation and growth of nuclei, they extensively coalesced into larger grains. During the coalescence, various kinds of grain boundaries formed at the interface where the grains met each other. Atomic configurations of such grain boundaries were investigated in detail using plan-view HR-TEM imaging of the 10 and 15 min-grown samples.³¹

BF image in Figure 4.5a shows many kinds of low-angle grain boundaries, indicated by dashed lines, and high-angle grain boundaries. It is worth noting that most of the low-angle grain boundaries commonly exhibited zig-zag atomic configurations retaining the {10̄10} facets of ZnO. This step-like boundaries incorporating stable {10̄10} ZnO planes, instead of straight boundaries with high-index plane, can possibly minimize the grain boundary formation energy over the whole area.

A comprehensive HR-TEM measurements revealed that many of these low-angle grain boundaries in the ZnO/graphene system corresponded to the [0001]-tilt grain boundaries which were typically observed in the fully-grown ZnO thin film^{36,37}. Figure 4.5b shows one of the low-angle grain boundaries consisting of an array of dislocation cores in a curved line. The periodic dislocation cores revealed strong contrast arising from local stain fields around the core.

Detailed atomic configurations nearby the low-angle grain boundaries were further studied by a magnified image of Figure 4.5b (Figure 4.6 a). The low-angle grain boundary generated distinctive atomic arrangements along the

boundary depending on its misorientation angle. When the misorientation angle was low (less than 10-15°), the distortion at the boundary was entirely accommodated by the inclusion of dislocations into the boundary. In the case of pure tilt boundary, the dislocation was mostly edge-type which essentially generated extra half-plane of atoms. Edge component of dislocation was also confirmed by a Burgers circuit around a dislocation core consisting of low-angle grain boundary, as shown in Figure 4.6a. Burgers vector identified with yellow arrow was found to be $1/3\langle 11\bar{2}0 \rangle$, the normal direction to the dislocation line, indicating the edge-type dislocation.

High-angle grain boundaries having misorientation angles larger than 20° were also prevalently observed, as shown in the regions marked with white-dashed squares in Figure 4.5a. Many of these high-angle grain boundaries in the ZnO/graphene system also corresponded to the [0001]-tilt grain boundaries. Many of the high-angle grain boundaries exhibiting high misorientation angle (greater than 15°) mostly formed the special boundary, termed coincidence site lattice (CSL) boundary, to reduce their grain boundary energy. The CSL boundary shows various atomic configurations depending on its misorientation angle and boundary plane.³⁶ In ZnO/graphene system which was developed in the present work, $\Sigma 7$ CSL boundaries were usually observed. As shown in Figure 4.5c, such flat and symmetric grain boundary exhibited the misorientation angle of 22.6°, close that of $\Sigma 7$ CSL boundary (21.79°), and the $\{12\bar{3}0\}$ boundary plane³⁶.

The atomic arrangements of the $\Sigma 7$ CSL boundary was examined in

detail using a magnified HR-TEM image in Figure 4.6b. The boundary exhibited ordered structure which consisted of periodic structural units as clarified by quadrilaterals along the boundary. The periodicity of the structural unit is well represented in the figure. Bright spots in quadrilaterals were arranged in every 3 atomic spacings, which is consistent of the previous report regarding typical $\Sigma 7$ boundary having $\{12\bar{3}0\}$ boundary plane. This boundary features smallest periodicity among the possible tilt grain boundaries in the hexagonal system³⁶.

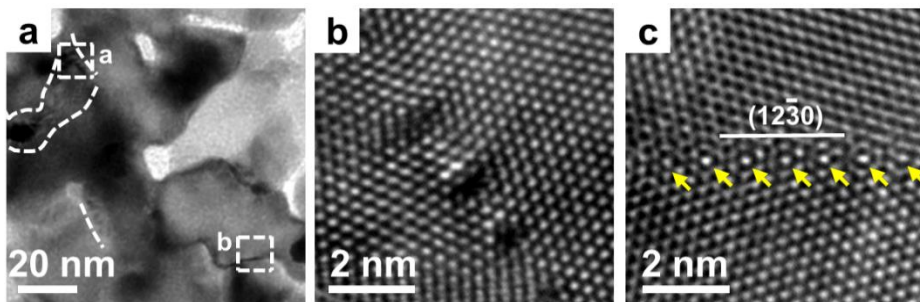


Figure 4.5. Grain boundary formation during ZnO nanomaterials growth.
(a) BF image obtained in the region where ZnO grains had substantially coalesced. The dashed lines denote low-angle grain boundaries. HR-TEM images were taken at each marked region, clearly showing the atomic configurations of grain boundaries. (b) Low-angle grain boundary containing an array of edge-type dislocation cores. The boundary has a rotation angle of 7.1°. (c) High-angle grain boundary with a rotation angle of 22.6° and the $\{12\bar{3}0\}$ boundary plane. Dislocation-like structural units periodically shown along the boundary are denoted by arrows.³¹

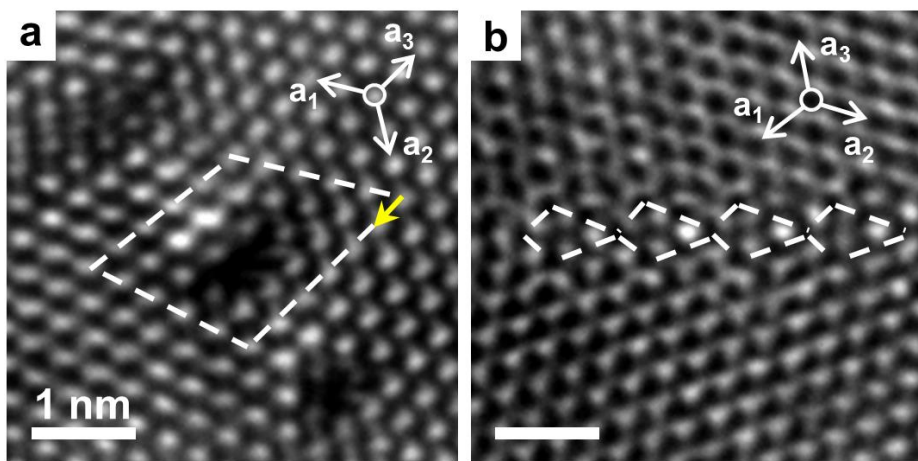


Figure 4.6. Distortion of atomic arrangements nearby various defects. (a) Enlarged HR-TEM image of Figure 4.5b, focusing on the dislocation core at the low-angle grain boundary. The Burgers circuit is drawn around the dislocation core at the grain boundary, which reveals a Burgers vector of $b = 1/3\langle 11\bar{2}0 \rangle$. (b) Enlarged HR-TEM image of Figure 4.5c, focusing on the grain boundary. The quadrilaterals representing structural units are marked along the high-angle grain boundary plane of $\{12\bar{3}0\}$. The Burgers circuit is also drawn around the dislocation core, which reveals a Burgers vector of $b = 1/3\langle 11\bar{2}0 \rangle$. The directions a_1 , a_2 , and a_3 in the figures are hexagonal lattice vectors, and the yellow arrows denote the Burgers vectors of the defects.³¹

4.5 Summary and outlook

In summary, the “direct growth and observation” technique with a graphene template was newly demonstrated to investigate the growth mechanism of ZnO nanomaterials. Graphene layers were used as a crystalline substrate exhibiting electron beam transparency, thereby enabling direct growth of ZnO nanomaterials on the free-standing graphene as well as atomic-resolution analysis using TEM. Various phenomena associated with the initial stage of heteroepitaxial growth could be clearly observed with high-sensitivity and resolution using this method. This includes the structural change of ZnO nuclei from cubic to hexagonal phase at the nucleation process and the formation of grain boundaries such as $\Sigma 7$ CSL boundary. The observation of rocksalt ZnO phase has great significance for providing unconventional p-type ZnO since rocksalt ZnO phase is known to be compatible for p-type doping, as opposed to typical hexagonal ZnO phase showing difficulty in p-type doping. The controlled growth of such rocksalt ZnO phase, which was only synthesized artificially at extremely high temperature and pressure, may open up new possibility of fabricating ZnO p-n junction and its application to electronic and optoelectronic devices. The dominant formation of $\Sigma 7$ CSL boundary has also important implications in anticipating electrical properties of ZnO grown on graphene because electrical properties are strongly correlated with double Schottky barrier at the grain boundary which is determined by the atomic configurations or the dopant segregation at the boundary. The success of clear imaging and analysis of nanomaterials on graphene using a new technique

promises insights for investigating extremely small nanostructures and their heteroepitaxial growth behavior beyond our current knowledge. Moreover, the experimental scheme demonstrated in this work can be readily exploited to study various phenomena in the heteroepitaxial growth of diverse materials on the crystalline 2-D materials.

CHAPTER 5

Growth mechanism of GaAs/graphene/InAs double heterostructures

In this chapter, the growth mechanism of GaAs/SLG/InAs double heterostructures is examined. Particularly, it is ascertained whether the nanomaterials already grown on the surface of graphene can influence on the subsequent nucleation and growth behavior of nanomaterials grown on the other side of graphene. In order to perform atomic-resolution imaging of nanomaterials without conventional TEM sample preparation processes, the improved “direct growth and observation” method using a graphene and a prefabricated SiNx membrane TEM grid is newly introduced. Firstly, its feasibility and reliability for the crystal growth as well as TEM measurements are confirmed. Then, using this method, the growth behavior of GaAs nanomaterials on SLG /InAs nanorods heterostructures is thoroughly discussed.

5.1 Introduction

Material systems exhibit dramatically different physical properties depending on their dimensionality, such as 0-D, 1-D, 2-D, and 3-D crystal structure. Atomically thin layered crystals, so called ‘2-D layered materials’, isolated by mechanical exfoliation method have exhibited new physical properties and provided novel applications.^{17,18} Graphene is a firstly demonstrated 2-D material which shows remarkable electron transport properties including high electron mobility at room temperature, with reported values in excess of $15,000 \text{ cm}^2/\text{V}\cdot\text{s}$.³⁸ Moreover, hybrid structures of these 2-D layered materials with semiconductor thin films and nanostructures offer additional functionalities, such as flexibility and transferability, thereby greatly extending their applicability to the future electronic and optoelectronic devices.^{9,11,12} Accordingly, many efforts have focused on nanomaterials growth using 2-D materials as substrates. In order to fabricate such nanomaterials with desired shapes and physical properties, the study on the growth mechanisms, such as nucleation, nuclei growth, and orientational relationship with substrate, should be priorly accompanied.

The growth of thin films and nanomaterials on 2-D layered materials is governed by a new mechanism called van der Waals epitaxy which was first suggested by Koma *et al.* in 1980s.²⁹ The van der Waals epitaxy features incommensurate epitaxy that enables coherent growth of materials without a direct chemical bond with a substrate having a large lattice mismatch due to an inert surface of 2-D materials without a dangling bond.²⁸ This is opposed to the

principle of conventional epitaxy based on a strong chemical bond between distinct atoms of growing material and a substrate. Therefore, the growth mechanism of nanomaterials on 2-D layered materials regarding the van der Waals epitaxy should be first investigated in detail.

One of the interesting aspects concerning the growth behavior of compound semiconductor on 2-D materials is whether the materials grown on the one side of atomically thin 2-D materials can influence on the nucleation and growth behavior on the other side. There were two different reports conflicting with each other in this context. Hong *et al.* suggested that the growth of InAs nanorods were not affected by the presence of InAs nanorods grown on the backside of SLG (Figure 5.1).³⁹ They showed identical van der Waals binding energy and van der Waals gap between InAs and SLG for the systems of InAs/SLG and InAs/SLG/InAs double heterostructures, indicating that InAs nanorods were grown on/underneath SLG independently. On the other hand, Kim *et al.* reported that GaAs thin films grown on SLG were influenced by the presence of underneath GaAs(001) substrate through SLG (Figure 5.2).⁴⁰ They showed that electron densities of both GaAs overlapped through SLG and, as a result, crystallographic orientation of GaAs grown on SLG mimicked that of GaAs(001) substrate. This suggests clear evidences for the interaction between GaAs placed on/underneath SLG.

In this work, GaAs/SLG/InAs double heterostructures were fabricated by catalyst-free MBE method to verify the role of graphene in the van der Waals epitaxy. InAs nanorods were grown first on the backside of SLG to study

whether GaAs nanomaterials grown on the front side of SLG can be influenced by the presence of InAs nanorods underneath SLG. TEM measurements revealed that nucleation sites of GaAs coincided with those of InAs nanorods. Additionally, the growth direction of GaAs can be flipped by the interaction with InAs nanorods underneath SLG. These results indicate that InAs nanorods can affect the nucleation and growth behavior of GaAs through atomically thin graphene.

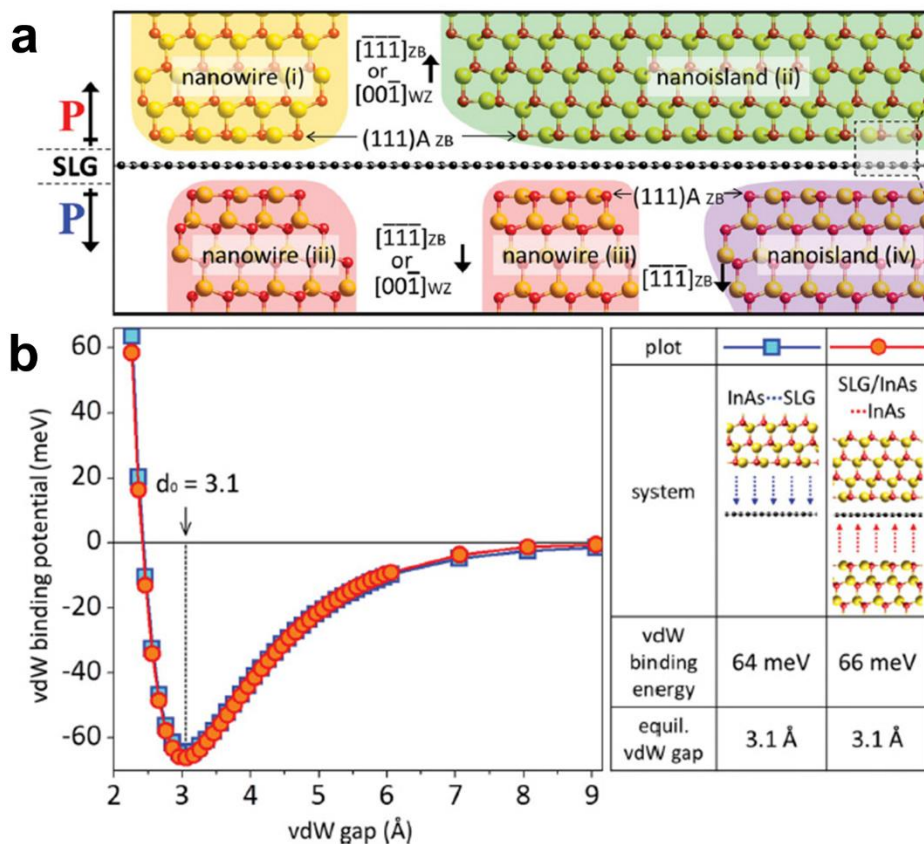


Figure 5.1. InAs/SLG/InAs double heterostructures. (a) Schematic illustration of InAs/SLG/InAs double heterostructures with polarity directions of InAs denoted in the figure. (b) Calculated van der Waals binding energy depending on the van der Waals gap between InAs and SLG for InAs/SLG and InAs/SLG/InAs double heterostructures, respectively.³⁹

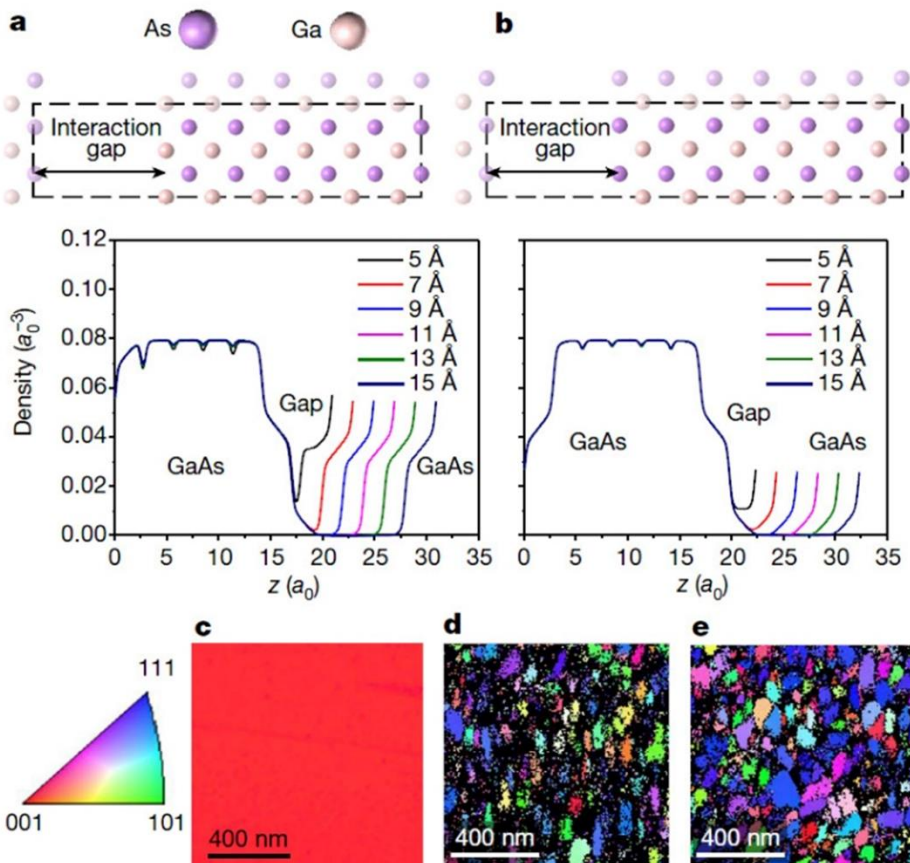


Figure 5.2. GaAs thin films grown on graphene-coated GaAs(001) substrate. (a,b) Density functional theory calculations of averaged electron density along directions identified by arrows between separated slabs of GaAs for (a) As–Ga interaction and (b) As–As interaction, respectively. (c–e) Electron backscattered diffraction orientational maps of GaAs thin films grown on (c) SLG, (d) bilayer graphene, and (e) tetralayer graphene-coated GaAs(001) substrate.⁴⁰

5.2 Direct growth and observation of nanomaterials using a graphene and prefabricated SiNx membrane TEM grid

5.2.1 Prefabricated SiNx membrane TEM grid

In order to observe GaAs and InAs nanomaterials without damages arising from conventional TEM sample preparation processes, the “direct growth and observation” technique was employed, as described in detail in Chapter 4.2. This method showed feasibility and reliability for both crystal growth and TEM measurements as shown in Chapter 4.3. However, the method left something to be desired in terms of crystal growth. Since commercial carbon layer-coated TEM grids, such as Quantifoil holey carbon grid, are very light, they may not contact well with a loading holder such as a graphite susceptor in an MOCVD reactor when reactant gases flow into a chamber with a sample loading holder rotated and heated during the growth. Such a bad contact between the loading holder and the sample would deteriorate temperature stability of the sample during the growth since the heat transfer from the loading holder is not consistent. This may induce slightly different growth conditions, and thus slight different growth behavior of nanomaterials at each cycle of crystal growth. Therefore, we need the other type of TEM grid that is not floating around easily on a sample loading holder during the crystal growth.

In this work, a prefabricated SiNx membrane TEM grid was newly fabricated and employed for “direct growth and observation” method instead of a commercial TEM grid. This new grid is based on a Si wafer widely used for

crystal growth for decades, which indicates a better suitability for the crystal growth in a growth chamber. The SiNx membrane TEM grid is basically similar to the previous methods using prefabricated thin membranes, such as Si_3N_4 and SiO_2 . The difference is that the prefabricated SiNx TEM grid employed in this work has an array of additional holes in the nitride membrane, which enables atomic-resolution imaging of nanomaterials through the holes using a graphene template, as described in Chapter 4.

Prefabricated SiNx membrane TEM grid is schematically represented in Figure 5.3. Figure 5.3a shows 5×5 array of SiNx membrane chips fabricated on the Si(100) wafer. A single SiNx membrane TEM grid has a shape of square and a length of 2.1 mm on a side to exactly fit the size of specimen mounting region in a TEM specimen holder. The SiNx membrane TEM grid consists of 200- μm -thick SiNx membranes on/underneath the Si wafer, and the nitride membrane is suspended on a square-shaped hole with a side length of $\sim 120 \mu\text{m}$ on the front side of Si wafer. A couple of micrometers-sized holes are also fabricated in the nitride membrane, as depicted in Figure 5.3b.

Figure 5.4a shows an OM image of homemade SiNx membrane chips which possesses 5×5 array of SiNx membrane TEM grids. This image is analogous to the schematics in Figure 5.3a. These grids are cut and separated into single SiNx membrane TEM grids as shown in Figure 5.4b. All of the SiNx membrane TEM grids had a 200- μm -thick SiNx membrane suspended over the hole of Si(100) wafer (Figure 5.4c). The side of a square-shaped hole is $\sim 120 \mu\text{m}$ in length on the front side of Si wafer. The nitride membrane also has an

array of circular holes with a diameter of 0.5–2 μm , as shown in TEM image of Figure 5.4d. The black regions in the image corresponds to 200- μm -thick SiNx membrane which exhibits low electron beam transparency. This single SiNx membrane TEM grid is used together with a graphene as an ideal template for the crystal growth and TEM measurements, which is analogous to a graphene/commercial TEM grid system given in Chapter 4.2. The detailed fabrication procedures of the prefabricated SiNx membrane TEM grid are described in Chapter 3.1.2.

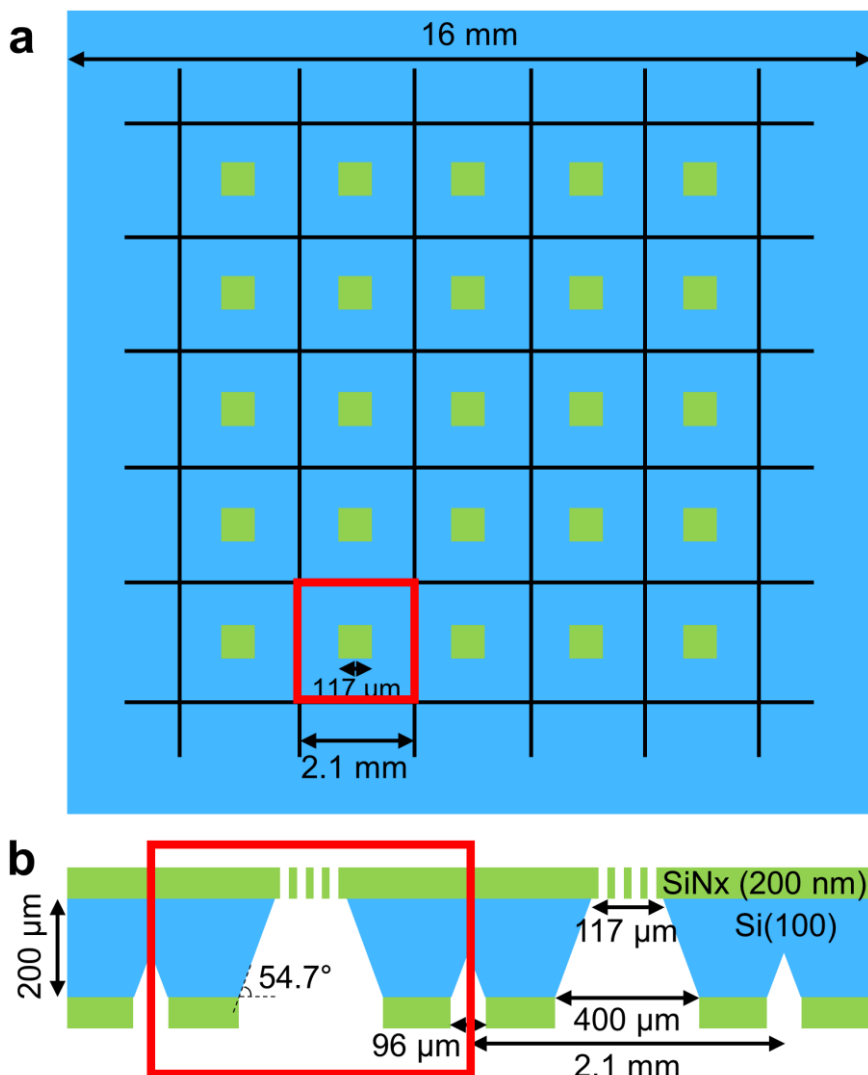


Figure 5.3. Schematic illustrations of a prefabricated SiNx membrane TEM grid. (a) Top view image of 5×5 array of SiNx membrane chips fabricated on a Si(100) wafer. (b) Cross-sectional image of SiNx membrane chips. Perforated SiNx membrane is clearly visible on the Si(100) wafer which will be used for atomic-resolution imaging in TEM. Red boxes in (a) and (b) indicate a region of single SiNx membrane TEM grid.

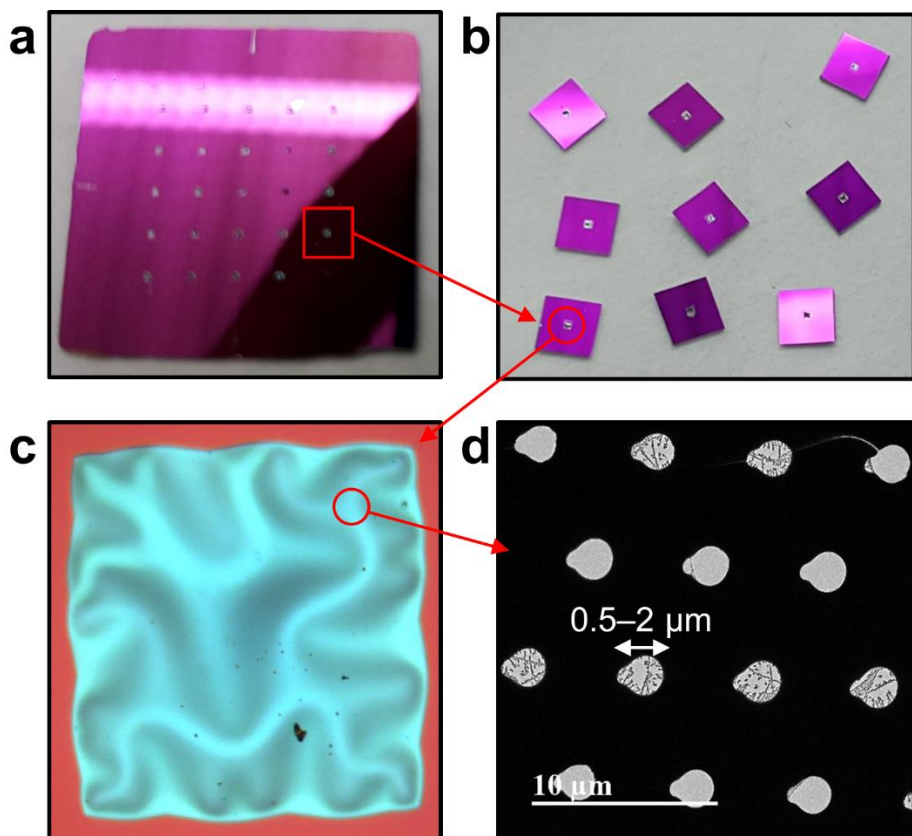


Figure 5.4. Homemade SiNx membrane TEM grid. (a) OM image of 5×5 array of prefabricated SiNx membrane chips. (b) Single SiNx membrane TEM grids. (c) SiNx membrane suspended over the square-shaped hole of a Si(100) wafer. (d) TEM image of an array of circular holes with a diameter of $0.5\text{--}2 \mu\text{m}$ in the SiNx membrane.

5.2.2 Direct growth and observation of GaAs and InAs nanomaterials

In order to achieve atomic-resolution and high sensitivity imaging of nanomaterials without background signal from the underlying thick membrane, graphene exhibiting excellent electron beam transparency and high mechanical strength is used as an ideal substrate for crystal growth and TEM measurements. The improved “direct growth and observation” method using a graphene and SiNx membrane TEM grid is schematically illustrated in Figure 5.5. The experimental scheme of this method is nearly same as that introduced in Chapter 4.2.

CVD graphene was grown on a Cu foil by CVD method and transferred onto a prefabricated SiNx TEM grid. Detailed growth and transfer procedures of graphene are explained step by step in Chapter 3.1.1 and Chapter 3.1.3, respectively. The graphene/SiNx membrane TEM grid template was then loaded in a cryogenically cooled ultra-high vacuum MBE chamber. In contrary to the growth of ZnO nanomaterials on graphene layers, O₂ plasma treatment was not performed since SLG is extremely vulnerable to plasma treatment. InAs nanorods were grown on the backside of SLG suspended over the perforated nitride membrane by catalyst-free MBE method for 30 s. Afterward, GaAs nanomaterials were grown on the front side of SLG placed on the nitride membrane for 30 s. The detailed growth procedures of GaAs and InAs nanomaterials are described in Chapter 3.2.2. After the growth, the template with GaAs and InAs grown on/underneath SLG was loaded in TEM without

conventional TEM sample preparation processes. TEM measurements including SAED and HR-TEM imaging were then performed on the GaAs and InAs nanomaterials grown on the both sides of SLG.

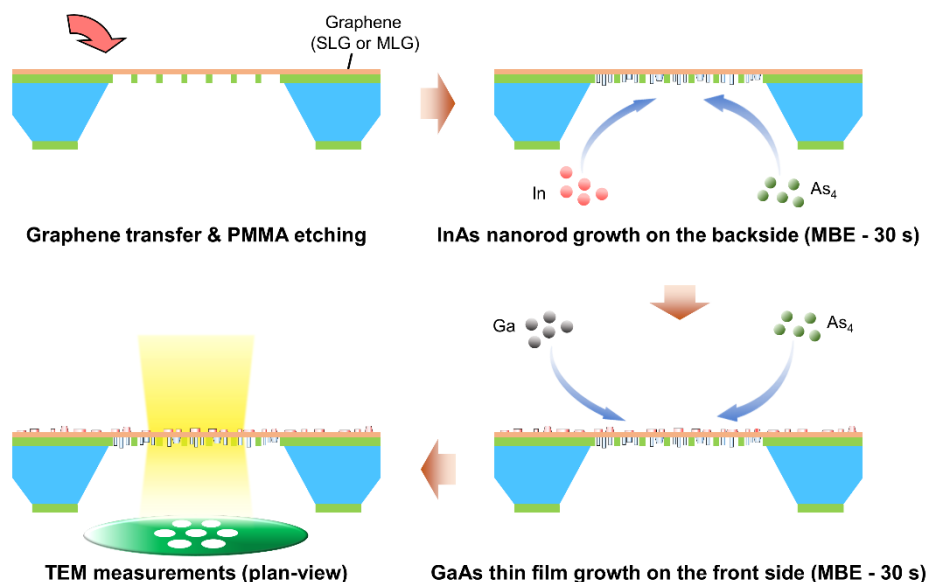


Figure 5.5. Direct growth and observation method using a graphene and SiNx membrane TEM grid. Graphene was transferred onto a prefabricated SiNx membrane TEM grid. InAs was grown first on the backside of graphene by catalyst-free MBE method. Afterward, GaAs was deposited on the front side of graphene. After the growth, TEM measurements were performed without conventional TEM sample preparation processes.

5.3 Feasibility of the improved method for crystal growth and TEM measurements

Feasibility of the graphene/SiNx membrane TEM grid system as a template for crystal growth and TEM measurements was verified. Thermal, mechanical, and chemical stabilities of the graphene/SiNx membrane TEM grid template at high growth temperature were thoroughly confirmed by SEM and TEM measurements. GaAs and InAs nanomaterials were grown on the graphene template for 30 s each using catalyst-free MBE method under the growth condition as mentioned in Chapter 3.2.2. Figure 5.6a displays a photograph of two graphene/SiNx membrane TEM grid templates loaded in a sample loading holder of MBE chamber. The template showed advantages over the graphene/commercial TEM grid template in terms of ease of sample loading on a holder, which would be beneficial for maintaining temperature stability of the sample during the growth. Figure 5.6b shows that both the graphene and nitride membrane suspended on the hole of Si wafer remained intact after the growth at high temperature, clearly indicating their robustness. Remarkable mechanical and thermal stability of graphene was also confirmed by SEM image in Figure 5.6c. This shows that graphene suspended over the micrometer-sized hole of nitride membrane still remained in a fairly good condition even with GaAs and InAs grown on it after the whole growth procedures. Therefore, it was clearly confirmed that the graphene/SiNx membrane TEM grid template can be exploited for the following “direct growth and observation” method without any problem.

The capability of acquiring clear atomic-resolution images of the graphene/SiNx membrane TEM grid template was further confirmed. Figure 5.7a shows HR-TEM image of GaAs and InAs nanomaterials grown on/underneath SLG acquired using aberration-corrected TEM equipped with an image corrector. The HR-image was taken in the region of free-standing SLG to avoid electron beam scattering from underlying thick and amorphous supporting layers. As already mentioned in Chapter 4.3, background signals caused by underlying graphene supporting layer was rarely detected due to its atomic-scale thickness and low atomic number, compared with conventional thick and amorphous supporting layers. In addition, such a growth of nanomaterials on the regions of free-standing graphene became possible because of high mechanical strength of graphene. Moreover, it was verified that GaAs and InAs nanomaterials grew on the graphene template in the same manner as they did on graphene lying on arbitrary substrates. This also ensures that the template can be exploited to investigate the general growth behavior of the GaAs and InAs nanomaterials on SLG.

The graphene, which was used as an ideal substrate as well as a supporting layer, enabled both crystal growth and TEM measurements without conventional TEM sample preparation processes. The SEM and TEM images showed that the free-standing region of the graphene remained intact after the growth process at high temperature. In addition, GaAs and InAs nanomaterials grown on the free-standing graphene stayed stable under various measurements. This suggests that the graphene/SiNx membrane TEM grid system is an ideal

template to investigate the nucleation and growth behavior of GaAs and InAs nanomaterials grown on a graphene substrate.

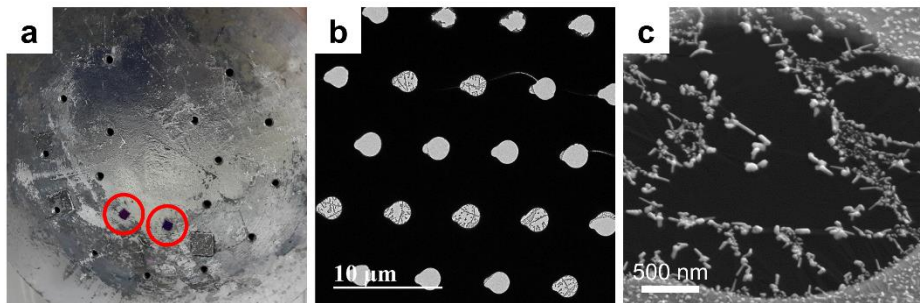


Figure 5.6. Feasibility of a graphene/SiNx membrane TEM grid template for nanomaterials growth and TEM measurements. (a) Photograph of the templates loaded in a sample loading holder of MBE chamber. The templates are identified by red circles. (b) TEM image of an array of circular holes in the nitride membrane after the growth of GaAs and InAs on/underneath SLG. This shows that the graphene/SiNx membrane maintained its structure after the growth at high temperatures. (c) SEM image of GaAs and InAs nanomaterials grown on/underneath SLG suspended over the perforated nitride membrane.

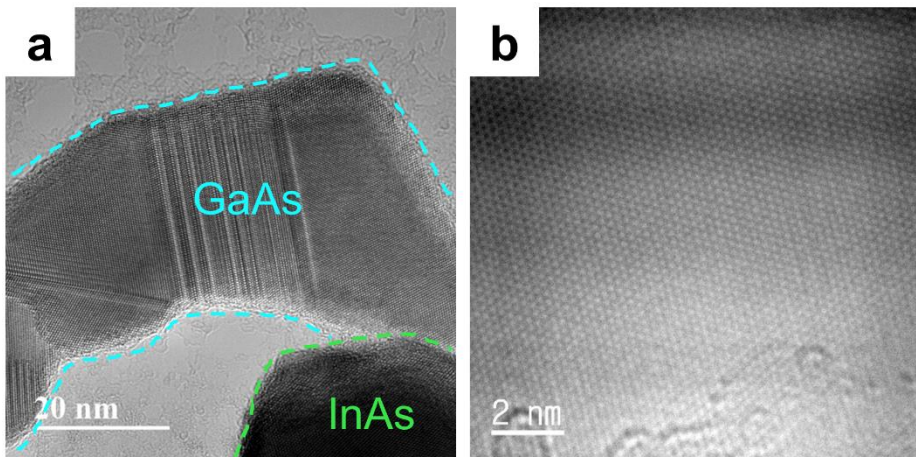


Figure 5.7. Atomic-resolution imaging performed over the suspended SLG.
(a) HR-TEM image of GaAs and InAs nanomaterials grown on/underneath SLG. (b) HR-TEM image of SLG.

5.4 Growth mechanism of GaAs/SLG/InAs double heterostructures

5.4.1 Control group: growth behavior of GaAs on SLG

The growth behavior of GaAs clusters on SLG was first examined as a reference case in order to unravel the growth mechanism of GaAs clusters on SLG/InAs nanorods heterostructures, in particular, to identify whether InAs nanorods influence on the nucleation and growth of GaAs nanomaterials through SLG. The improved “direct growth and observation” method using a graphene and SiNx membrane TEM grid was employed for the growth of GaAs nanomaterials and subsequent TEM measurements. GaAs nanomaterials were grown on SLG for a short time of 30 s by catalyst-free MBE method, and atomic-resolution imaging was performed on the region of suspended SLG using an aberration-corrected TEM operated at 80 kV.

GaAs nanomaterials grown on SLG exhibited various growth behavior, particularly, in terms of the growth direction. Figure 5.8 shows HR-TEM images of GaAs clusters grown on SLG and their corresponding FFT patterns. GaAs clusters mostly consisted of multiple grains having different crystallographic orientations at the initial growth stage as shown in Figure 5.8a–c. The grain boundaries and growth directions of GaAs grains were identified by analyzing FFT patterns obtained from individual grains in the HR-TEM images. The growth directions of the grains marked with asterisks in Figure 5.8a–c were specified as crystallographic zone axes in Figure 5.8d–f. A direction of [111]_{ZB}, a preferential growth direction of GaAs nanorods, was also

denoted as an arrow for each GaAs grain in Figure 5.8a–c for the sake of convenient explanation of the growth directions of GaAs clusters.

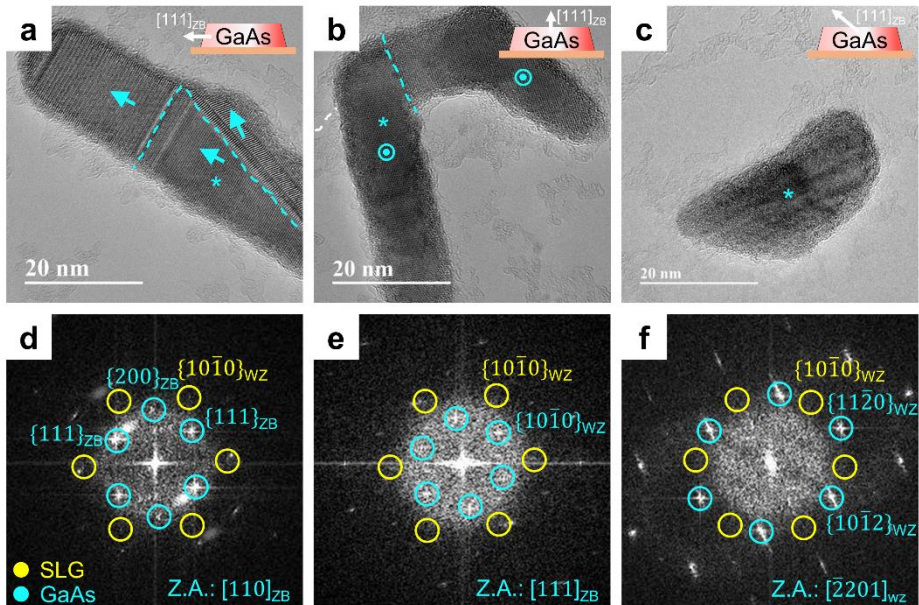


Figure 5.8. Various growth directions of GaAs clusters grown on SLG. (a–c) HR-TEM images showing GaAs clusters grown on SLG with a $[111]_{\text{ZB}}$ direction (a) pointing laterally, (b) pointing vertically, and (c) tilted with respect to the surface of SLG, respectively. Schematics in the insets represent the directions of GaAs $[111]_{\text{ZB}}$. Each grain in the cluster is identified by dashed lines. The $[111]_{\text{ZB}}$ direction of each grain is identified by an arrow. (d–f) Corresponding FFT patterns obtained from GaAs grains marked with asterisks in (a–c), respectively. The FFT peaks from SLG and GaAs were identified with yellow and cyan circles, respectively. The growth directions of GaAs grains, termed as crystallographic zone axis (Z.A.), are indicated in the figures.

In order to examine the preferential growth direction of GaAs on SLG, a considerable number of HR-TEM images of GaAs clusters were acquired and the growth directions for all of the grains were investigated by analyzing FFT patterns. Figure 5.9 displays statistics for the growth direction of GaAs clusters grown on SLG which were obtained by aforementioned procedures. GaAs grains were classified into three different groups by where their $[111]_{\text{ZB}}$ directions are pointing towards with respect to the surface of SLG; the $[111]_{\text{ZB}}$ direction formed horizontally, vertically, and in a tilted direction on the surface of SLG. These three orientations of $[111]_{\text{ZB}}$ each correspond to those in Figure 5.8a–c. The number of GaAs grains that belonged to each three groups were represented as a pie chart in Figure 5.9a. This chart clearly revealed that most of GaAs grains were grown with a $[111]_{\text{ZB}}$ direction formed horizontally on the surface of SLG.

The growth direction of GaAs having horizontal $[111]_{\text{ZB}}$ direction was further investigated. Figure 5.9b displays a pie chart showing the percentages of GaAs grains that had each growth direction represented in the legend. In this statistic, GaAs grains, which were grown with a $[111]_{\text{ZB}}$ direction pointing horizontally, were only considered. The pie chart also reveals that most of GaAs grains were grown along $[1\bar{1}0]_{\text{ZB}}$ direction. The portion of GaAs grains that belonged to group ‘others’ was excluded for the analysis since their growth directions were not explicitly identified. This might be because some of the grains were still incompletely crystallized at the initial stage of growth, which made it difficult to index their crystallographic orientations. To conclude, it was

clearly verified that GaAs clusters were preferentially grown along $[1\bar{1}0]_{ZB}$ direction with $[111]_{ZB}$ formed horizontally on the surface of SLG, as shown in Figure 5.8a and d. This result will be used as a reference for the analysis of growth behavior of GaAs/SLG/InAs double heterostructures in the following section.

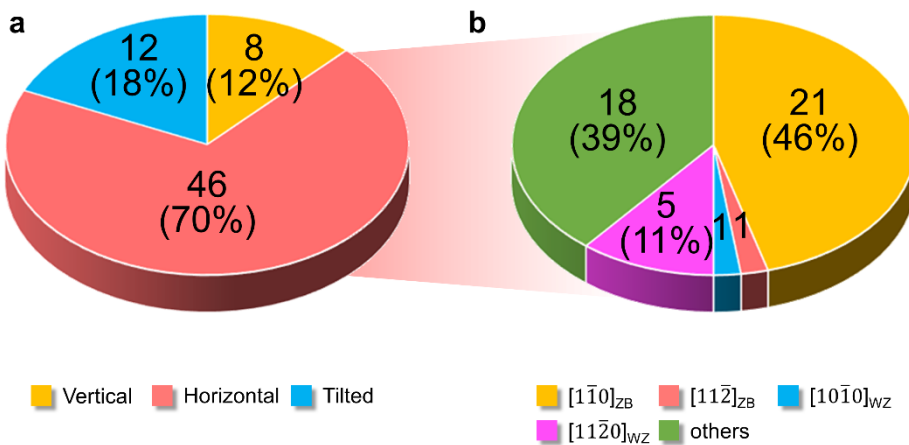


Figure 5.9. Statistics for the growth direction of GaAs clusters on SLG. (a) The number of GaAs grains classified by their $[111]_{ZB}$ directions with respect to the surface of graphene. Horizontal, vertical, and tilted directions correspond to $[111]_{ZB}$ directions of GaAs grains formed as shown in Figure 5.8a–c, respectively. (b) The number of GaAs grains having a horizontal $[111]_{ZB}$ direction, which is further classified by their growth directions as shown in the legend. The green portion named ‘others’ in the legend indicates GaAs grains with a horizontal $[111]_{ZB}$ direction, but the growth direction was not fully identified.

5.4.2 Experimental group: growth behavior of GaAs on SLG/InAs

The growth behavior of GaAs clusters on SLG with InAs nanorods grown on the backside was investigated by comparing with that on bare SLG studied previously in Chapter 5.4.1. By analyzing the growth behavior of GaAs clusters on SLG/InAs heterostructures, it will be ascertained whether InAs nanorods on the backside of SLG can influence on the nucleation and growth of GaAs nanomaterials on the other side. The same approach using “direct growth and observation” method as in Chapter 5.4.1 was employed for the growth of InAs and GaAs nanomaterials and following TEM measurements. InAs nanorods were grown first on the backside of SLG, and GaAs nanomaterials were grown on the other side both for a short time of 30 s by catalyst-free MBE method. Atomic-resolution imaging using an aberration-corrected TEM operated at 80 kV was performed on the region of suspended SLG.

GaAs nanomaterials grown on SLG/InAs heterostructures also exhibited various growth directions. Figure 5.10 shows HR-TEM images of GaAs clusters grown on SLG/InAs nanorods and their corresponding FFT patterns. The grain boundaries and growth directions of GaAs grains having different crystallographic orientations were identified by analyzing FFT patterns obtained from individual grains in Figure 5.10. The growth directions of the grains marked with asterisks in Figure 5.10a and b were specified as crystallographic zone axes in Figure 5.10d and e. Directions of GaAs $[111]_{\text{ZB}}$ and InAs $[0001]_{\text{wz}}$, a preferential growth direction of the nanorods, were also

identified by arrows for each GaAs and InAs grain in Figure 5.10a–c for the sake of convenient explanation of the growth directions of GaAs clusters and InAs nanorods.

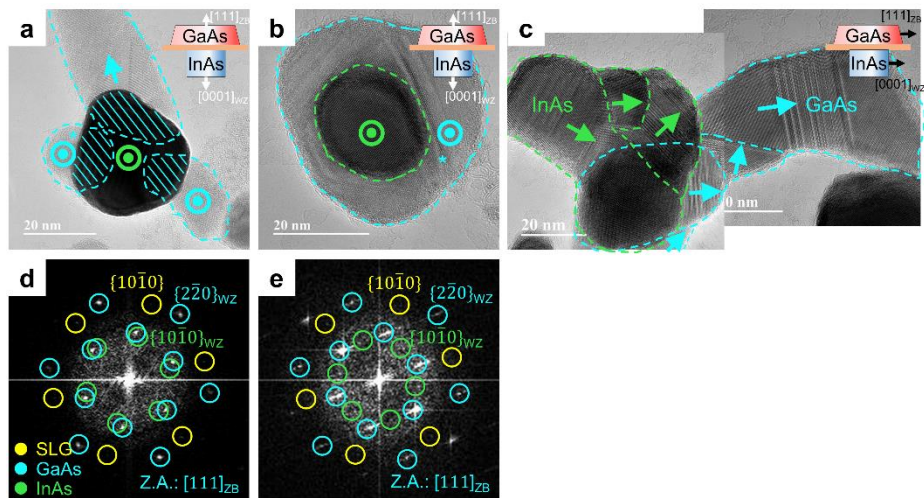


Figure 5.10. Various growth directions of GaAs clusters grown on SLG/InAs nanorods. (a–c) HR-TEM images showing GaAs clusters grown on SLG/InAs nanorods with both GaAs [111]_{ZB} and InAs [0001]_{WZ} directions pointing (a–b) vertically and (c) laterally with respect to the surface of SLG, respectively. Schematics in the insets represent the directions of GaAs [111]_{ZB} and InAs [0001]_{WZ}. The grains of GaAs and InAs in the clusters are identified by cyan and green dashed lines, respectively. The [111]_{ZB} direction of each grain is identified by an arrow. The dashed regions in (a) depict overlap areas of GaAs on SLG and InAs underneath SLG. (d–e) Corresponding FFT patterns obtained from GaAs grains marked with asterisks in (a–b), respectively. The FFT peaks from SLG, GaAs and InAs were identified with yellow, cyan, and green circles, respectively. The growth directions of GaAs grains, termed as crystallographic zone axis (Z.A.), are indicated in the figures.

Preferential growth direction of GaAs on SLG/InAs heterostructures was also examined by analyzing FFT patterns obtained from a substantial number of HR-TEM images of GaAs clusters and InAs nanorods. Both GaAs grains and InAs nanorods were classified into three different groups by where GaAs [111]_{ZB} and InAs [0001]_{wz} directions are pointing towards with respect to the surface of SLG in the same manner as in Chapter 5.4.1. From now on, InAs nanorods with vertical, horizontal, and tilted [0001]_{wz} directions are referred to as InAs_{vertical}, InAs_{horizontal}, and InAs_{tilted}, respectively, for the sake of convenient explanation.

Figure 5.11 displays statistics for the growth direction of GaAs grains grown on SLG/InAs_{vertical}. The number of GaAs grains that belonged to each three groups were represented as pie charts in Figure 5.11a. The classification of GaAs grains with respect to the directions of [111]_{ZB} was conducted depending on the overlap areas of GaAs clusters on SLG and InAs nanorods underneath SLG, as illustrated by dashed regions in Figure 5.10a. The GaAs clusters that overlapped with InAs nanorods were only considered for the left pie chart, termed as $A_{overlap} > 0\%$, and the clusters that had overlap area over half their own size were only considered for the right pie chart, termed as $A_{overlap} > 50\%$, in Figure 5.11a. Interestingly, these charts clearly revealed that most of GaAs clusters were grown along [111]_{ZB} direction on SLG/InAs_{vertical}, indicating a growth direction flip compared with GaAs clusters grown along [1̄10]_{ZB} on SLG. In addition, the percentage of GaAs grown along [111]_{ZB} direction further increased up to 60% when the overlap area exceeded half the

size of each GaAs grains.

The growth direction of GaAs having horizontal $[111]_{\text{ZB}}$ direction was also investigated. Figure 5.11b displays pies chart showing the distribution of the growth directions among the GaAs grains having horizontal $[111]_{\text{ZB}}$ direction. The classification was also performed depending on the overlap area of GaAs clusters and InAs nanorods. These pie charts also reveals that most of GaAs grains having horizontal $[111]_{\text{ZB}}$ were grown along $[1\bar{1}0]_{\text{ZB}}$ direction, excluding the portion of GaAs grains that belonged to group ‘ $[0002]_{\text{wz}}/[111]_{\text{ZB}}$ along the surface’ of which the growth directions were not explicitly identified.

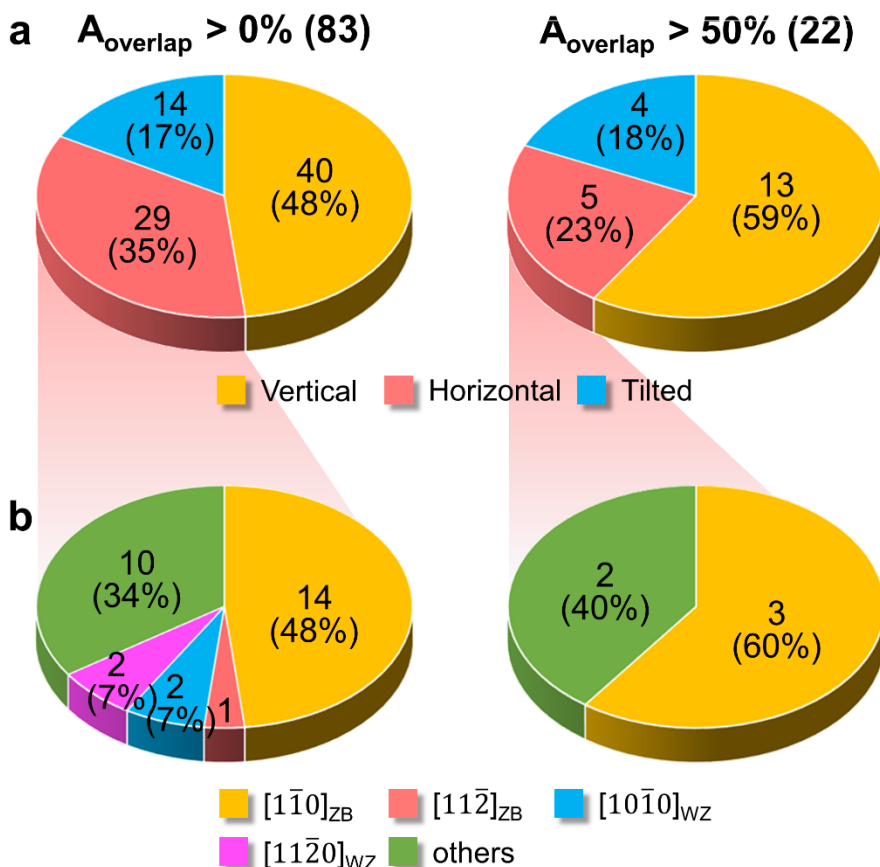


Figure 5.11. Statistics for the growth direction of GaAs clusters on SLG/InAs_{vertical} nanorods. (a) The number of GaAs grains classified by their $[111]_{\text{ZB}}$ directions with respect to the surface of graphene depending on the overlap area of GaAs and InAs (A_{overlap}). Horizontal, vertical, and tilted directions correspond to $[111]_{\text{ZB}}$ directions of GaAs grains formed as shown in Figure 5.8a–c. (b) The number of GaAs grains classified by their growth directions as represented in the legend, depending on the overlap area. GaAs grains having a horizontal $[111]_{\text{ZB}}$ direction were only considered. The green portion named ‘others’ in the legend indicates GaAs grains with a horizontal $[111]_{\text{ZB}}$ direction, but the growth direction was not fully identified. The numbers in the parentheses at the top represent the total number of GaAs grains observed.

The growth behavior of GaAs clusters on SLG/InAs_{horizontal} and SLG/InAs_{tilted} heterostructures was also investigated. Figure 5.12 displays statistics for the growth direction of GaAs grains grown on SLG/InAs_{vertical}. The classification of GaAs grains by the directions of [111]_{ZB} was conducted depending on the overlap areas of GaAs clusters and InAs nanorods in the same manner as for Figure 5.11. These pie charts show that 70–80% of GaAs clusters were grown along [1̄10]_{ZB} direction with a [111]_{ZB} direction formed horizontally on SLG/InAs_{horizontal}. The percentages of the grains having horizontal [111]_{ZB} direction and [1̄10]_{ZB} growth direction are nearly identical to those for the GaAs grains grown on bare SLG described in Chapter 5.4.1 as a reference case, suggesting that the growth behavior of GaAs on SLG/InAs_{horizontal} heterostructures almost resembles that on bare SLG. This indicates that the growth direction flip did not occur for the growth of GaAs on SLG/InAs_{horizontal}.

Figure 5.13 displays statistics for the growth direction of GaAs grains grown on SLG/InAs_{tilted}. The classification of GaAs grains by the directions of [111]_{ZB} was conducted depending on the overlap areas of GaAs clusters and InAs nanorods in the same manner as for Figure 5.11. These pie charts revealed an increased portion of GaAs grains having vertical [111]_{ZB} direction, which is analogous to the growth of GaAs on SLG/InAs_{vertical} in Figure 5.11. This might suggests that the growth direction of GaAs also changes from [1̄10]_{ZB} to [111]_{ZB} on the surface of SLG/InAs_{tilted}. However, it is hard to trust these statistics regarding the growth direction of GaAs on SLG/InAs_{tilted} since the

number of GaAs grains observed were not sufficient enough to extract a reliable conclusion in this case.

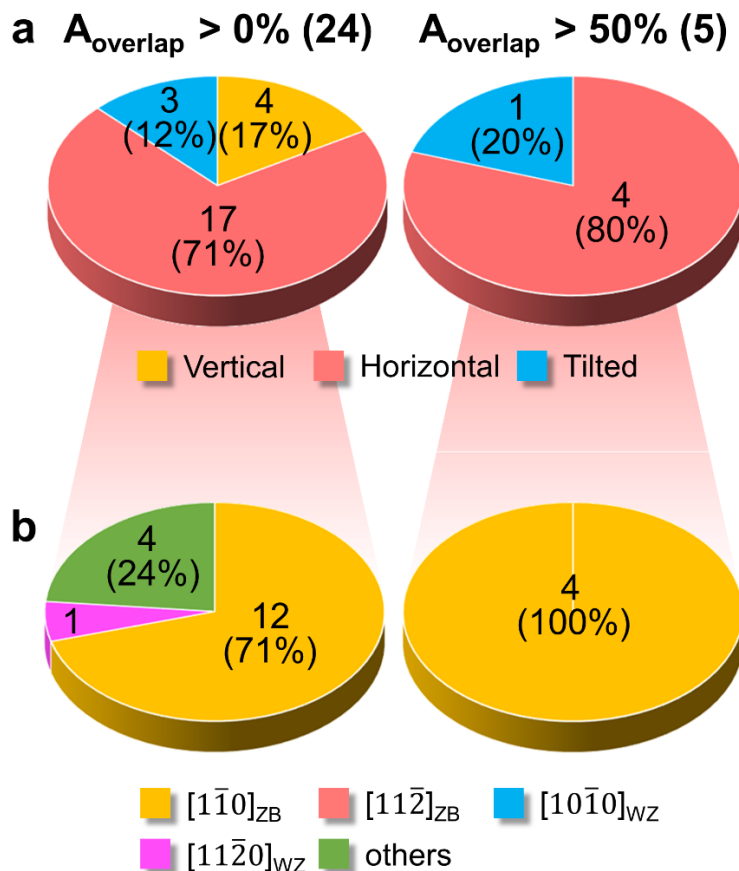


Figure 5.12. Statistics for the growth direction of GaAs clusters on SLG/InAs_{horizontal}. (a) The number of GaAs grains classified by their [111]_{ZB} directions with respect to the surface of graphene depending on the overlap area of GaAs and InAs with horizontal [0001]_{WZ} direction. Horizontal, vertical, and tilted directions correspond to [111]_{ZB} directions of GaAs grains formed as shown in Figure 5.8a–c. (b) The number of GaAs grains classified by their growth directions as represented in the legend, depending on the overlap area. GaAs grains having a horizontal [111]_{ZB} direction were only considered. The green portion named ‘others’ in the legend indicates GaAs grains with a horizontal [111]_{ZB} direction, but the growth direction was not fully identified. The numbers in the parentheses at the top represent the total number of GaAs grains observed.

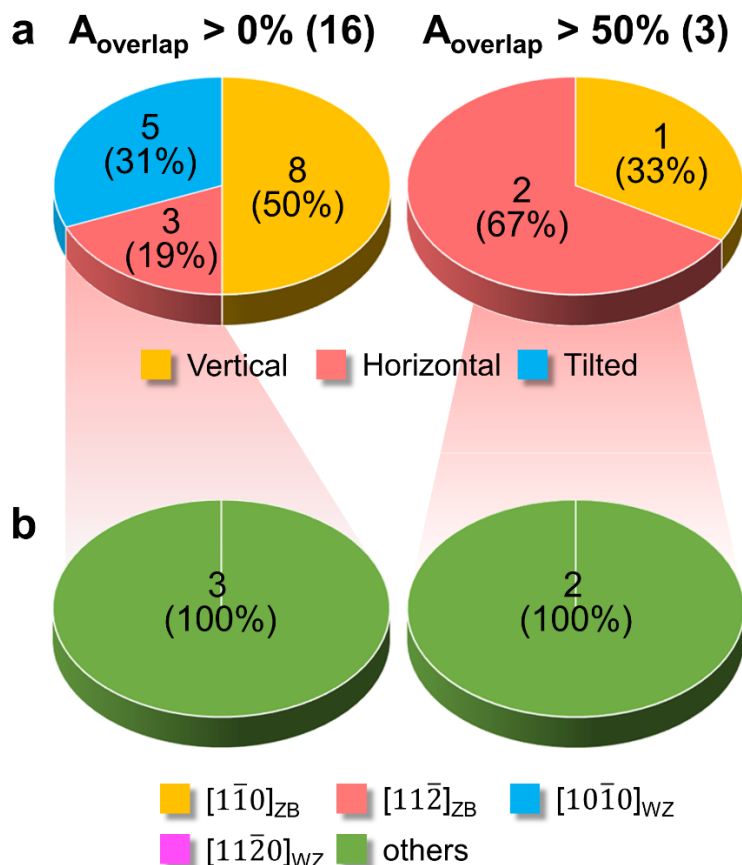


Figure 5.13. Statistics for the growth direction of GaAs clusters on SLG/InAs_{tilted}. (a) The number of GaAs grains classified by their [111]_{ZB} directions with respect to the surface of graphene depending on the overlap area of GaAs and InAs with tilted [0001]_{WZ} direction. Horizontal, vertical, and tilted directions correspond to [111]_{ZB} directions of GaAs grains formed as shown in Figure 5.8a–c. (b) The number of GaAs grains classified by their growth directions as represented in the legend, depending on the overlap area. GaAs grains having a horizontal [111]_{ZB} direction were only considered. The green portion named ‘others’ in the legend indicates GaAs grains with a horizontal [111]_{ZB} direction, but the growth direction was not fully identified. The numbers in the parentheses at the top represent the total number of GaAs grains observed.

5.4.3 General growth mechanism of double heterostructures

GaAs clusters were grown on SLG in different ways depending on the presence of InAs nanorods as well as their growth directions underneath SLG. The growth behavior of GaAs for the three different cases dealt with in the last two sections is schematically summarized in Figure 5.14. The growth of GaAs along $[1\bar{1}0]_{ZB}$ direction with $[111]_{ZB}$ direction formed laterally was favorable on bare SLG and SLG/InAs_{horizontal} (Figure 5.14a and c), whereas the growth of GaAs along $[111]_{ZB}$ direction was dominant on SLG/InAs_{vertical} (Figure 5.14b). The comparison between Figure 5.14a and c reveals that GaAs was grown on SLG/InAs_{horizontal} independently, irrespective of the presence of underlying InAs nanorods. Such an independent growth of GaAs can be evidenced by the statistics in Figures 5.9 and 5.12, which shows nearly same percentages of GaAs grains having $[1\bar{1}0]_{ZB}$ growth direction as well as $[111]_{ZB}$ lateral direction for both GaAs/SLG and GaAs/SLG/InAs_{horizontal}. On the other hand, the nucleation and growth of GaAs clusters seem to be affected by the presence of underlying InAs_{vertical}, in particular, by the growth direction of InAs nanorods. GaAs $[111]_{ZB}$ and InAs $[0001]_{WZ}$ are crystallographically identical except for their stacking sequences of hexagonal closed-packed atomic layers. Thus, it might be possible for GaAs to mimic the growth direction of underlying InAs nanorods and change the growth direction into that of InAs nanorods. Such a growth direction flip can be evidenced by an increase in the portion of $[111]_{ZB}$ -grown GaAs grains as the overlap area of GaAs clusters and InAs nanorods increases. The increase in the overlap area indicates that GaAs clusters are

much more influenced by the InAs nanorods underneath SLG, thereby enabling the growth direction flip as shown in Figure 5.14b.

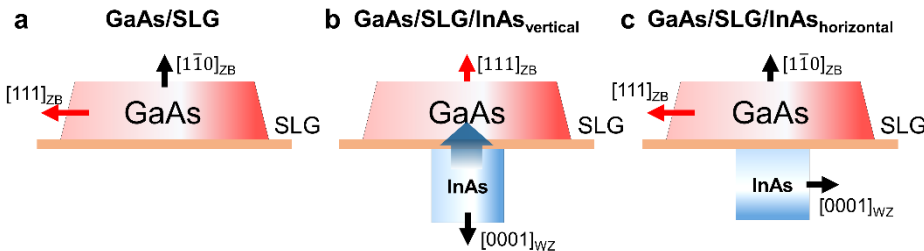


Figure 5.14. Growth direction flip of GaAs clusters. (a) GaAs clusters grown on SLG. (b) GaAs clusters grown on SLG/InAs with vertical $[0001]_{WZ}$ direction. (c) GaAs clusters grown on SLG/InAs with horizontal $[0001]_{WZ}$ direction.

The general growth mechanism of GaAs/SLG/InAs double heterostructures is schematically illustrated step by step in Figure 5.15. Firstly, InAs nanorods were grown on the backside of SLG. The preferential growth direction of InAs nanorods was $[0001]_{WZ}$, as marked with vertical arrows in the figure. The nanorods grown along the other direction still existed, as marked with lateral and slanted arrows in the figure, which were referred to as InAs_{horizontal} and InAs_{tilted} in Chapter 5.4.2. GaAs clusters were then grown on the front side of SLG. They preferentially nucleated at the sites nearby underlying InAs nanorods and grew along $[1\bar{1}0]_{ZB}$ and $[111]_{ZB}$ for GaAs/SLG/InAs_{horizontal} and GaAs/SLG/InAs_{vertical}, respectively. The growth of

GaAs on SLG/InAs_{horizontal} was not affected by the presence of InAs nanorods underneath SLG, thus showing the same growth direction as that of GaAs on bare SLG. In contrast, the growth of GaAs on SLG/InAs_{vertical} was influenced by the underlying InAs nanorods, in particular [0001]_{wz}-grown InAs nanorods, which results in the growth direction flip of GaAs clusters.

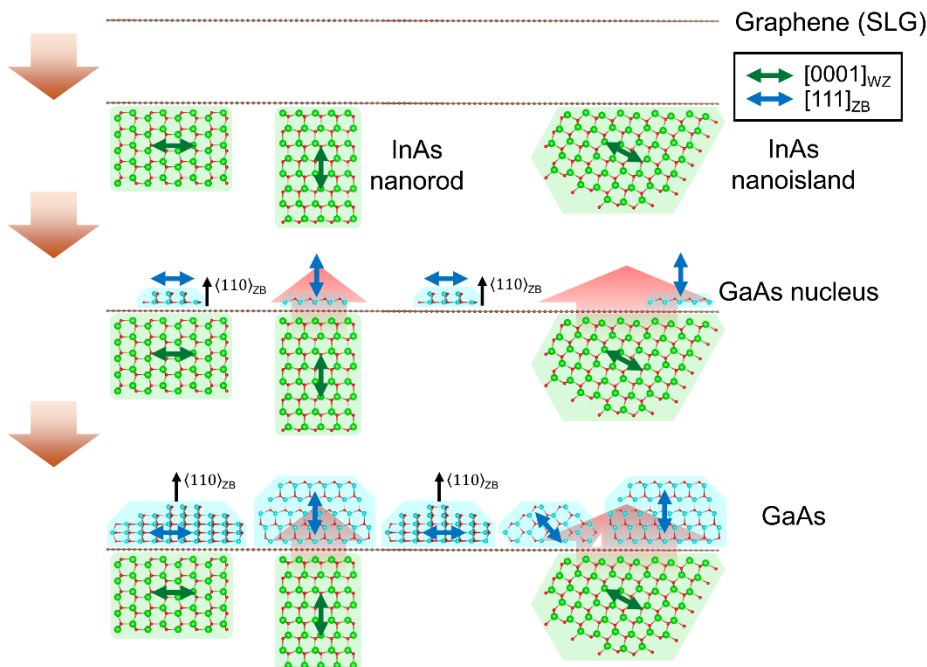


Figure 5.15. Schematic diagrams showing growth mechanism of GaAs/SLG/InAs double heterostructures. GaAs and InAs nanostructures are represented by blue and green polygons, respectively, with their atomic configurations observed along $[1\bar{1}\bar{2}0]_{\text{wz}}/[1\bar{1}0]_{\text{ZB}}$ directions. The directions of GaAs $[111]_{\text{ZB}}$ and InAs $[0001]_{\text{wz}}$ are identified by blue and green arrows, respectively.

5.5 Summary and outlook

In summary, the improved “direct growth and observation” technique using a graphene and a prefabricated SiNx membrane TEM grid was newly demonstrated to investigate the growth mechanism of GaAs/SLG/InAs double heterostructures. In particular, the possibility that two nanomaterials on/underneath SLG are interacted during the growth is addressed. The improved technique enabled the GaAs and InAs growth as well as atomic-resolution imaging on the free-standing SLG. The growth direction flip of GaAs clusters grown on SLG/InAs_{vertical} was observed to mimic the growth direction of InAs nanorods, whereas the growth of GaAs on SLG/InAs_{horizontal} was not influenced by the presence of underlying InAs nanorods. This suggests that the nucleation and growth of nanomaterials on SLG can be affected by not only the presence but also the growth direction of the other nanomaterials underneath SLG. Such an interesting growth behavior of double heterostructures can provide a great potential to stimulate a new field of research regarding the crystal growth as well as basic science based on atomically thin 2-D materials. Additionally, two different parts of nanostructures on/underneath 2-D materials can be exploited as independent functional devices. Therefore, the success of fabricating high-quality double heterostructures with desired physical properties will enhance versatility and multi-functionality of the future devices.

CHAPTER 6

Real-time characterization of the growth behavior of InAs nanorods using in situ RHEED transmission mode and TEM

This chapter discusses the initial growth mechanisms of InAs nanorods and GaAs($In_xGa_{1-x}As$)/InAs coaxial nanorods on Si(111) and graphene substrate. To monitor and analyze the growth behavior of nanorods in real time, RHEED, which is conventionally used only in reflection mode, is newly demonstrated in transmission mode during the growth. Firstly, the feasibility of RHEED transmission mode for structural analysis of nanomaterials is described by comparing with electron diffraction principles in TEM. Then, using the combined methods with RHEED transmission mode and TEM, the initial growth behavior of InAs nanorods showing a transition of local growth condition from In-rich to As-rich is explained. The strain relaxation process during epitaxial coating of coaxial nanorods is also discussed thereafter.

6.1 Introduction

A fundamental study on growth mechanisms has important implications for fabricating nanomaterials having desired physical properties. To achieve these high-quality nanomaterials for device applications, accurate structural information during the growth process is essential.^{12,13,41-45} The limitations of conventional *ex situ* characterization methods, such as atomic force microscopy and SEM, for studying the growth mechanism of nanomaterials are well recognized: the possibilities of structural or phase changes of a specimen caused by exposure to the atmosphere and the difficulties in the observation of intermediate states during the nucleation and growth processes.^{46,47} In recent years, researches exploiting *in situ* observation and characterization have enabled a direct observation of solid/liquid/gas-state reactions in real time. This allowed us to realize improved understanding beyond our current knowledge in diverse fields.⁴⁸⁻⁵² Accordingly, a search for a new characterization technique for assessing *in situ* structural information of nanomaterials during growth processes is also highly inspired.

RHEED in reflection mode, which utilizes high surface sensitivity of the glancing incident electron beam, is a powerful real-time monitoring technique for thin films growth because of its *in situ* compatibility with crystal growth in growth chambers.^{53,54} This method, however, was only able to be used for monitoring thin films growth. On the contrary, RHEED operated in transmission mode enables the *in situ* structural analysis of nanomaterials. The parallel electrons emitted from RHEED gun interact with growing

nanostructures, and they are scattered to generate diffraction patterns. This is basically same principle as electron diffraction in TEM, thereby enabling acquisition of structural information in real time during the growth of various nanostructures. Several studies have previously referred the evolution of spotty pattern arising from island formation or 2-D/3-D transition during the nanostructures growth using the RHEED transmission mode.⁵⁵⁻⁵⁸ However, Comprehensive study on the detailed growth mechanism of nanomaterials regarding their structural analysis using RHEED transmission mode have not been reported in spite of its great significance and potential.

In this work, the growth behavior of InAs nanorods and GaAs($\text{In}_x\text{Ga}_{1-x}\text{As}$)/InAs coaxial nanorods was investigated in real time using RHEED transmission mode together with TEM. The combination of both techniques eventually led to a better understanding on the growth mechanisms of nanostructures, which were not attainable using traditional *ex situ* analytical methods. This approach offered important new findings regarding the formation of pure zinc blende (ZB) and wurtzite (WZ) phases and structural change of InAs nanorods at the very initial stage of growth caused by the local transition of growth condition from In-rich to As-rich. Additionally, strain relaxation process via lattice constant accommodation was clearly revealed during epitaxial coating of GaAs shell layers.

6.2 RHEED transmission mode

The new technique of RHEED transmission mode is explained by comparing with electron diffraction in TEM. The principle of RHEED transmission mode is schematically illustrated in Figure 6.1. A collimated electron beam with high energy of 22.2 keV from RHEED gun passes through nanostructures, *i.e.*, nanorods, nanowires, and nanotubes that stand vertically on a substrate. The electron beam that has been interacted with the nanostructures produces diffraction patterns at a detector. These diffraction spots appear in the position where Bragg condition is satisfied, as in typical diffraction methods such as X-ray or electron diffraction in TEM. The difference from the electron diffraction in TEM is that RHEED patterns are acquired from larger area because of larger spot size of RHEED, which provides collective information of nanostructures as shown in Figure 6.1. Additionally, the RHEED diffraction patterns can be easily obtained from nanostructures without any modification of an MBE chamber as well as a special RHEED gun alignment. These characteristics of RHEED transmission mode allow us to obtain and analyze structural information of nanostructures in real time during the growth.

RHEED transmission mode offers a more complete range of information regarding the growth behavior of nanostructures when combined with TEM. This technique fundamentally shows similarity to electron diffraction in TEM, but offers complementary information to that obtained with TEM, thereby allowing us to exploit advantages of both RHEED transmission

mode and TEM simultaneously; real-time observation and structural analysis during the growth of nanostructures by RHEED transmission mode, and in-depth structural and chemical analyses with excellent spatial resolution by TEM. The combination of both techniques eventually leads to better understanding on the growth mechanisms of nanostructures, which are not attainable using traditional *ex situ* analytical methods. By using these methods together, we can investigate various growth mechanisms of any kind of nanostructures. This includes the very initial growth behavior of nanomaterials, the formation of epitaxial relationship with a substrate, structural change of nanostructures during the growth, and annealing effect of the specimen in a growth chamber, etc.

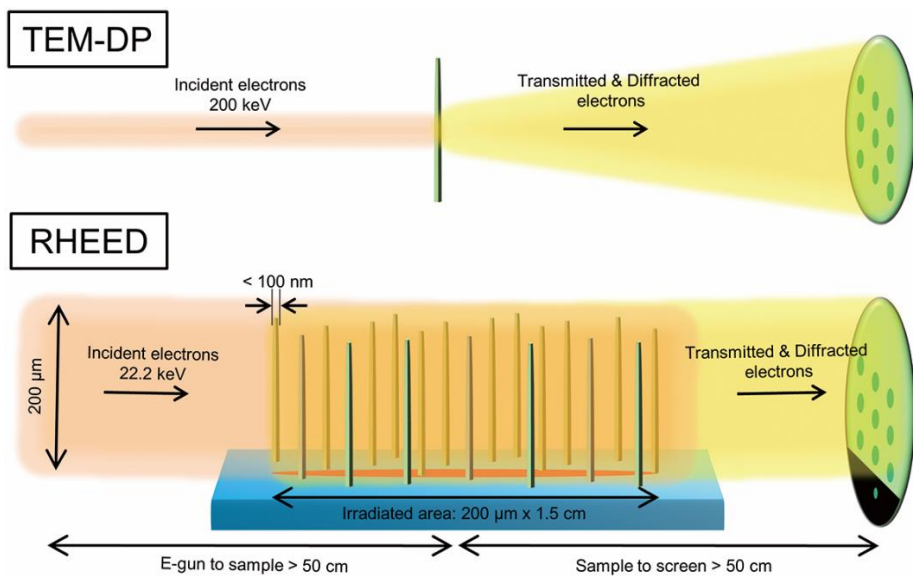


Figure 6.1. Schematic illustration of electron diffraction in TEM and RHEED. The electron diffraction in RHEED is compared with that in TEM. The RHEED electron beam has a larger spot size of 200 μm compared with a beam size in TEM. It glances off the surface of the substrate with an angle of *ca.* 0.8°. The size of the area irradiated by the electron beam is *ca.* 200 $\mu\text{m} \times$ 1.5 cm. The large spot size indicates that the RHEED diffraction pattern provides information concerning the nanostructures over a wide area of the specimen.

6.3 Feasibility of RHEED transmission mode for the real-time structural analysis of nanomaterials

As a model system for demonstrating the real-time characterization technique using RHEED transmission mode, InAs nanorods and GaAs($\text{In}_x\text{Ga}_{1-x}\text{As}$)/InAs coaxial nanorods were epitaxially grown on Si(111) substrate by catalyst-free MBE (Figure 6.2). The high-density of nanorods were extended up to 2–3 μm in length with a diameter of 40–60 nm and ~100 nm for InAs nanorods and coaxial nanorods, respectively. They showed excellent vertical alignment on the substrate, as shown in Figure 6.2a and c, even though they were grown under the exposure of electron beam emitted by a RHEED gun during the whole growth process. They were not bent or damaged by the irradiation of electron beam, indicating that electron beam hardly influences on the growth of nanorods. This might be due to low current density of large-area electron beam irradiation. In particular, the growth of InAs nanorods for coating of GaAs shell layers was carried out only for a short time of 2.5 min to prevent possible bending of the long GaAs/InAs coaxial nanorods because of the large lattice mismatch between GaAs and InAs and high stiffness of GaAs shell layer compared with InAs core nanorod (Figure 6.2d).

The material system based on InAs nanorods is especially good for demonstrating this real-time characterization technique since their diameter was small enough for electrons to transmit and their crystal orientations are well-aligned both in-plane and out-of-plane on the Si(111) substrate. Additionally, their various structural properties, including crystal phases and

stacking faults depending on the growth condition, size of nanorod, and controllable composition of ternary compounds,^{59–62} offer numerous aspects that can be studied using the *in situ* observation technique.

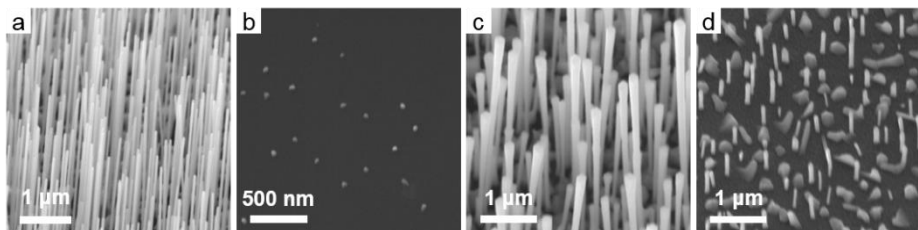


Figure 6.2. SEM images showing the surface morphology of nanorods grown on Si(111) substrate. (a) InAs nanorods. (b) InAs nanorods grown only for 30 s. (c) $\text{In}_x\text{Ga}_{1-x}\text{As}/\text{InAs}$ coaxial nanorods. (d) GaAs/InAs coaxial nanorods.

Feasibility of RHEED transmission mode for the real-time structural analysis of nanomaterials was verified by directly comparing with electron diffraction in TEM. HR-TEM images were taken at the edge of the InAs nanorods along three different orientations (Figure 6.3d–f), and corresponding FFT patterns were obtained from these HR-TEM images (Figure 6.3a–c, bottom). The InAs nanorods had stacking faults along the growth direction composed of alternating ZB and WZ phases, which are caused by the 60° rotation of three In-As bonds of tetrahedral unit around the growth direction at the topmost surface layer of InAs nanorods during the incorporation of adatoms.⁶³ The typical intermixed structure observed for the InAs nanorods could readily occur because of the very small energy difference between the ZB and WZ polytypes, *i.e.*, *ca.* 5 meV/atom,⁶⁴ as well as their atomically identical

(0001) and {111} facets.

HR-TEM images and FFT patterns showed different features depending on the crystallographic orientations of InAs nanorods observed. Single crystalline lattice image of nanorod and spotty FFT pattern were only observed in Figure 6.3a and d, since these images were obtained along twinning direction of $[10\bar{1}0]_{WZ}/[2\bar{1}\bar{1}]_{ZB}$ where twin defects cannot be observed. On the other hand, high density of rotational twin and resulting streaky FFT pattern were clearly observed along the growth direction in Figure 6.3c and f because these images were obtained along a direction of $[11\bar{2}0]_{WZ}/[1\bar{1}0]_{ZB}$, commonly used for twin observation.^{62,65,66} HR-TEM image and corresponding FFT pattern in Figure 6.3b and e were acquired along a direction of $[41\bar{5}0]_{WZ}/[3\bar{2}\bar{1}]_{ZB}$ between orientations represented in Figure 6.3a and c, as displayed in the inset.

After the InAs nanorods growth was completed, RHEED patterns were also recorded in a growth chamber along the same three orientations as the TEM diffraction geometry (Figure 6.3a–c, top). The scale of the RHEED pattern was adjusted to the FFT micrograph of the HR-TEM images by using Si peaks as a reference; the distances between the RHEED streaks originating from the Si(111) substrate were compared with those between the FFT peaks from Si. Figure 6.3a–c showed that the RHEED patterns perfectly matched the FFT patterns at all of the orientations, indicating a direct correlation of RHEED transmission mode with electron diffraction in TEM.

The correspondence between RHEED transmission mode and electron

diffraction in TEM was further examined by comparing RHEED diffraction patterns with simulated diffraction patterns obtained from twinned ZB and WZ phases of InAs nanorods. Figure 6.3g–i shows simulated diffraction patterns with ZB and WZ phases overlapped around their origins at each orientations. Twinned ZB diffraction patterns in Figure 6.2h and i were obtained by twinning corresponding ZB patterns on the (111) plane and overlapping them around their origins, as also represented as L and R chirality in the figures. Details concerning the diffraction patterns of each phase and chirality are displayed in Figure 6.4.

Comparison between RHEED and simulated diffraction patterns reveals that the RHEED patterns also coincide with the mixed simulated patterns for all of the orientations. This strongly suggests that the RHEED spotty patterns are indeed reproducing the electron diffraction patterns of the 3-D materials in TEM, which is not the case when using RHEED in the conventional reflection mode. This results demonstrate the utility of RHEED transmission mode for *in situ* structural observations and analyses during the growth of nanostructures.

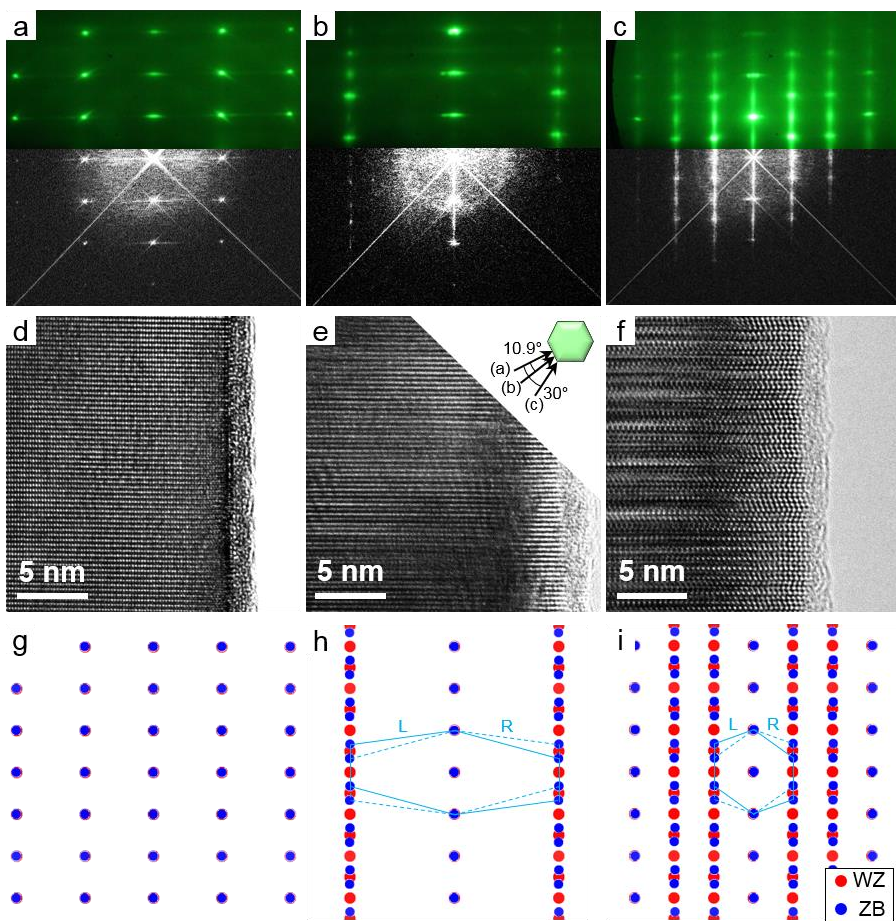
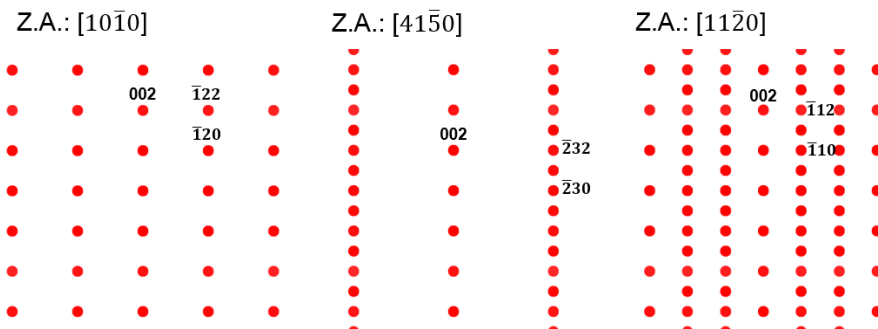


Figure 6.3. Correlation between RHEED and TEM diffraction patterns.
 (a–c) Overlap of (top) RHEED patterns and (bottom) corresponding FFT patterns obtained from the HR-TEM images in (d)–(f) taken along the directions of (a) $[10\bar{1}0]$ wz/ $[2\bar{1}\bar{1}]$ zB, (b) $[41\bar{5}0]$ wz/ $[3\bar{2}\bar{1}]$ zB, and (c) $[1\bar{1}\bar{2}0]$ wz/ $[\bar{1}\bar{1}0]$ zB, respectively. (d–f) HR-TEM images of InAs nanorods taken along the same three orientations. Inset of (e) displays the relationship between these orientations. (g–i) Simulated electron diffraction patterns along the same three directions of (a)–(c), respectively. Red and blue dots represent diffraction spots for WZ and ZB, respectively. (h) and (i) also consist of symmetric twinned ZB structures, as illustrated in detail in Figure 6.4.

InAs (wurtzite)



InAs (zinc blende)

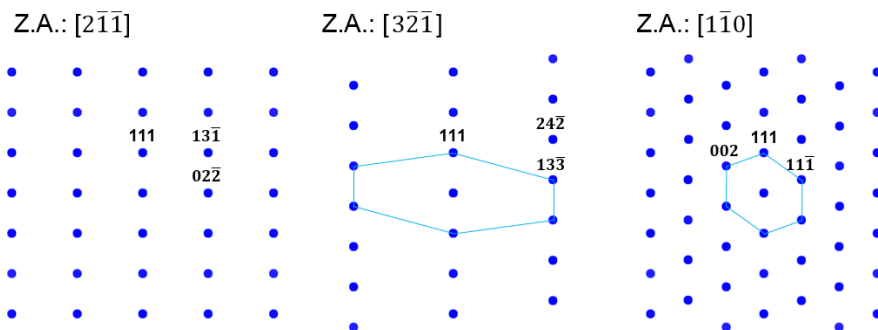


Figure 6.4. Simulated electron diffraction patterns of InAs WZ and ZB phases obtained along the three different orientations. Diffraction patterns of InAs ZB phase were acquired from ZB phase with L chirality depicted in Figure 6.3h and i.

Figure 6.3 only showed RHEED diffraction patterns of the vertically well-aligned InAs nanorods. The RHEED patterns, however, can also be acquired from the nanorods with varied alignment, and they provide a range of information such as crystal growth direction, degree of vertical alignment, and in-plane misorientation of the entire nanorods. Figure 6.5a shows various RHEED patterns depending on crystal growth directions of InAs nanorods. The

different growth directions of the nanorods were obtained by using different surface orientations of Si substrates. The nanorods were epitaxially grown in a direction normal to (111) plane of the Si substrate; vertically on Si(111) substrate or tilted 54° and 36° away from the surface normal on Si(100) and Si(110), respectively, as shown in the schematic diagrams and SEM images in Figure 6.5a. RHEED diffraction patterns constructively generated from these nanorods reflect their structural information, *i.e.*, diffraction spots of (0002)_{wz}/(111)_{ZB} appeared pointing towards the growth direction of nanorods. This indicates that the dominant growth direction of the entire nanorods can be easily identified by analyzing the (0002)_{wz}/(111)_{ZB} spot of RHEED patterns.

The degree of vertical alignment of the nanorods can be also predicted by the RHEED patterns. Figure 6.5b shows RHEED patterns depending on the vertical alignment of the InAs nanorods grown on Si(111) substrate. InAs nanorods were sometimes bent during the growth due to the inappropriate growth condition as shown in the SEM image, termed as ‘Poor vertical alignment’ in Figure 3b. Such bent nanorods were responsible for the dispersed RHEED patterns, whereas the vertically well-aligned nanorods produced spotty patterns. The spread of the RHEED patterns increased as the degree of vertical alignment of the nanorods lowered as shown in the series of RHEED patterns in Figure 3b. In the following sections, the epitaxially grown nanorods with a good vertical alignment are only considered, which are advantageous for diverse applications including electronic and optoelectronic devices.⁶⁷

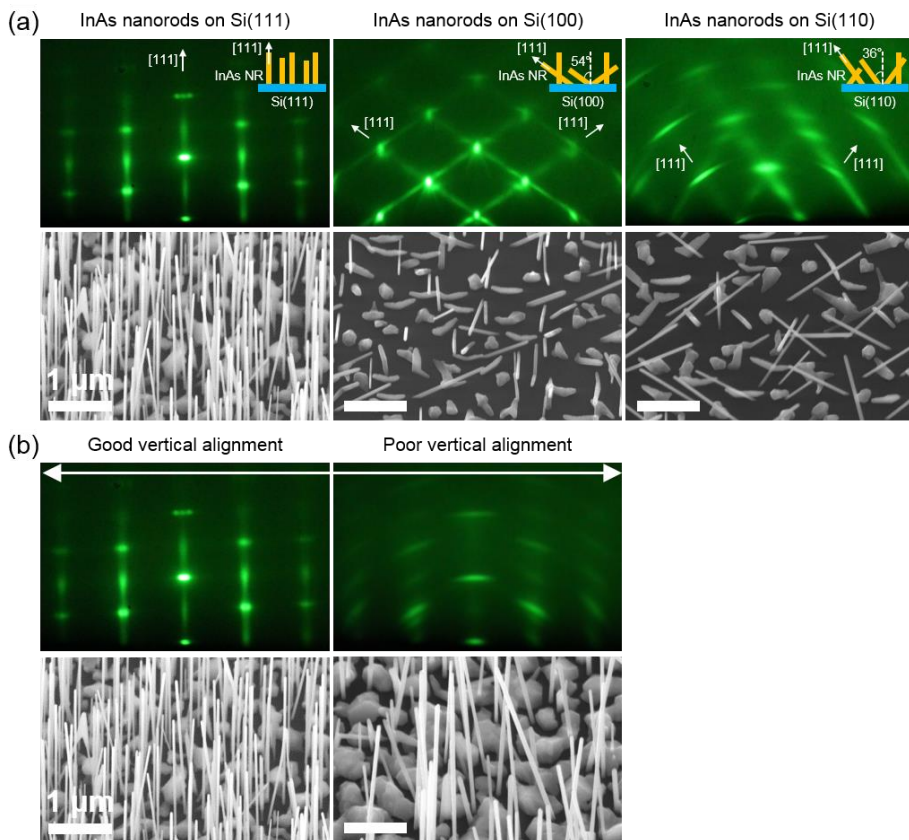


Figure 6.5. RHEED patterns of poorly-aligned InAs nanorods. (a) (top) RHEED patterns of InAs nanorods grown on Si(111), Si(100) and Si(110) substrates. (bottom) Corresponding SEM images of InAs nanorods. A schematic diagram of InAs nanorods representing their crystal growth direction is displayed in each RHEED pattern. (b) (top) RHEED patterns depending on the vertical alignment of InAs nanorods grown on Si(111) substrates. (bottom) Corresponding SEM images of InAs nanorods. All of the RHEED patterns were acquired along the $[1\bar{1}\bar{2}0]_{\text{WZ}}/[1\bar{1}0]_{\text{ZB}}$ direction of the nanorod.

6.4 Growth mechanism of InAs nanorods and GaAs($In_xGa_{1-x}As$)/InAs coaxial nanorods

6.4.1 Initial growth behavior of InAs nanorods

Using RHEED transmission mode combined with TEM measurements, initial growth behavior of InAs nanorods was investigated. Figure 6.6a–c shows RHEED patterns acquired at different growth stages. RHEED pattern in Figure 6.6a was taken just before the growth began, thus the streaky pattern arose from the surface of Si(111) substrate. The spotty pattern emerged, and the streaky pattern from Si(111) substrate was faded away in a few seconds after the growth started as shown in Figure 6.6b. Such a sudden appearance of Bragg spots and disappearance of streaky pattern on the initiation of the growth suggest a catalyst-free crystal growth of InAs nanorods on Si(111) substrate. This is contrary to VLS-type growth of nanorods forming amorphous catalyst at the nucleation stage, which leads to a delayed transition from streaky to spotty pattern.⁵⁸ The Bragg spots appeared at different locations with respect to those of streaks from Si(111) substrate, indicating an abrupt change in the d-spacing and, as a result, rapid in-plane strain relaxation of InAs nanorods. Both ZB and WZ peaks were observed in the RHEED pattern with the epitaxial relationship of InAs $[10\bar{1}0]_{WZ}/[\bar{1}\bar{1}2]_{ZB} \parallel Si \ [\bar{1}\bar{1}2]$ and InAs $(0002)_{WZ}/(111)_{ZB} \parallel Si \ (111)$.

More close inspection of Figure 6.6b revealed that characteristic spots, so called twin-ZB and WZ-sensitive spots,⁶⁸ appeared at the early growth stage

of nanorods, which are marked by blue and yellow arrows, respectively. Twin-ZB pattern refer to superimposed double diffraction spots from twinned ZB phase in an individual nanorod, as denoted with L and R chirality in Figure 6.3i. This may also indicate coexistence of twin orientations in different nanorods. Interestingly, these characteristic spots nearly disappeared as the growth proceeded, and only streak patterns and other spots remained, as shown in Figure 6.6c.

It is worth noting that both twin-ZB and WZ-sensitive spots appeared only at the early growth stage of InAs nanorods. In previous studies, InAs nanorods with alternating ZB and WZ phases commonly exhibited streaky patterns along the growth direction with almost no intensity of both twin-ZB and WZ-sensitive characteristic spots in the diffraction pattern. This is because such heavily disordered stacking of nanorods could not be indexed by ZB and WZ phases anymore.^{66,68,69} This unexpected appearance of both characteristic peaks and their disappearance could be attributed to the structural transformation of InAs nanorods during the growth. At the initiation of the growth, InAs nanorod might be composed of relatively thick ZB and WZ layers rather than commonly reported heavily twinned structures. When such thick ZB and WZ phases possess their own crystal structures, there characteristic peaks could appear in the diffraction patterns as shown in Figure 6.6b. As the growth proceeded, however, the crystal structure of InAs nanorods would be transformed into typical disordered structure, which results in distinctive streaky patterns with no intensity of characteristic spots in the diffraction

pattern. This exactly corresponds to the RHEED pattern in Figure 6.6c which was obtained from almost fully-grown nanorods.

The structural transformation of InAs nanorods was further proved using subsequent TEM measurements. In order to confirm the crystal structure of InAs nanorods at the initial growth stage, InAs nanorods were grown only for 30 s under the same growth condition as shown in Figure 6.2b. Cross-sectional HR-TEM image of the nanorod revealed relatively thick ZB and WZ layers with more than 10–50 atomic layers at the early growth stage, whereas fully-grown nanorods normally exhibited a periodicity of a few atomic layers (Figure 6.6e). FFT patterns in Figure 6.6f and g obtained from these ZB and WZ layers in Figure 6.6e clearly defines twin-ZB and WZ-sensitive spots as indicated by blue and yellow arrows in the pattern, respectively. This is also responsible for the observation of superimposed characteristic spots of the RHEED pattern in Figure 6.6b. These experimental findings by both *in situ* RHEED transmission mode and TEM eventually confirm the structural transition of InAs nanorods at the initial growth stage.

The structural transformation of InAs nanorods is closely associated with a transition in local growth conditions from In-rich to As-rich at the early growth stage. Under high As overpressure employed in the present study, the energetically most favorable As-rich (2×2) reconstructed (111)B surface structure whose unit cell consists of As-trimmers preferentially appears.^{60,70,71} This modifies the surface energies for preferential twin and stacking fault formation, allowing the formation of stacking faults and rotational twin defects

on the (111)B growth plane. However, this is not the case in the very early stage of the InAs nanorods growth. A large amount of In species are required for the nucleation of nanorods under high As-rich growth conditions, which arrive on specific sites, such as the edge of remaining oxide on Si substrate or Si nanocrystals.^{72,73} In adatoms could be easily supplied to the nucleation sites by their high diffusivity on the Si substrate just before nucleation of nanorods. Such local In-rich condition resulted in the distinct surface structure other than As-rich (2×2) reconstructed (111)B surface,^{60,74} which possibly allowed the formation of relatively thick ZB and WZ layers even in the As-rich growth conditions. The local In-rich condition on the substrate at the early growth stage was also evidenced by fast growth rates of nanorods (200 nm/85 s = 8.5 μm/h) due to high supply of In adatoms, compared to the overall growth rates of nanorods (3–4 μm/80 min = 2–3 μm/h).^{66,74} The As-rich conditions were then immediately restored while the supply rate of In species to the tip of an individual nanorod decreased because of increasing diameter and density of the InAs nanorods, which eventually induced the formation of rotational twins in the nanorods (Figure 6.6d).

The growth mechanism of InAs nanorods was explained in detail in Figure 6.7. As mentioned above, the appearance of streaks in the FFT micrographs indicates that the InAs nanorods are composed of heavily twinned structures with alternating WZ and ZB phases. High density of stacking faults formed even at the very early stages of growth, which led to the formation of nanorods without thick ZB and WZ layers at the base (case (1)). However, thick

ZB and WZ layers developed for most of the nanorods at the initial stage as shown in Figure 6.6e, which still remained at the base of the fully-grown nanorods (case (2)). Such a structural transition is attributed to the local growth condition transition from In-rich to As-rich at the initial growth stage. Nanoislands, which did not grow into nanorods with high aspect ratio, normally formed when the initial growth proceeded in a growth direction other than [0001]_{WZ}/[111]_{ZB} (case (3)). These nanoislands, however, rarely contribute to the formation of RHEED patterns because the number of nanoislands is very small compared to that of nanorods and their crystallographic orientations are not aligned each other well enough to give constructive interference pattern.

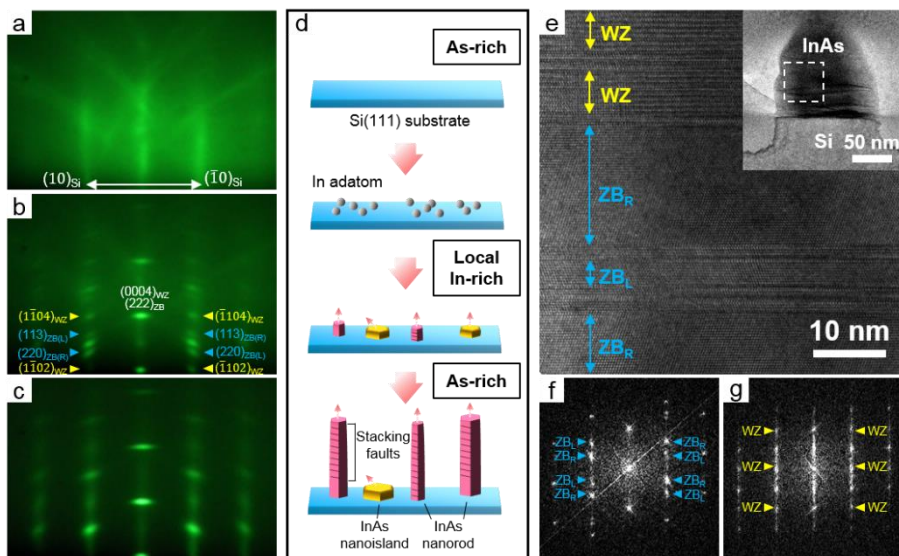


Figure 6.6. Real-time observation of the initial growth behavior of InAs nanorods on the Si(111) substrate. (a–c) RHEED patterns obtained (a) just before the start of growth, and (b) 30 s and (c) 15 min after growth commencement, respectively. Streaks in (a) and diffraction spots in (b) are indexed in the figures. (d) Schematic illustration of the growth behavior of InAs nanorods on the Si(111) substrate. (e) HR-TEM image of InAs nanorod grown for 30 s, taken at the region indicated in the inset. The inset shows a low-magnification image of InAs nanorod. (f,g) FFT patterns obtained for (f) twinned ZB and (g) WZ regions in (e), respectively. Twin-ZB and WZ-sensitive spots are denoted by blue and yellow arrows in (f) and (g), respectively. All of the RHEED and TEM diffraction patterns were taken along the $[11\bar{2}0]_{\text{WZ}}/ [1\bar{1}0]_{\text{ZB}}$ direction to distinguish the ZB and WZ spots.

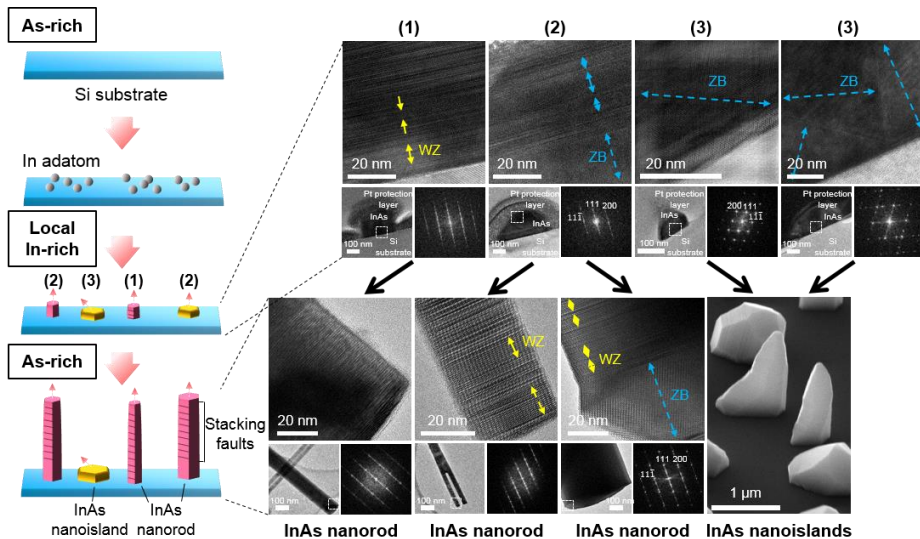


Figure 6.7. Growth mechanisms of InAs nanorods. The four image sets at the top show the crystal structures of the InAs nanorods at the interface with the Si(111) substrate at an early stage of growth. The four lower image sets show the crystal structures of fully-grown InAs nanorods and nanoislands at the base. Each image set consists of a low-magnification BF image of InAs nanorods, HR-TEM image obtained from the region indicated by the dashed square in the BF image and FFT micrograph obtained from the HR-TEM image. The last image at the bottom is SEM image showing InAs nanoislands. ZB and WZ layers free of stacking faults are indicated in the figures by dashed arrows along the $[0001]_{\text{WZ}}/[111]_{\text{ZB}}$ growth direction. The data shown here are representative of more than 10 nanorods.

6.4.2 Strain relaxation of shell layers during the epitaxial growth

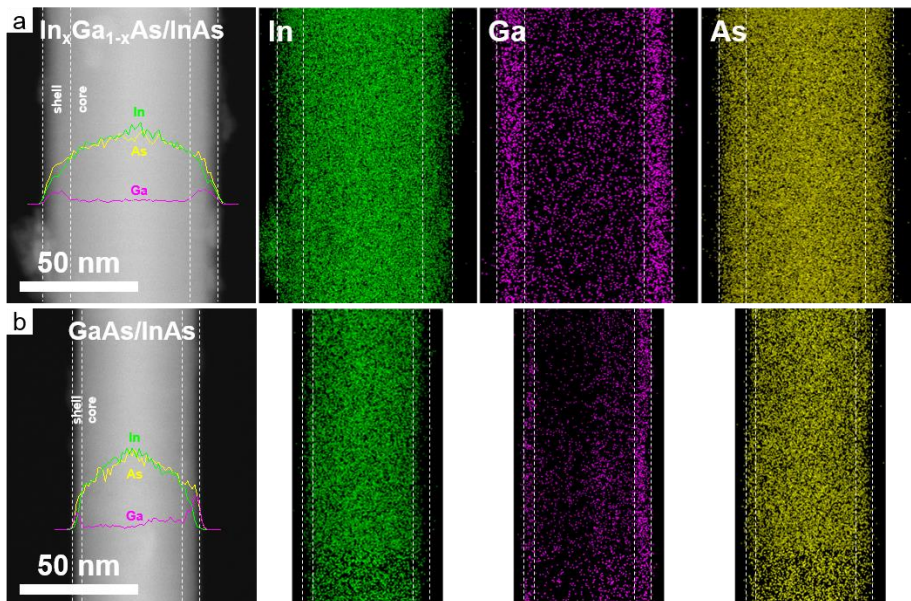


Figure 6.8. $\text{In}_x\text{Ga}_{1-x}\text{As}/\text{InAs}$ and GaAs/InAs coaxial nanorods. HAADF-STEM images of (a) $\text{In}_x\text{Ga}_{1-x}\text{As}/\text{InAs}$ and (b) GaAs/InAs coaxial nanorods and corresponding EDS element maps of In, Ga, and As, respectively. EDS line profiles of In, Ga, and As were obtained across the coaxial nanorods, and displayed in each HAADF-STEM image. The interfaces and edges of the coaxial nanorods were marked by white-dashed lines by comparing HAADF-STEM images and EDS element maps and line profiles.

The growth behavior of $\text{In}_x\text{Ga}_{1-x}\text{As}$ ($0.8 < x < 0.85$) and GaAs shell layers on InAs nanorods was examined in real time using RHEED transmission mode. After growing InAs core nanorods, $\text{In}_x\text{Ga}_{1-x}\text{As}$ and GaAs shell layers were epitaxially grown on the core nanorods, as shown in Figure 6.2c and d. Core-shell structures of the nanorods was clearly confirmed by High-angle annular dark-field scanning TEM (HAADF-STEM) images and EDS mapping,

as displayed in Figure 6.8. Both images revealed that \sim 10-nm-thick $\text{In}_x\text{Ga}_{1-x}\text{As}$ and \sim 5-nm-thick GaAs shell layers were coated on the InAs core nanorods with a diameter of \sim 50 nm.

Figure 6.9a and b shows HR-TEM images obtained along $[11\bar{2}0]_{WZ}/[1\bar{1}0]_{ZB}$ direction at the edge of $\text{In}_x\text{Ga}_{1-x}\text{As}/\text{InAs}$ and GaAs/InAs coaxial nanorods, respectively. As the interfaces between the core-shell layers and InAs core nanorods were hardly distinguishable in the HR-TEM images, both the interfaces and edges of coaxial nanorods were marked by white dashed lines in the figures by comparing HR-TEM images and EDS line scan results. During the growth of $\text{In}_x\text{Ga}_{1-x}\text{As}$ and GaAs coating layers, RHEED patterns were acquired at different growth stages as displayed in Figure 6.9c and d, respectively.

The coaxial coating of $\text{In}_x\text{Ga}_{1-x}\text{As}$ shell layers did not show any change in the RHEED diffraction patterns (Figure 6.9c). This suggests that the $\text{In}_x\text{Ga}_{1-x}\text{As}$ coating layers, which have almost no lattice mismatch with InAs, were grown epitaxially with almost same crystal structures and lattice constants as those of InAs core nanorods. The only change observed was that the intensities of RHEED spots decreased as the growth proceeded due to increased thickness of coaxial nanorods which leads to a lower transmission probability of electron beam.

In contrast to $\text{In}_x\text{Ga}_{1-x}\text{As}$ shell layers, the evolution of the RHEED diffraction spots were observed during the coaxial coating of GaAs having \sim 7% lattice mismatch with InAs. RHEED spots of GaAs split off those of InAs at

the initial stage of coaxial coating and evolved gradually into the position matching with the lattice constants of GaAs, as clearly evidenced by both GaAs (0002)_{WZ}/(111)_{ZB} and (0004)_{WZ}/(222)_{ZB} spots in Figure 6.9d. Additionally, the intensities of the GaAs and InAs spots changed as the growth proceeded; the intensities of InAs spots increasingly darkened and those of GaAs spots became brighter. Such intensity changes are attributed to the increasing amount of GaAs shell layers as well as relatively low transmittance of RHEED electron beam through the thick InAs core nanorods compared with the thin GaAs shell layers.

To trace the evolution of the RHEED diffraction spots in more detail, the shift of intensity profiles around the InAs (0004)_{WZ}/(222)_{ZB} and GaAs (0004)_{WZ}/(222)_{ZB} spots were examined at each growth stage of $In_xGa_{1-x}As$ shell layers (Figure 6.9e). The graph clearly shows that GaAs spot abruptly appeared and gradually evolved into the location corresponding to its own lattice constant over time. The transitional behavior of RHEED spots suggests that GaAs coaxial coating layers were formed epitaxially on InAs core nanorods at the early stage of growth, having the same crystal structures and lattice constants with those of InAs, but returned back to its own lattice constants as the growth proceeded.

In order to relate microstructural characteristics of $In_xGa_{1-x}As$ and GaAs coaxial nanorods to the movement of the RHEED spots, Fourier filtered HR-TEM images were further obtained. Figure 6.10b and d displays the Fourier filtered images obtained from corresponding HR-TEM images of $In_xGa_{1-x}As$ and GaAs coaxial nanorods in Figure 6.10a and c, respectively. Whereas $In_xGa_{1-x}As$

xAs shell layers showed no dislocation nearby the interface except for the defects possibly caused by the imperfect crystal growth of coaxial nanorods, GaAs shell layers commonly showed dislocations originating from large lattice mismatch between GaAs and InAs. The generation of extra half planes corresponding to $(111){ZB}/(0002)_{WZ}$ in the GaAs shell layers results from their strain relaxation during the growth, which is responsible for the evolution of GaAs RHEED spots and lattice constants as shown in Figure 6.9d and e. This commensurate growth behavior of coaxial coating followed by the introduction of dislocations to relieve the interior strain is analogous to the conventional principle in the epitaxial growth of thin films on a substrate with different lattice constants.

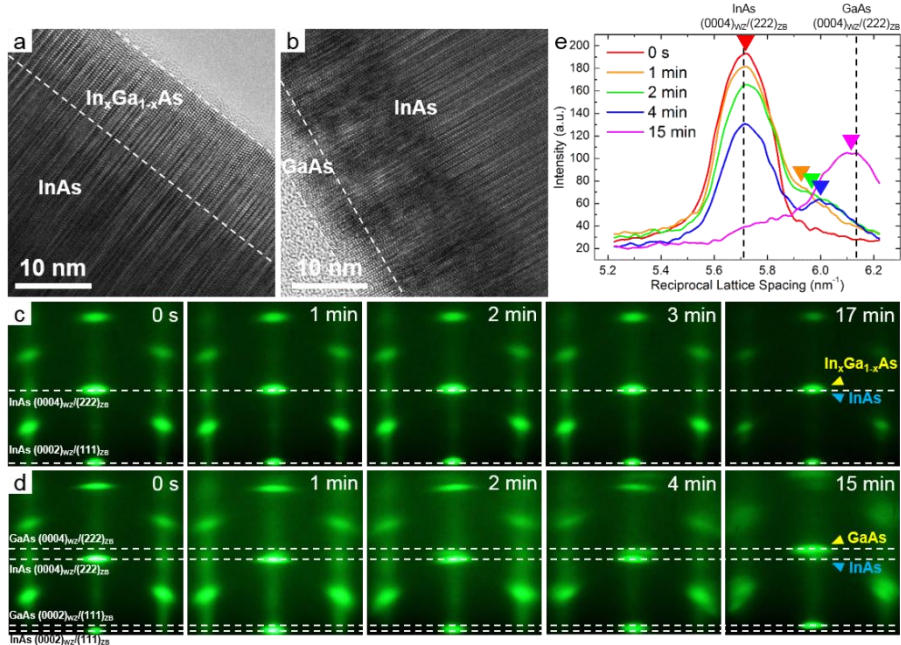


Figure 6.9. Real-time structural analysis of the shell layers during the coaxial coating on InAs core nanorods. (a,b) HR-TEM images of (a) $\text{In}_{x}\text{Ga}_{1-x}\text{As}/\text{InAs}$ and (b) GaAs/InAs coaxial nanorods. (c,d) Series of RHEED patterns acquired during (c) $\text{In}_{x}\text{Ga}_{1-x}\text{As}$ and (d) GaAs shell layers coating on InAs nanorods. All of the RHEED patterns are aligned with respect to their transmitted beams as zero points, which are not shown in the images. The growth time for each RHEED pattern is indicated in the image. All of the RHEED patterns were obtained along a direction of $[11\bar{2}0]_{\text{WZ}}/[1\bar{1}0]_{\text{ZB}}$. (e) RHEED intensity profiles around $\text{InAs}(0004)_{\text{WZ}}/(222)_{\text{ZB}}$ and $\text{GaAs}(0004)_{\text{WZ}}/(222)_{\text{ZB}}$ spots at growth times of 0, 1, 2, 4 and 15 min in (d). The RHEED intensities were measured along the central vertical line intersecting the $(000l)_{\text{WZ}}$ diffraction spots. The positions of the GaAs peaks at which the GaAs spots appeared are indicated by arrows on the plots. The expected positions of the GaAs and InAs spots corresponding to their lattice constants of $(0002)_{\text{WZ}}/(111)_{\text{ZB}}$ and $(0004)_{\text{WZ}}/(222)_{\text{ZB}}$ are indicated by dashed lines in (c)–(e).

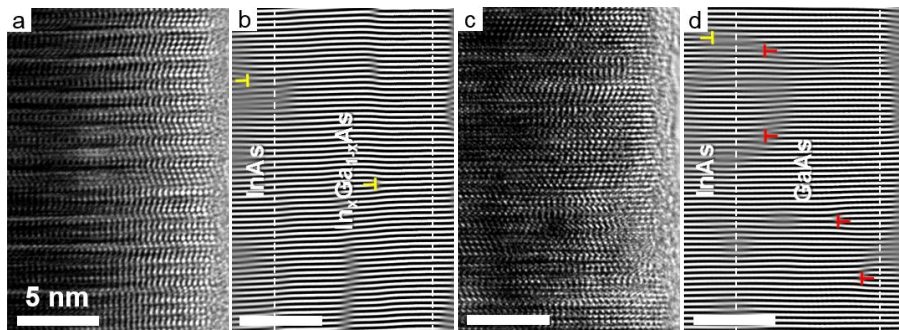


Figure 6.10. Microstructural defects within the shell layers of coaxial nanorods. (a,c) HR-TEM images of $\text{In}_x\text{Ga}_{1-x}\text{As}/\text{InAs}$ and GaAs/InAs coaxial nanorods obtained along the $[11\bar{2}0]_{\text{WZ}}/[1\bar{1}0]_{\text{ZB}}$ direction. (b,d) Corresponding Fourier-filtered images obtained by selecting FFT $(0002)_{\text{WZ}}/(111)_{\text{ZB}}$ spots of (a) and (c), respectively. The locations of dislocations are indicated by the ‘T’ symbol. The yellow and red colors of the symbol represent extra half-planes inserted toward the InAs core nanorod and toward the edge of the shell layer, respectively. The edge of the nanorods and the interfaces between the core and shell layers were identified by EDS line scans and are indicated by the white-dashed lines in (b) and (d).

6.4.3 InAs nanorods growth on graphene layers

As the importance of hybrid heterostructures based on graphene becomes growing, the growth behavior of InAs nanorods on graphene layers was also studied.⁷⁵ InAs nanorods were grown on CVD graphene by catalyst-free MBE method, the same equipment and growth method used for the growth of InAs nanorods on Si(111) substrate. RHEED patterns were monitored and acquired during the whole growth process. Figure 6.11a and b shows the snapshots of RHEED patterns taken before and after the growth of InAs nanorods, respectively. Before the initiation of the growth, ring and streaky patterns were only observed as shown in Figure 6.11a. Such ring patterns, which were not observed for crystalline Si(111) substrate, are ascribed to polycrystalline characteristics of CVD graphene placed on SiO₂/Si substrate. As the growth of InAs nanorods began, the spotty patterns abruptly appeared and the ring and streaky patterns suddenly disappeared. These changes occurred in a few seconds after the growth began, as evidenced by intensity change of RHEED patterns in Figure 6.11c. In particular, the inset of i represented the abrupt appearance of spotty pattern arising from InAs nanorods. This result accords with the appearance and disappearance of RHEED patterns observed for the growth of InAs nanorods on Si(111) in Figure 6.6, thereby suggesting catalyst-free growth of InAs nanorods on graphene layers.

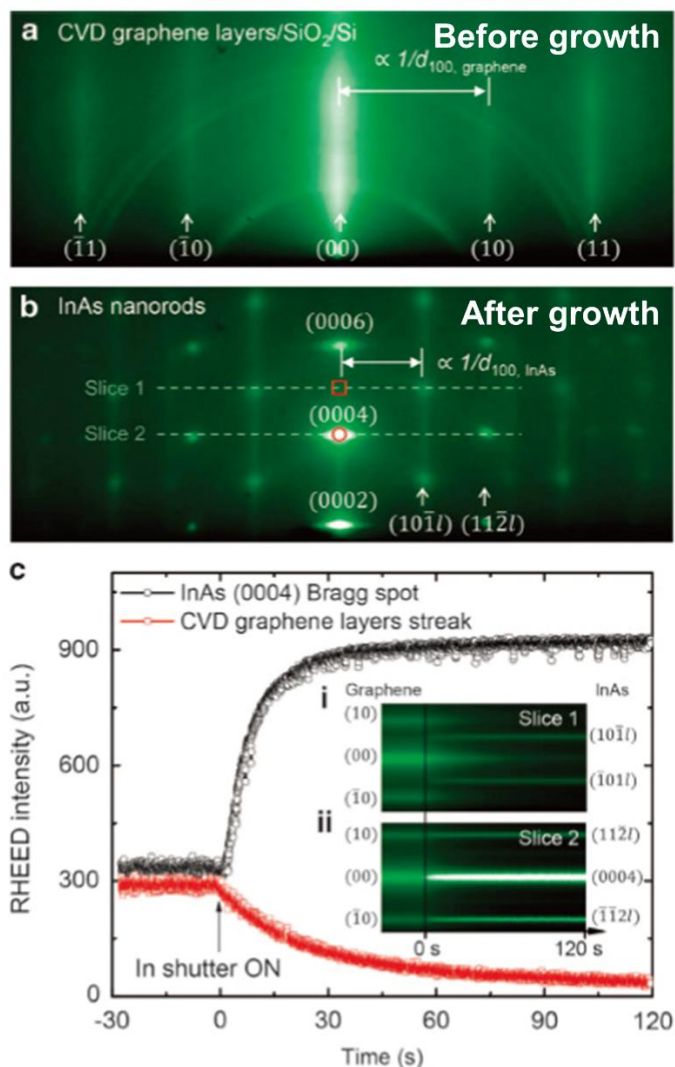


Figure 6.11. RHEED patterns acquired during the growth of InAs nanorods on graphene layers. (a) Streaky and ring patterns from graphene layers obtained before the growth. (b) Spotty pattern of InAs nanorods obtained after the growth. (c) Intensity changes of RHEED spotty patterns as the growth proceeded. Black and red profiles are obtained in the square and circular boxes in (b), respectively, during the growth. The insets denoted as i and ii represent intensity changes in the positions identified with white-dashed lines of Slice 1 and 2 in (b), respectively.⁷⁵

6.5 Summary and outlook

In summary, the RHEED transmission mode combined with TEM measurements was successfully employed for real-time observation and structural analysis of InAs nanorods and GaAs($\text{In}_x\text{Ga}_{1-x}\text{As}$)/InAs coaxial nanorods growth. Using this combined method, structural change of InAs nanorod caused by a transition in local growth condition from In-rich to As-rich at the initial growth stage was found. Additionally, lattice constants evolution and strain relaxation of GaAs/InAs coaxial nanorods during shell layers coating were thoroughly investigated. The RHEED transmission mode exhibits many advantages over conventional *ex situ* characterization techniques in various aspects. The real-time characterization technique allows us to obtain structural information of nanostructures during the growth without post-sampling processes which may induce mechanical and chemical damages on a specimen. Additionally, real-time monitoring using RHEED transmission mode can avoid structural or phase change of a specimen caused by its exposure to the atmosphere and retarded annealing in a growth chamber during cool-down after the growth, which restricts the analysis of nucleation and growth of nanomaterials. The other advantage is that RHEED provides collective information over large area because of its large electron beam size, which provides the representative characteristics of the whole sample. Moreover, this technique provides more accurate and detailed information when used with following TEM measurements, thereby providing a complete range of information which was not achievable with typical *ex situ* characterization

methods. Detailed information obtained by this combined method could be highly valuable for controlling the growth of functional nanostructures, such as for the fabrication of stacking fault-free III-V nanorods or strain-controlled coaxial nanorods. This also provides the opportunity for the realization of their novel properties and application to the future electronics and optoelectronics. More importantly, this work has a great potential to stimulate a new field of research concerning the *in situ* observation of nanostructures growth and to enhance our understanding of crystal growth and of other areas beyond our current knowledge.

CHAPTER 7

Conclusions

7.1 Summary

In this study, the growth mechanisms of compound semiconductor nanostructures on 2-D materials such as graphene were investigated using TEM. In order to avoid damages on fragile nanomaterials arising from conventional TEM sample preparation processes, ‘direct growth and observation’ techniques were newly introduced. Using these methods, the growth mechanisms of three different materials systems were thoroughly studied; (1) ZnO nanomaterials on graphene layers (Chapter 4), (2) GaAs/SLG/InAs double heterostructures (Chapter 5), and (3) InAs nanorods and GaAs($In_xGa_{1-x}As$)/InAs coaxial nanorods on Si(111) and graphene layers (Chapter 6).

In Chapters 4 and 5, the ‘direct growth and observation’ methods using a graphene template were discussed. Basically, these techniques ensured atomic-resolution observation of the growth behavior of nanomaterials with

TEM by growing nanomaterials directly on graphene placed on a commercial holey carbon TEM grid or a prefabricated SiNx membrane TEM grid. Graphene exhibiting excellent electron beam transparency and high mechanical strength was employed as an ideal supporting layer for TEM measurements by minimizing the background signal from the underlying thick membrane. In addition to merely sustaining nanomaterials as a support, graphene was further used as a crystalline substrate for nanomaterials growth. The crystalline nature of graphene along with its electron beam transparency enabled direct atomic-resolution imaging of nanomaterials over the suspended regions without conventional TEM sample preparation processes. Therefore, this ultimately allowed us to systematically investigate the initial growth mechanisms of nanomaterials.

Firstly, the initial growth behavior of ZnO nanomaterials on graphene was studied using the ‘direct growth and observation’ method. Transition of the ZnO phase from uncommon rocksalt to the most stable wurtzite, governed by kinetics based on the competition between interfacial energy and bulk Gibb free energy of ZnO nuclei, was clearly observed at the nucleation stage. Additionally, atomic-resolution imaging revealed that $\Sigma 7$ CSL boundaries were dominantly generated with their characteristic atomic configurations during the coalescence of grains having different crystallographic orientations. Next, the growth behavior of GaAs/SLG/InAs double heterostructures was also examined. The comparisons between the growth behavior of GaAs on bare SLG and on SLG/InAs nanorods heterostructures revealed that the nucleation and growth of

GaAs were influenced by the presence as well as the growth direction of InAs nanorods underneath SLG. Such interaction through SLG was confirmed by the growth direction flip of GaAs clusters which mimic the growth direction of InAs nanorods underneath SLG.

In Chapter 6, the ‘direct growth and observation’ method using RHEED transmission mode was discussed. Basically, this technique ensured real-time structural analysis by analyzing the diffraction patterns obtained during the growth of nanomaterials. RHEED was newly used in transmission mode which is analogous to the electron diffraction in TEM, thereby providing structural information of nanomaterials. RHEED transmission mode allowed the study on intermediates states during the nucleation and epitaxial growth of hetero-nanostructures, which was not attainable by traditional *ex situ* characterization methods. Moreover, when this technique was combined with TEM, real-time observation of the growth behavior of nanomaterials by RHEED transmission mode and chemical and structural analysis with excellent spatial resolution by TEM offered unprecedented scopes and details of knowledges in nanostructure growth.

Using RHEED transmission mode combined with TEM measurements, structural change of InAs nanorods from pure ZB/WZ phases to heavily defective twinning structures were observed at the very early stage of growth. The origin of the structural change was examined in detail, which has long been considered beyond the realm of direct investigation. In addition, delayed strain relaxation process occurring within the shell layers was clearly

observed during the epitaxial growth of shell layers for the first time.

7.2 Outlook

This work has great values in the scientific and technological aspects. It is believed that the “direct growth and observation” method would offer great opportunities for studying the growth mechanisms of diverse nanomaterials on various 2-D layered materials and the effect of 2-D materials as substrates during the crystal growth by bottom-up approach. Additionally, the techniques developed in this work will open up new research fields in the crystal growth and *in situ* electron microscopy. Further development of these unique approaches are also expected to bring a new paradigm, *i.e.* the fabrication of hybrid heterostructures based on various 2-D materials, in semiconductor science and technology. This achievements will lay the foundation for the realization of hybrid nanostructures applicable to biomedical, display, memory, and information technology. Eventually, the scientific breakthroughs achieved with an aid of newly developed techniques will allow us to meet the required technological revolution for the future industries and provide a means to improve everyday human life in the future.

References

- 1 Lewis, J. "Material challenge for flexible organic devices". *Mater Today*, **9**, 38-45 (2006).
- 2 Liao, C. Z., Zhang, M., Yao, M. Y., Hua, T., Li, L. & Yan, F. "Flexible Organic Electronics in Biology: Materials and Devices". *Adv Mater*, **27**, 7493-7527 (2015).
- 3 Lin, Y. Y., Xu, Z., Yu, D. L., Lu, L. F., Yin, M., Tavakoli, M. M., Chen, X. Y., Hao, Y. Y., Fan, Z. Y., Cui, Y. X. & Li, D. D. "Dual-Layer Nanostructured Flexible Thin-Film Amorphous Silicon Solar Cells with Enhanced Light Harvesting and Photoelectric Conversion Efficiency". *Acs Appl Mater Inter*, **8**, 10929-10936 (2016).
- 4 Nomura, K., Ohta, H., Takagi, A., Kamiya, T., Hirano, M. & Hosono, H. "Room-temperature fabrication of transparent flexible thin-film transistors using amorphous oxide semiconductors". *Nature*, **432**, 488-492 (2004).
- 5 Oh, J. Y., Kim, S., Baik, H. K. & Jeong, U. "Conducting Polymer Dough for Deformable Electronics". *Adv Mater*, **28**, 4455-4461 (2016).
- 6 Takamatsu, S., Lonjaret, T., Ismailova, E., Masuda, A., Itoh, T. & Malliaras, G. G. "Wearable Keyboard Using Conducting Polymer Electrodes on Textiles". *Adv Mater*, **28**, 4485-4488 (2016).
- 7 Krames, M. R., Shchekin, O. B., Mueller-Mach, R., Mueller, G. O., Zhou, L., Harbers, G. & Crawford, M. G. "Status and future of high-power light-emitting diodes for solid-state lighting". *J Disp Technol*, **3**, 160-175 (2007).
- 8 Tsintzos, S. I., Pelekanos, N. T., Konstantinidis, G., Hatzopoulos, Z. & Savvidis, P. G. "A GaAs polariton light-emitting diode operating near room temperature". *Nature*, **453**, 372-375 (2008).
- 9 Kobayashi, Y., Kumakura, K., Akasaka, T. & Makimoto, T. "Layered boron nitride as a release layer for mechanical transfer of GaN-based devices". *Nature*, **484**, 223-227 (2012).

- 10 Liao, L., Lin, Y. C., Bao, M. Q., Cheng, R., Bai, J. W., Liu, Y. A., Qu, Y. Q., Wang, K. L., Huang, Y. & Duan, X. F. "High-speed graphene transistors with a self-aligned nanowire gate". *Nature*, **467**, 305-308 (2010).
- 11 Chung, K., Lee, C. H. & Yi, G. C. "Transferable GaN Layers Grown on ZnO-Coated Graphene Layers for Optoelectronic Devices". *Science*, **330**, 655-657 (2010).
- 12 Lee, C. H., Kim, Y. J., Hong, Y. J., Jeon, S. R., Bae, S., Hong, B. H. & Yi, G. C. "Flexible Inorganic Nanostructure Light-Emitting Diodes Fabricated on Graphene Films". *Adv Mater*, **23**, 4614-4619 (2011).
- 13 Kim, H., Park, J. H., Suh, M., Ahn, J. R. & Ju, S. "Horizontally aligned ZnO nanowire transistors using patterned graphene thin films". *Appl Phys Lett*, **100**, 063112 (2012).
- 14 Kim, Y. J., Yoo, H., Lee, C. H., Park, J. B., Baek, H., Kim, M. & Yi, G. C. "Position- and Morphology-Controlled ZnO Nanostructures Grown on Graphene Layers". *Adv Mater*, **24**, 5565-5569 (2012).
- 15 Munshi, A. M., Dheeraj, D. L., Fauske, V. T., Kim, D. C., van Helvoort, A. T. J., Fimland, B. O. & Weman, H. "Vertically Aligned GaAs Nanowires on Graphite and Few-Layer Graphene: Generic Model and Epitaxial Growth". *Nano Lett*, **12**, 4570-4576 (2012).
- 16 Son, D. I., Kwon, B. W., Park, D. H., Seo, W. S., Yi, Y., Angadi, B., Lee, C. L. & Choi, W. K. "Emissive ZnO-graphene quantum dots for white-light-emitting diodes". *Nat Nanotechnol*, **7**, 465-471 (2012).
- 17 Novoselov, K. S., Geim, A. K., Morozov, S. V., Jiang, D., Zhang, Y., Dubonos, S. V., Grigorieva, I. V. & Firsov, A. A. "Electric field effect in atomically thin carbon films". *Science*, **306**, 666-669 (2004).
- 18 Novoselov, K. S., Jiang, D., Schedin, F., Booth, T. J., Khotkevich, V. V., Morozov, S. V. & Geim, A. K. "Two-dimensional atomic crystals". *P Natl Acad Sci USA*, **102**, 10451-10453 (2005).
- 19 Meyer, J. C., Girit, C. O., Crommie, M. F. & Zettl, A. "Imaging and dynamics of light atoms and molecules on graphene". *Nature*, **454**, 319-

- 322 (2008).
- 20 Lee, C., Wei, X. D., Kysar, J. W. & Hone, J. "Measurement of the elastic properties and intrinsic strength of monolayer graphene". *Science*, **321**, 385-388 (2008).
- 21 Nair, R. R., Blake, P., Grigorenko, A. N., Novoselov, K. S., Booth, T. J., Stauber, T., Peres, N. M. R. & Geim, A. K. "Fine structure constant defines visual transparency of graphene". *Science*, **320**, 1308-1308 (2008).
- 22 McCaffrey, J. P., Phaneuf, M. W. & Madsen, L. D. "Surface damage formation during ion-beam thinning of samples for transmission electron microscopy". *Ultramicroscopy*, **87**, 97-104 (2001).
- 23 Enquist, F. & Spetz, A. "The Fabrication of Amorphous SiO₂ Substrates Suitable for Transmission Electron-Microscopy Studies of Ultrathin Polycrystalline Films". *Thin Solid Films*, **145**, 99-104 (1986).
- 24 Cheong, W. S., Hwang, N. M. & Yoon, D. Y. "Observation of nanometer silicon clusters in the hot-filament CVD process". *J Cryst Growth*, **204**, 52-61 (1999).
- 25 Grant, A. W., Hu, Q. H. & Kasemo, B. "Transmission electron microscopy 'windows' for nanofabricated structures". *Nanotechnology*, **15**, 1175-1181 (2004).
- 26 Zheng, H. M., Smith, R. K., Jun, Y. W., Kisielowski, C., Dahmen, U. & Alivisatos, A. P. "Observation of Single Colloidal Platinum Nanocrystal Growth Trajectories". *Science*, **324**, 1309-1312 (2009).
- 27 Kashchiev, D. *Nucleation : basic theory with applications*. (Butterworth Heinemann, 2000).
- 28 Utama, M. I. B., Zhang, Q., Zhang, J., Yuan, Y. W., Belarre, F. J., Arbiol, J. & Xiong, Q. H. "Recent developments and future directions in the growth of nanostructures by van der Waals epitaxy". *Nanoscale*, **5**, 3570-3588 (2013).
- 29 Koma, A. "Vanderwaals Epitaxy - a New Epitaxial-Growth Method for a Highly Lattice-Mismatched System". *Thin Solid Films*, **216**, 72-76

- (1992).
- 30 Williams, D. B. & Carter, C. B. *Transmission electron microscopy : a textbook for materials science*. 2nd edn. (Springer, 2008).
- 31 Jo, J., Yoo, H., Park, S. I., Park, J. B., Yoon, S., Kim, M. & Yi, G. C. "High-Resolution Observation of Nucleation and Growth Behavior of Nanomaterials Using a Graphene Template". *Adv Mater*, **26**, 2011-2015 (2014).
- 32 Bates, C. H., Roy, R. & White, W. B. "New High-Pressure Polymorph of Zinc Oxide". *Science*, **137**, 993 (1962).
- 33 Decremps, F., Pellicer-Porres, J., Datchi, F., Itie, J. P., Polian, A., Baudelet, F. & Jiang, J. Z. "Trapping of cubic ZnO nanocrystallites at ambient conditions". *Appl Phys Lett*, **81**, 4820-4822 (2002).
- 34 Bobade, S. M. "A reconstruction of cubic rs-ZnO on MgO (200) substrate through (100) plane of w-ZnO:rs-ZnO for transparent electronic application". *Appl Phys Lett*, **100**, 072102 (2012).
- 35 Liu, X. Y. "Interfacial effect of molecules on nucleation kinetics". *J Phys Chem B*, **105**, 11550-11558 (2001).
- 36 Oba, F., Ohta, H., Sato, Y., Hosono, H., Yamamoto, T. & Ikuhara, Y. "Atomic structure of [0001]-tilt grain boundaries in ZnO: A high-resolution TEM study of fiber-textured thin films". *Phys Rev B*, **70**, 125415 (2004).
- 37 Huang, J. Y., Ye, Z. Z., Lu, H. M., Wang, L., Zhao, B. H. & Li, X. H. "Microstructure study of ZnO thin films on Si substrate grown by MOCVD". *J Phys D Appl Phys*, **40**, 4882-4886 (2007).
- 38 Geim, A. K. & Novoselov, K. S. "The rise of graphene". *Nat Mater*, **6**, 183-191 (2007).
- 39 Hong, Y. J., Yang, J. W., Lee, W. H., Ruoff, R. S., Kim, K. S. & Fukui, T. "Van der Waals Epitaxial Double Heterostructure: InAs/Single-Layer Graphene/InAs". *Adv Mater*, **25**, 6847-6853 (2013).
- 40 Kim, Y., Cruz, S. S., Lee, K., Alawode, B. O., Choi, C., Song, Y., Johnson, J. M., Heidelberger, C., Kong, W., Choi, S., Qiao, K.,

- Almansouri, I., Fitzgerald, E. A., Kong, J., Kolpak, A. M., Hwang, J. & Kim, J. "Remote epitaxy through graphene enables two-dimensional material-based layer transfer". *Nature*, **544**, 340-343 (2017).
- 41 Brune, H., Giovannini, M., Bromann, K. & Kern, K. "Self-organized growth of nanostructure arrays on strain-relief patterns". *Nature*, **394**, 451-453 (1998).
- 42 Zuo, J. M. & Li, B. Q. "Nanostructure evolution during cluster growth: Ag on H-terminated Si(111) surfaces". *Phys Rev Lett*, **88**, 255502 (2002).
- 43 Kim, B. J., Tersoff, J., Kodambaka, S., Reuter, M. C., Stach, E. A. & Ross, F. M. "Kinetics of Individual Nucleation Events Observed in Nanoscale Vapor-Liquid-Solid Growth". *Science*, **322**, 1070-1073 (2008).
- 44 Jeong, J. S. & Lee, J. Y. "Investigation of initial growth of ZnO nanowires and their growth mechanism". *Nanotechnology*, **21** (2010).
- 45 Wang, Z. L. & Song, J. H. "Piezoelectric nanogenerators based on zinc oxide nanowire arrays". *Science*, **312**, 242-246 (2006).
- 46 Kim, S. K., Jeong, S. Y. & Cho, C. R. "Structural reconstruction of hexagonal to cubic ZnO films on Pt/Ti/SiO₂/Si substrate by annealing". *Appl Phys Lett*, **82**, 562-564 (2003).
- 47 Sykora, M., Koposov, A. Y., McGuire, J. A., Schulze, R. K., Tretiak, O., Pietryga, J. M. & Klimov, V. I. "Effect of Air Exposure on Surface Properties, Electronic Structure, and Carrier Relaxation in PbSe Nanocrystals". *Ac_s Nano*, **4**, 2021-2034 (2010).
- 48 Kwon, D. H., Kim, K. M., Jang, J. H., Jeon, J. M., Lee, M. H., Kim, G. H., Li, X. S., Park, G. S., Lee, B., Han, S., Kim, M. & Hwang, C. S. "Atomic structure of conducting nanofilaments in TiO₂ resistive switching memory". *Nat Nanotechnol*, **5**, 148-153 (2010).
- 49 Yuk, J. M., Park, J., Ercius, P., Kim, K., Hellebusch, D. J., Crommie, M. F., Lee, J. Y., Zettl, A. & Alivisatos, A. P. "High-Resolution EM of Colloidal Nanocrystal Growth Using Graphene Liquid Cells". *Science*,

- 336, 61-64 (2012).
- 50 Baldi, A., Narayan, T. C., Koh, A. L. & Dionne, J. A. "In situ detection of hydrogen-induced phase transitions in individual palladium nanocrystals". *Nat Mater*, **13**, 1143-1148 (2014).
- 51 Ross, F. M. "Opportunities and challenges in liquid cell electron microscopy". *Science*, **350**, aaa9886 (2015).
- 52 Lim, J., Li, Y. Y., Alsem, D. H., So, H., Lee, S. C., Bai, P., Cogswell, D. A., Liu, X. Z., Jin, N., Yu, Y. S., Salmon, N. J., Shapiro, D. A., Bazant, M. Z., Tyliszczak, T. & Chueh, W. C. "Origin and hysteresis of lithium compositional spatiodynamics within battery primary particles". *Science*, **353**, 566-571 (2016).
- 53 Gaines, J. M. "In-Situ Characterization of II/Vi Molecular-Beam Epitaxy Growth Using Reflection High-Energy Electron-Diffraction Oscillations". *J Cryst Growth*, **137**, 187-194 (1994).
- 54 Braun, W. *Applied RHEED : reflection high-energy electron diffraction during crystal growth*. (Springer, 1999).
- 55 Oliver, R. A., Norenberg, C., Martin, M. G., Castell, M. R., Allers, L. & Briggs, G. A. D. "The effect of V : III ratio on the growth of InN nanostructures by molecular beam epitaxy". *Surf Sci*, **532**, 806-810 (2003).
- 56 Chen, H. Y., Lin, H. W., Shen, C. H. & Gwo, S. "Structure and photoluminescence properties of epitaxially oriented GaN nanorods grown on Si(111) by plasma-assisted molecular-beam epitaxy". *Appl Phys Lett*, **89**, 243105 (2006).
- 57 Soshnikov, I. P., Cirlin, G. E., Tonkikh, A. A., Nevedomskii, V. N., Samsonenko, Y. B. & Ustinov, V. M. "Electron diffraction on GaAs nanowhiskers grown on Si(100) and Si(111) substrates by molecular-beam epitaxy". *Phys Solid State*, **49**, 1440-1445 (2007).
- 58 Rudolph, D., Hertenberger, S., Bolte, S., Paosangthong, W., Spirkoska, D., Doblinger, M., Bichler, M., Finley, J. J., Abstreiter, G. & Koblmuller, G. "Direct Observation of a Noncatalytic Growth Regime

- for GaAs Nanowires". *Nano Lett*, **11**, 3848-3854 (2011).
- 59 Pehlke, E., Moll, N., Kley, A. & Scheffler, M. "Shape and stability of quantum dots". *Appl Phys a-Mater*, **65**, 525-534 (1997).
- 60 Yoshida, H., Ikejiri, K., Sato, T., Hara, S., Hiruma, K., Motohisa, J. & Fukui, T. "Analysis of twin defects in GaAs nanowires and tetrahedra and their correlation to GaAs(111)B surface reconstructions in selective-area metal organic vapour-phase epitaxy". *J Cryst Growth*, **312**, 52-57 (2009).
- 61 Joyce, H. J., Wong-Leung, J., Gao, Q., Tan, H. H. & Jagadish, C. "Phase Perfection in Zinc Blende and Wurtzite III-V Nanowires Using Basic Growth Parameters". *Nano Lett*, **10**, 908-915 (2010).
- 62 Koblmuller, G. & Abstreiter, G. "Growth and properties of InGaAs nanowires on silicon". *Phys Status Solidi-R*, **8**, 11-30 (2014).
- 63 Rajkumar, K. C., Chen, P. & Madhukar, A. "A Transmission Electron-Microscope Study of Twin Structure in Gaas/Gaas (111)B Grown Via Molecular-Beam Epitaxy". *J Appl Phys*, **69**, 2219-2223 (1991).
- 64 Akiyama, T., Sano, K., Nakamura, K. & Ito, T. "An empirical potential approach to wurtzite-zinc-blende polytypism in group III-V semiconductor nanowires". *Jpn J Appl Phys 2*, **45**, L275-L278 (2006).
- 65 Tomioka, K., Motohisa, J., Hara, S. & Fukui, T. "Crystallographic structure of InAs nanowires studied by transmission electron microscopy". *Jpn J Appl Phys 2*, **46**, L1102-L1104 (2007).
- 66 Zhuang, Q. D., Anyebe, E. A., Sanchez, A. M., Rajpalke, M. K., Veal, T. D., Zhukov, A., Robinson, B. J., Anderson, F., Kolosov, O. & Fal'ko, V. "Graphitic platform for self-catalysed InAs nanowires growth by molecular beam epitaxy". *Nanoscale Res Lett*, **9**, 321 (2014).
- 67 Tomioka, K., Yoshimura, M. & Fukui, T. "A III-V nanowire channel on silicon for high-performance vertical transistors". *Nature*, **488**, 189-192 (2012).
- 68 Morkotter, S., Funk, S., Liang, M., Doblinger, M., Hertenberger, S., Treu, J., Rudolph, D., Yadav, A., Becker, J., Bichler, M., Scarpa, G.,

- Lugli, P., Zardo, I., Finley, J. J., Abstreiter, G. & Koblmuller, G. "Role of microstructure on optical properties in high-uniformity $In_{1-x}Ga_xAs$ nanowire arrays: Evidence of a wider wurtzite band gap". *Phys Rev B*, **87**, 205303 (2013).
- 69 Johansson, J., Wacaser, B. A., Dick, K. A. & Seifert, W. "Growth related aspects of epitaxial nanowires". *Nanotechnology*, **17**, S355-S361 (2006).
- 70 Biegelsen, D. K., Bringans, R. D., Northrup, J. E. & Swartz, L. E. "Reconstructions of $GaAs(1\bar{1}\bar{1}1\bar{1}\bar{1}\bar{1})$ Surfaces Observed by Scanning Tunneling Microscopy". *Phys Rev Lett*, **65**, 452-455 (1990).
- 71 Ikejiri, K., Noborisaka, J., Hara, S., Motohisa, J. & Fukui, T. "Mechanism of catalyst-free growth of GaAs nanowires by selective area MOVPE". *J Cryst Growth*, **298**, 616-619 (2007).
- 72 Nesheva, D., Raptis, C., Perakis, A., Bineva, I., Aneva, Z., Levi, Z., Alexandrova, S. & Hofmeister, H. "Raman scattering and photoluminescence from Si nanoparticles in annealed SiO_x thin films". *J Appl Phys*, **92**, 4678-4683 (2002).
- 73 Park, H. D., Prokes, S. M., Twigg, M. E., Cammarata, R. C. & Gailiot, A. C. "Si-assisted growth of InAs nanowires". *Appl Phys Lett*, **89**, 223125 (2006).
- 74 Dimakis, E., Lahnemann, J., Jahn, U., Breuer, S., Hilse, M., Geelhaar, L. & Riechert, H. "Self-Assisted Nucleation and Vapor-Solid Growth of In As Nanowires on Bare Si(111)". *Cryst Growth Des*, **11**, 4001-4008 (2011).
- 75 Tchoe, Y., Jo, J., Kim, M. & Yi, G. C. "Catalyst-free growth of $InAs/In_xGa_{1-x}As$ coaxial nanorod heterostructures on graphene layers using molecular beam epitaxy". *Npg Asia Mater*, **7**, e206 (2015).

초 록

기계적 박리법으로 얻어진 원자단위 두께의 이차원 초박막 물질은 기존에 존재하지 않았던 새로운 물리적 특성들을 발현하여 학계 및 산업계에서 큰 주목을 받고 있다. 또한 이런 이차원 물질들은 기존의 화합물 반도체 박막이나 나노구조체와 결합된 하이브리드 구조를 형성하여 기존의 소자에 유연성, 투명성 등의 다양한 기능성을 새롭게 부여할 것으로 기대되고 있다. 이런 이유로 이차원 물질을 기판으로 활용하여 나노구조물을 그 위에 결정성장시키고 이를 전자/광전자 소자에 적용하고자 하는 많은 연구가 이루어지고 있다. 하지만 우리가 원하는 구조와 물리적 특성을 보이는 나노구조물을 이차원 물질 위에 고품질로 성장시키기 위해서는 핵생성 및 성장, 에피택시 관계의 형성 등 초기결정성장단계를 아주 자세히 연구하는 일이 필수적으로 선결되어야 한다.

본 연구에서는 투과전자현미경을 이용하여 2차원 물질 중 가장 대표적인 그래핀 위에서 성장된 화합물 반도체의 결정성장 메커니즘에 대해 알아보았다. 투과전자현미경 분석에서는 전자빔이 투과할 수 있도록 시편을 아주 얇게 만드는 시편 후처리 과정이 필수적인데 이 과정에서 시편이 의도치 않게 손상될 수 있다. 이런 시편 손상을 피하여 초기결정성장 단계의 아주 작은 크기의 시편을 관찰하기 위해서 개선된 결정성장 및 투과전자현미경 관찰법을 새롭게 제시하였다. 이는 전자빔 투과도가 굉장히 좋은 그래핀을 투과전자현미경 관찰을 위한 그리드의 지지막 뿐만 아니라 결정성장에 필요한 기판으로 활용한 방법으로 그래핀 위에 결정성장 후 시편 후처리 과정 없이 바로 투과전자현미경 관찰을 한 방법이다. 이를 이용해 산화아연(ZnO), 인듐비소(InAs),

갈륨비소(GaAs) 등의 화합물 반도체 나노구조물을 그래핀 위에 성장시키고 시편 후처리 과정 없이 바로 투과전자현미경 관찰을 수행하였다. 또한 본 연구에서는 RHEED 기법을 기존의 반사 방식이 아닌 투과 방식으로 새롭게 활용하여 결정성장 동안 나노구조체의 구조 정보를 실시간으로 얻고 이를 분석하는 연구를 진행하였다. RHEED 전자빔과 나노구조체와의 상호작용으로 인해 형성된 회절패턴은 투과전자현미경에서 나타나는 전자회절기법과 같은 현상이기 때문에 이를 이용해 나노구조체의 구조 정보 분석이 가능함을 확인하였다.

새롭게 제시한 분석법을 이용하여 본 연구에서는 다음 세가지 종류의 화합물 반도체 나노구조물의 결정성장 메커니즘을 분석하였다. 첫 번째로 그래핀을 투과전자현미경 관찰을 위한 지지막 뿐만 아니라 결정성장을 위한 기판으로도 활용하여 산화아연의 결정성장 메커니즘을 원자 단위의 고분해능에서 관찰하는 연구를 수행하였다. 이 방법을 통해 기존에는 알려지지 않았던 입방구조(cubic) 산화아연의 핵생성 과정과 $\Sigma 7$ CSL 결정립계가 주도적으로 형성되는 현상을 확인하였다. 두 번째로는 좀 더 개선된 결정성장 및 투과전자현미경 관찰법을 활용하여 갈륨비소/그래핀/인듐비소 이중 이종구조의 결정성장 메커니즘에 대해 알아보았다. 여기서는 그래핀에 성장되어 있는 인듐비소 나노구조물이 다른 면에서 갈륨비소가 성장되는 과정에 영향을 줄 수 있다는 것을 새롭게 밝혀내었다. 마지막으로는 RHEED 투과 방식 기법을 활용하여 인듐비소 나노막대의 성장 메커니즘을 실시간으로 관찰하였다. 이런 실시간 관찰을 통해 인듐비소 나노막대의 초기 성장과정에서 부분적으로 인듐 포화 상태에서 비소 포화 상태로 성장 조건이 바뀌어 나노막대의 구조적 변화가 동반된다는 사실을 확인하였다. 또한, 인듐비소 나노막대 주변에

성장되는 갈륨비소 코팅층의 내부 스트레인이 성장 과정과 동시에 점차 해소되는 현상을 RHEED 투과 방식 분석을 통해 실시간으로 확인하였다.

주요어: 투과전자현미경, 핵생성 및 성장, 그래핀, 화합물 반도체, 나노구조물, 개선된 결정성장 및 관찰법

학 번: 2014-30226